Excitonic Spin Engineering in Optoelectronic Devices

by

Daniel Norbert Congreve

Submitted to the Department

of Electrical Engineering and Computer Science

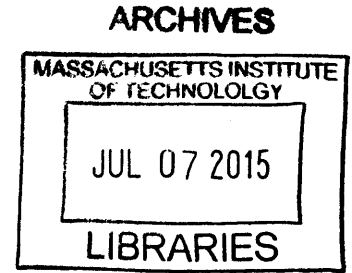in partial fulfillment of the requirements for the degree of

Doctor of Philosophy

at the

Massachusetts Institute of Technology

June 2015

Author....... Signature redacted

Department of Electrical Engineering and Computer Science

May 19, 2015

Certified by...... Signature redacted

Professor Marc A. Baldo

Thesis Supervisor

Certified by........ Signature redacted

Professor Leslie A. Kolodziejski

Chair, Department Committee on Graduate Students

1

Excitonic Spin Engineering in Optoelectronic Devices

by

Daniel Norbert Congreve

Submitted to the Department of Electrical Engineering and Computer Science on May 19, 2015
in partial fulfillment of the requirements for the degree of Doctor of Philosophy

Abstract

Despite decades of research, solar cell efficiencies struggle to get higher than 25%. This is due to two fundamental losses in the device: thermalization of high energy photons and transmission of low energy photons. In this work, we demonstrate efforts to improve both these losses, which, when fully realized, could increase power efficiencies to 35% or higher.

First, we utilize singlet exciton fission as a downconverting layer. Singlet exciton fission is a process in which a single high energy exciton fissions into two excitons of half the energy. Here, we first demonstrate the potential of singlet fission in an all-organic solar cell. We measure an EQE as high as 109%, breaking the conventional limit of 100%. We utilize the magnetic field effect of fission to characterize and quantize the fission yield in these devices, demonstrating that an increase in absorption should lead to even higher EQE values. Next, we utilize an optical light trapping scheme to increase the absorption, driving the EQE as high as 126% with no external optics. Finally, we demonstrate the ability to orthogonalize singlet fission from the normal OPV functions such as absorption and charge transport with a small interfacial layer of a fission material.

With the efficiency of singlet fission established, we then demonstrate how it can be utilized by building an optical downconverter with tetracene as the fission material and PbS colloidal nanocrystals as the acceptor. We demonstrate that low energy excitons generated in the fission material transfer to the nanocrystal with 90% efficiency before fluorescing. This fluorescence will be able to transfer energy to inorganic solar cells such as silicon.

To combat the transmission loss, we turn to the reverse process of singlet fission: triplet-triplet annihilation. We utilize colloidal nanocrystals as the sensitizer and rubrene as the annihilator. The use of colloidal nanocrystals as the sensitizer allows us to minimize energetic loss and extend deeper into the infrared as compared to state of the art devices, while allowing for facile construction of a solid state geometry. We characterize this process and demonstrate the potential it holds for future solar cells.

Finally, we characterize the charge transfer state in organic solar cells. We demonstrate that intersystem crossing plays a key role, defining device performance and recombination. We further show that these states are mobile and can diffuse via an 'inchworm' hopping motion.

Thesis supervisor: Marc Baldo

Supervisor title: Professor of Electrical Engineering, *EECS*

Acknowledgements

Contents

5

List of Figures

Chapter 1: Solar Energy

1.1. Solar Energy Generation

It is estimated that world energy consumption will approach 30 TW by 2030, double what is currently used.[1] Finding 15 TW of energy generation is a daunting task; finding 15 TW of clean, renewable energy doubly so. Nature, however, has provided us with a tremendous opportunity: over 89,000 TW of light energy falls on the earth. Capturing but a sliver of this energy could greatly ease energetic demands, allowing for pollution-free, stable energy generation for billions of people.

Of course, reality is not so simple. Latitude dependence, seasons, and weather can greatly reduce the energy available by a factor of 5 or more,[2] yet still, the United States has some of the best solar real estate in the world, see Figure 1-1.
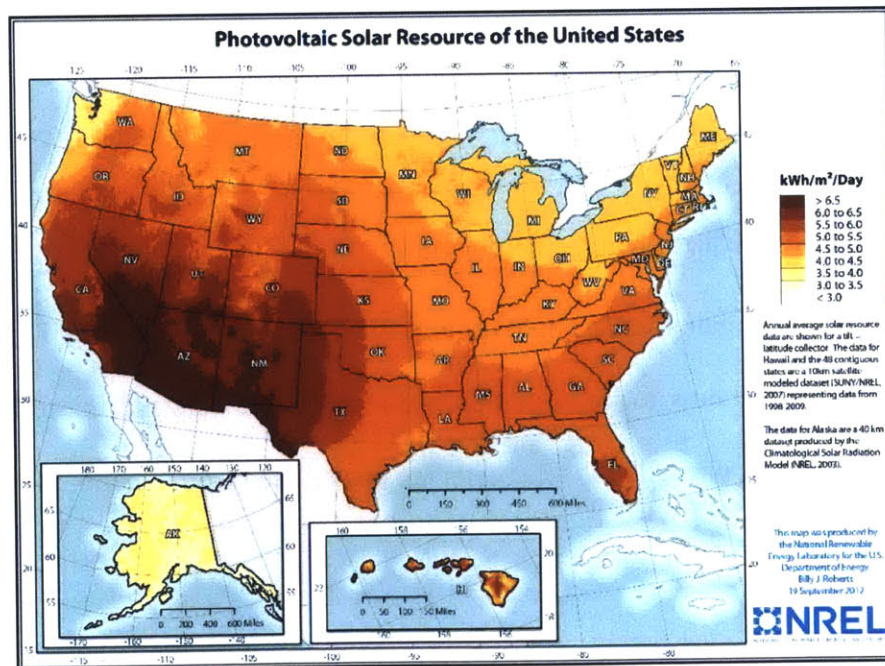
Figure 1-1. Solar resources of the US shows excellent solar real estate in the southwest. Data from NREL.[3]

Indeed, the United States has been scrambling to take advantage of this area, with over 4,000 MW installed in 2013.[4] This growth occurs mostly in the southwest states highlighted in Figure 1-1; however some states such as Massachusetts are using subsidies to drive growth in lower solar flux locations.[4] Indeed, Massachusetts ranks 5th of all states in installed capacity.[5] Overall, the US solar market continues to grow exponentially, see Figure 1-2.
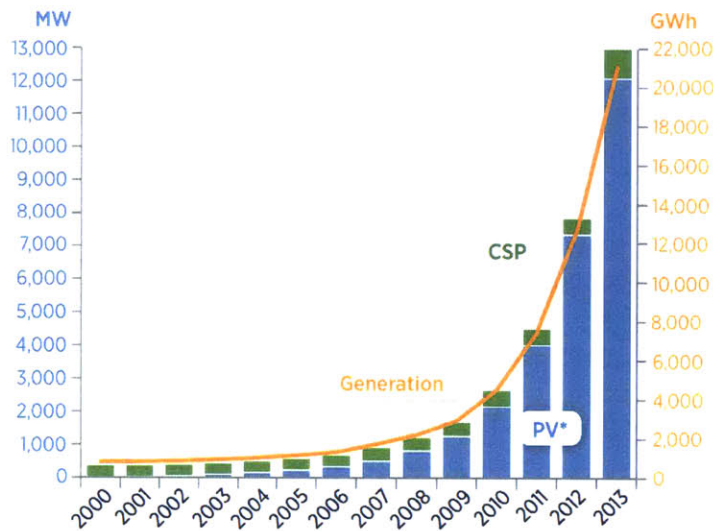
Figure 1-2. Installed solar capacity in the US. Data from NREL.[5]

1.2. Modern Photovoltaic Systems

Despite these rapid gains, solar photovoltaics still represents only 0.5% of our total energy generation.[5] To understand how to improve this, we must first understand the technology being used. On the market today, virtually all solar cells are constructed from silicon, see Figure 1-3.

By Technology

Mono c-Si 24%
9,354 MW

Multi c-Si 65%
25,467 MW

CdTe 4%
1,640 MW

CIGS 3%
1,271 MW

a-Si 3%
1,254 MW
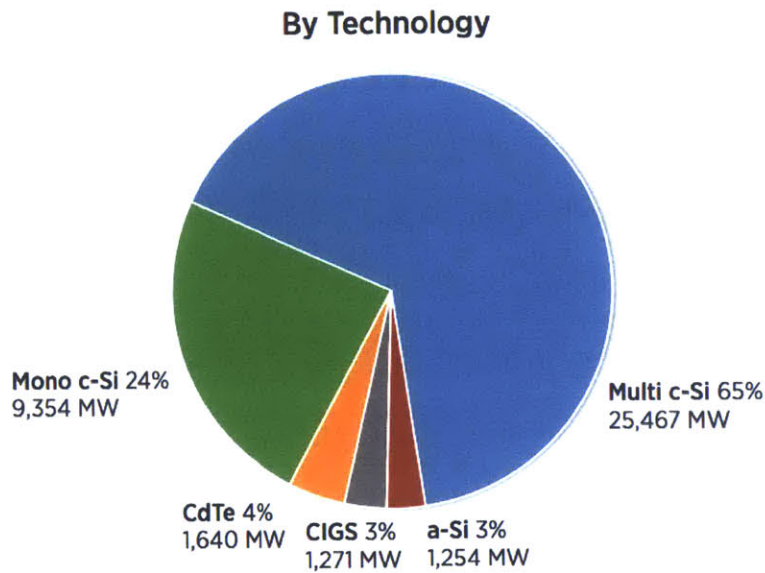
Figure 1-3. Solar cell technology used in the US. Data from NREL.[5]

Silicon technology, either monocrystalline or multicrystalline (lower quality wafers with grains on the order of a centimeter), makes up 89% of the market today. So called 2nd generation thin-film systems make up the remaining 11%. Clearly, silicon is the most critical technology on the market today. Understanding and improving on its deficits will provide a clear path forward towards more cost-effective photovoltaics.

1.3. Shockley-Queisser Limit

The world's best silicon solar cells are 25% power efficient at lab scale.[6] In other words, three-quarters of the light incident upon them is wasted. To understand these losses, we must examine the basic functioning of the sun and of a solar cell. Sunlight is broadband, spreading over

a wide range of ultraviolet, visible, and infrared wavelengths. The power received at typical US latitudes is plotted in Figure 1-4, black line.

Silicon is defined by its bandgap of 1.12 eV, corresponding to light of 1100 nm wavelength. Light at this energy is efficiently absorbed and collected as electricity. Light greater than this bandgap is also absorbed, but the generated carriers rapidly thermally relax to the band edge of the device, wasting the excess energy as heat. Therefore a single high energy blue photon provides the same output energy as a low energy infrared one. The energy a silicon solar cell is able to capture is indicated in purple in Figure 1-4. The loss from high energy photons due to heating is termed *thermalization*. This loss is extremely harmful in the visible spectrum, where over half the incident energy can be wasted.

A second loss is also shown in Figure 1-4: any photon with energy less than the bandgap will pass through the cell unabsorbed. Therefore, silicon cells collect no energy from photons with wavelength greater than 1100 nm. These two losses form the backbone of the Shockley-Queisser limit, which limits silicon solar cells to approximately 33% efficiency.[7] The remaining 8% difference between the Shockley-Queisser limit and top lab efficiencies are due to incomplete absorption and voltage losses, among other things, and are beyond the scope of this document.
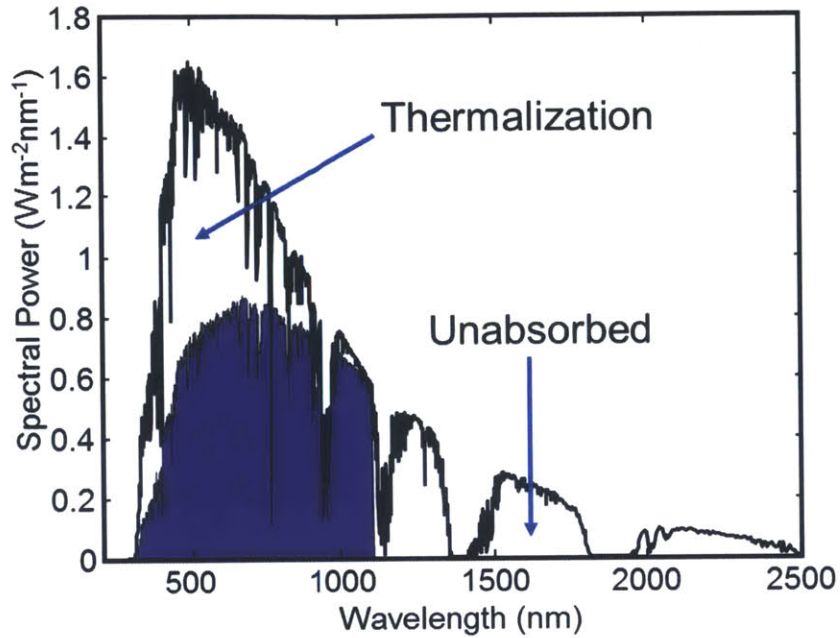
Figure 1-4. The spectral power density of the sun (black line) and the amount of the power collectable by silicon solar cells (purple).
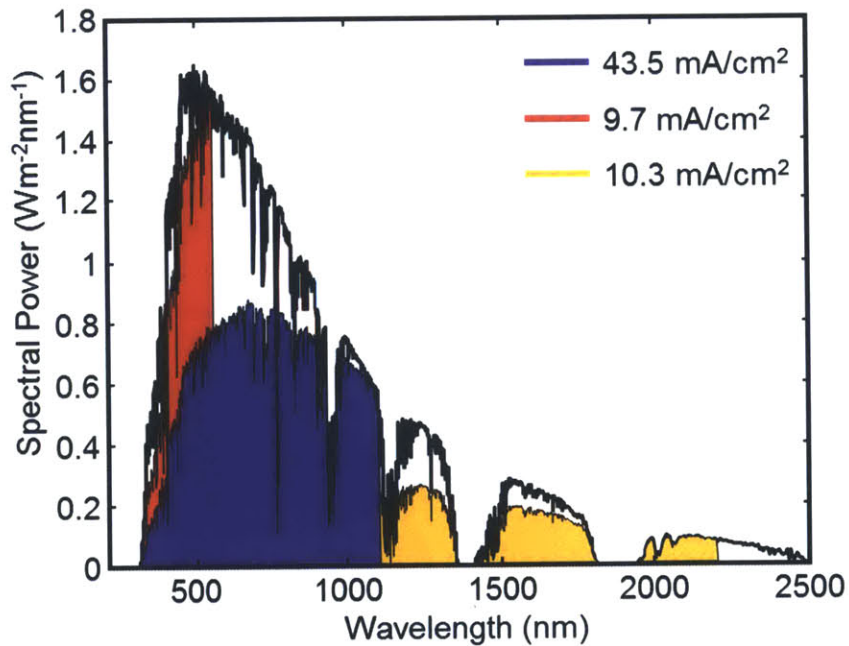
Figure 1-5. The gains from downconversion (red) and upconversion (yellow) are quite large, each representing almost a 25% relative increase on the current power efficiency of silicon cells.

1.4. Circumventing the Limit

There are many ways to get around the Shockley-Queisser limit, but they all revolve around the same fundamental principle: use an alternative material with a different bandgap to absorb different portions of the spectrum light. This is most commonly demonstrated in III-V solar cell tandem structures, in which multiple solar cells are stacked vertically and efficiencies have exceeded the Shockley-Queisser Limit.[8] These cells, however, are quite expensive to produce, and therefore not suitable for terrestrial applications.

Instead, we propose optical manipulation of the incident photons. The specifics will be detailed in the following chapters. Here, we present the overarching physics that defines these materials.

1.4.1. Downconversion

Downconversion is the process by which one high energy photon splits into two photons of half or less of the initial energy, see Figure 1-6(a). A high energy photon is absorbed by our downconverter black box, which then emits two photons at half the energy. The silicon solar cell can now output twice the photocurrent as a cell without the downconversion. This black box is operational for all wavelengths twice or greater the energy of the bandgap, or 550 nm and bluer for silicon. The potential spectral gains are highlighted in red in Figure 1-5. A perfect downconverter black box would give a silicon solar cell an extra 9.7 mA/cm^2 of photocurrent, increasing the power conversion limit to approximately 40%.

It is important to note that when trying to realize these devices in practice, outputting less than one photon per incident photon (or efficiencies less than 100% on a 200% scale) will actively

harm the device, as energy is now being wasted in the black box instead of being absorbed by the silicon PV.
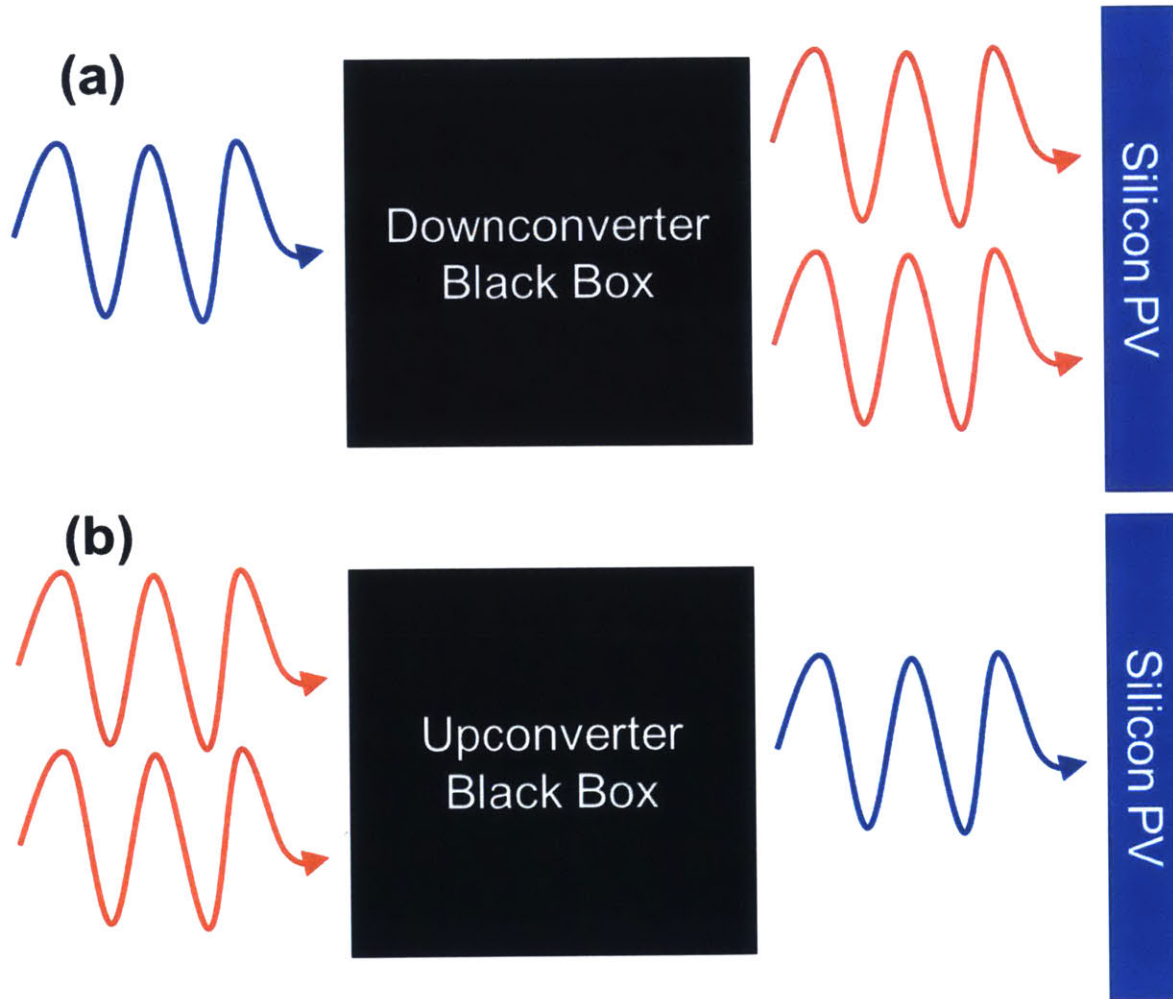
Figure 1-6. Basic schemes for upconversion and downconversion. (a) In downconversion, one high energy photon is split into two photons of half the energy, both of which can now be absorbed by the silicon solar cell. (b) In upconversion, two un-absorbable low energy photons are fused to create one higher energy photon which the silicon solar cell can then absorb.

1.4.2. Upconversion

Upconversion is the process by which two low energy photons are fused to become one high energy photon, see Figure 1-6(b). Two low energy photons are absorbed by our upconverter black

box, which then emits a single photon at twice the energy. The silicon solar cell can thus output photocurrent at a wavelength that a cell without the black box could not. This black box is operational for all wavelengths half or greater the energy of the bandgap, or 2200 nm and bluer for silicon. The potential spectral gains are highlighted in yellow in Figure 1-5. A perfect upconverter black box would give a silicon solar cell an extra 10.3 mA/cm^2 of photocurrent, increasing the power conversion limit to approximately 40%. Unlike downconversion, any photocurrent generated from an upconversion device is useful, as the cell would otherwise convert none of the low energy light to electricity.

Finally, the gains of upconversion and downconversion are not mutually exclusive; one could envision a silicon solar cell that takes advantage of both technologies. In that case, the power conversion limit tops 48%. Clearly, the ability to successfully perform high efficiency upconversion and downconversion would be a tremendous boost to photovoltaics and energy conversion in general.

Chapter 2: Organic Photovoltaics

Organic electronics is an extremely broad field. In this section, we endeavor to provide a clear picture of the relevant physics in these materials and provide a brief history of organic materials as photovoltaics.

2.1. Excitons

Excitons, bound electron-hole pairs,[9] define the device characteristics of a wide variety of materials. Traditional inorganic materials have a high dielectric constant, and therefore loosely bound electron-hole pairs. These charges can readily diffuse apart and are easily separated. Organic materials have a low dielectric constant, such that the charges are much more tightly bound to one another, with binding energy much greater than kT.[10] They do not separate easily and travel as quasi-particles that we call excitons. Here, we endeavor to describe the interesting physics behind these quasi-particles so that we can manipulate them in an intelligent way.

2.1.1. A Single Molecule

A single molecule is the simplest building block any organic system can be divided into. Yet even that is far too complex for exact quantum mechanical modeling. A single pentacene, for instance, contains 22 carbon atoms and 14 hydrogen atoms, each of which must be precisely modeled. Therefore, we utilize the Born-Oppenheimer approximation,[11] which states that, due to their large difference in mass, electrons move much more quickly than their nuclear counterparts. Therefore, we can assume the nuclei are fixed, and we can treat the electrons and the nuclei separately.

2.1.2. HOMO and LUMO

A given molecule contains a complicated energy structure, with electrons filling the bonds of the molecule as defined by the Pauli exclusion principle, from the tightly bound electrons all the way up to very loosely bound ones, with anti-bonding combinations unoccupied further up in energy. In order to simplify the molecule still further, we assume that all the deep energy electrons are tightly bound and therefore inaccessible for most optoelectronic applications and concern ourselves with only those electrons in the highest occupied molecular orbital (HOMO) and the states of the lowest unoccupied molecular orbital (LUMO). Thus, we have simplified an extremely complicated molecule down to a two electron system.

2.1.3. State Symmetry

According to the Pauli principle, when two electrons are exchanged, the total wavefunction must be anti-symmetric, that is,

$$\psi(r_1, r_2) = -\psi(r_2, r_1) \tag{2.1}$$

Where ψ represents the total wavefunction. The wavefunction can be broken down into two parts, a physical wavefunction Φ and a spin wavefunction σ such that

$$\psi = \Phi\sigma \tag{2.2}$$

By inspection, in order for ψ to be anti-symmetric, one of Φ and σ must be symmetric, while the other must be anti-symmetric. Therefore, when we examine the spin of these states, we can break them down into two groups: those with anti-symmetric spin and those with symmetric spin.

Because the state has two spin-half electrons, each state can have a total spin of zero or one. We then find that there exists one anti-symmetric spin state, corresponding to S = 0:

$$\sigma_{AS} = \frac{1}{\sqrt{2}}(\alpha\beta - \beta\alpha) \tag{2.3}$$

Where α and β are spin-up and spin down electrons, respectively. There are also three symmetric spin states which correspond to S = 1:

$$\sigma_S = \alpha\alpha \tag{2.4}$$

$$\sigma_S = \frac{1}{\sqrt{2}}(\alpha\beta + \beta\alpha) \tag{2.5}$$

$$\sigma_S = \beta\beta \tag{2.6}$$

These two groupings are referred to as the singlet and triplet states, respectively due to their respective degeneracies.[12] It is important to note that the spatial wavefunction will have the opposite symmetric property, that is, spin symmetric triplet states will have anti-symmetric spatial wavefunctions and vice versa.

2.1.4. Optical transitions

With the degeneracies of states in hand, the question of interactions with light naturally arises. The dipole operator for a two electron system is $-er_1 - er_2$ and is by inspection symmetric under particle exchange. We can then evaluate the dipole between symmetric and anti-symmetric states

$$\mu = \langle\sigma_{AS}|-er_1 - er_2|\sigma_S\rangle \tag{2.7}$$

If one were to switch the two electrons, the anti-symmetric wavefunction would flip sign, but the symmetric would not. Therefore, it is easy to see that μ would change sign. However, the dipole cannot have a dependence on electron exchange, and therefore must be 0. This demonstrates that symmetric states can only couple to symmetric states, and anti-symmetric states can only couple to anti-symmetric states. That is, absorption of light can only excite a singlet state into a higher energy singlet state, or a triplet state into a higher energy triplet state. In virtually all organic molecules, including all of those presented in this document, the ground state is a singlet, such that all interactions with light see the excitation from the ground singlet state to a higher energy singlet state. Further, this means all triplet states are forbidden from relaxing to the ground state, and therefore have an extremely long lifetime as compared to singlet states.

These dynamics are clearly demonstrated in Figure 2-1. The transition from singlet to singlet state is rapid and proceeds on the order of a few nanoseconds. When this involves the emission of a photon, it is termed fluorescence. Transition from an excited singlet to excited triplet is termed intersystem crossing and typically occurs on the microsecond timescale. In most materials, other processes proceed much faster and so intersystem crossing is not observed. The transition from the spin triplet excited state back to the spin singlet ground state is also spin forbidden and proceeds quite slowly. When this involves the emission of a photon, it is termed phosphorescence, and is a useful process in a sub-set of organic molecules used in OLEDs.[13]
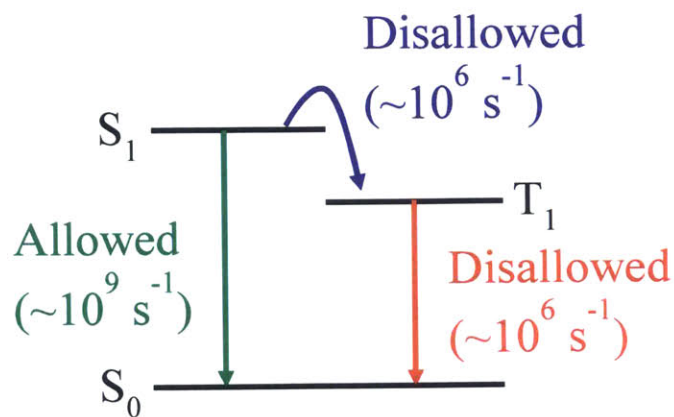
Figure 2-1. Allowed and disallowed transitions in organic semiconductors. Moving between singlet states (green arrow) is quite fast; however, moving between triplet and singlet states (purple and red arrows) requires a spin flip and is therefore quite slow.[14]

The anti-symmetric spatial wavefunction of triplet states has a second effect that is critical to note. The wavefunction reduces electron-electron repulsion in the system, lowering the overall energy of the triplet state relative to the singlet state. The triplet state is typically considered to be about 0.7 eV below the singlet state,[15] but this is hugely dependent on molecular geometry. The splitting is proportional to the overlap between the HOMO and LUMO, such that intelligent molecular design can allow for high or low splitting. For instance, recent efforts to separate the electron and hole in thermally assisted delayed fluorescence molecules for use in OLEDs has reduced the splitting to less than 100 meV.[16]

2.2. Photovoltaic Device Operation

In the early days of organic photovoltaics, an organic material was sandwiched between two contacts. This structure struggled to overcome the large binding energy of the generated

excitons, and efficiencies were quite low. That changed in 1986 with Tang's development of the bilayer system.[17] The addition of an electron accepting layer allowed for facile dissociation of the excitons and approximately 1% power conversion efficiency. The cell operated as shown in Figure 2-2. Light is absorbed into the singlet exciton, which then diffuses to the interface of the cell. The electron then hops to the electron acceptor, generating a bound charge transfer (CT) state. This state then dissociates into free charge. The physics of this dissociation is still an active area of research, including in this document, see Chapter 7 for more details.
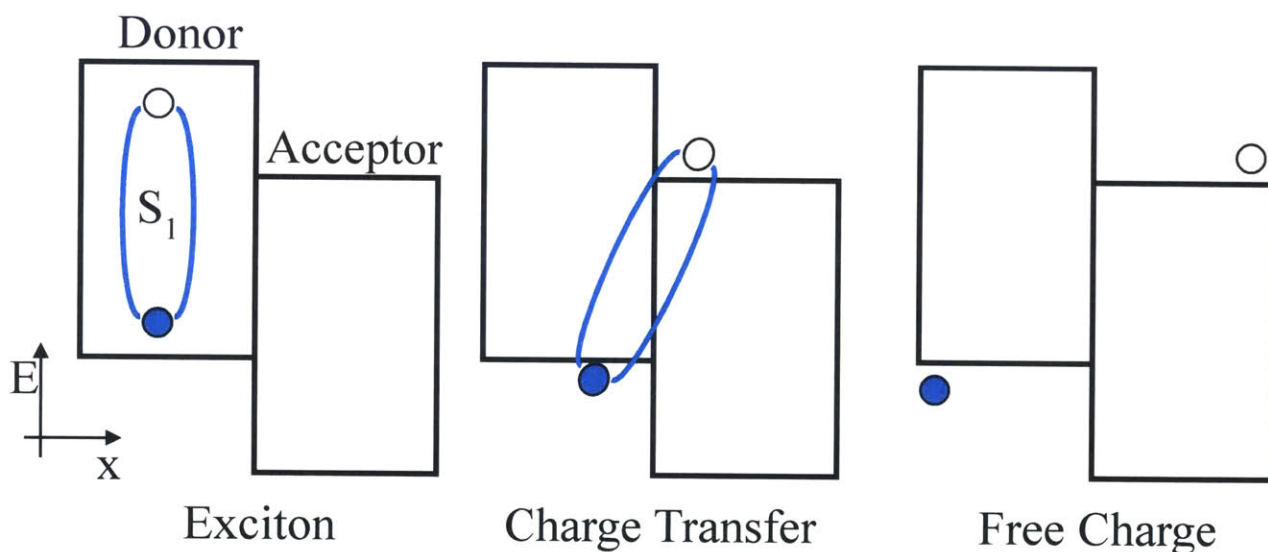
Figure 2-2. To generate photocurrent, an organic photovoltaic absorbs energy into the excitonic state, which diffuses to the interface where the electron jumps to the acceptor. This forms a bound charge transfer state which can then separate into free charge which can be collected at the contacts.

Since then, research in photovoltaics has exploded. The development of a bulk heterojunction, in which the donor and acceptor are mixed together, allowed for an increase in absorption without sacrificing collection efficiency.[18] Modern devices exhibit the ability to collect absorbed photons with near unity efficiency[19] and power conversion efficiencies of up to 11%.[8]

However, these devices still suffer from stability issues.[20] With the recent rise of alternative photovoltaic materials such as perovskites[21] and colloidal nanocrystals,[22] researchers must continue to increase the power efficiency of these organic materials or risk being left behind.

Chapter 3: Singlet Exciton Fission

Singlet exciton fission is the spin-allowed, energy conserved process of splitting one singlet exciton into two child triplet excitons. Here we offer a brief history of the field and an overview of the relevant physics. We conclude with a brief look at the field today, particularly as it pertains to singlet fission devices.

3.1. History of Singlet Fission

Singlet fission was first discovered as triplet-triplet annihilation in 1965 in anthracene crystals;[23] it was quickly realized to be of significant importance for tetracene as well.[24,25] The key to proving the physics of singlet fission was the change in rate with applied magnetic field as shown by Johnson and coworkers.[26] A model for magnetic field modulation was developed by Merrifield[27] and further refined by Suna.[28] The technology was recognized by Dexter for its potential for downconversion,[29] but it was not yet mature enough for further development.

After 30 years of limited research, interest in singlet fission was revived in the early 2000's when it was realized that OPV technology had matured enough to further examine its potential.[30,31] This sparked a renaissance of interest in the topic that has since continued unabated.[32] Researchers have discovered a library of materials[31-36] that perform singlet fission and utilized ultrafast spectroscopy to better understand the its mechanism.[37-41]

3.2. Conservation of Energy and Spin

Singlet fission, like all physical processes, requires that energy be conserved. The final state has two excitons, each of which must be approximately half the energy of the original exciton. Thus, singlet fission is limited to molecules in which the T_1 state is approximately half the energy of the S_1 state. This limits the singlet fission engineer to a small choice of materials; see [31] for a discussion of many of these. For example, tetracene is slightly uphill, with a singlet state at 2.3 eV and a triplet state at 1.25 eV,[42] but fission still proceeds on the order of one hundred picoseconds. The singlet quenching in tetracene is shown in Figure 3-1. Despite the energy needed, fission proceeds relatively independently of temperature,[43,44] an area that is still under active research.[45]
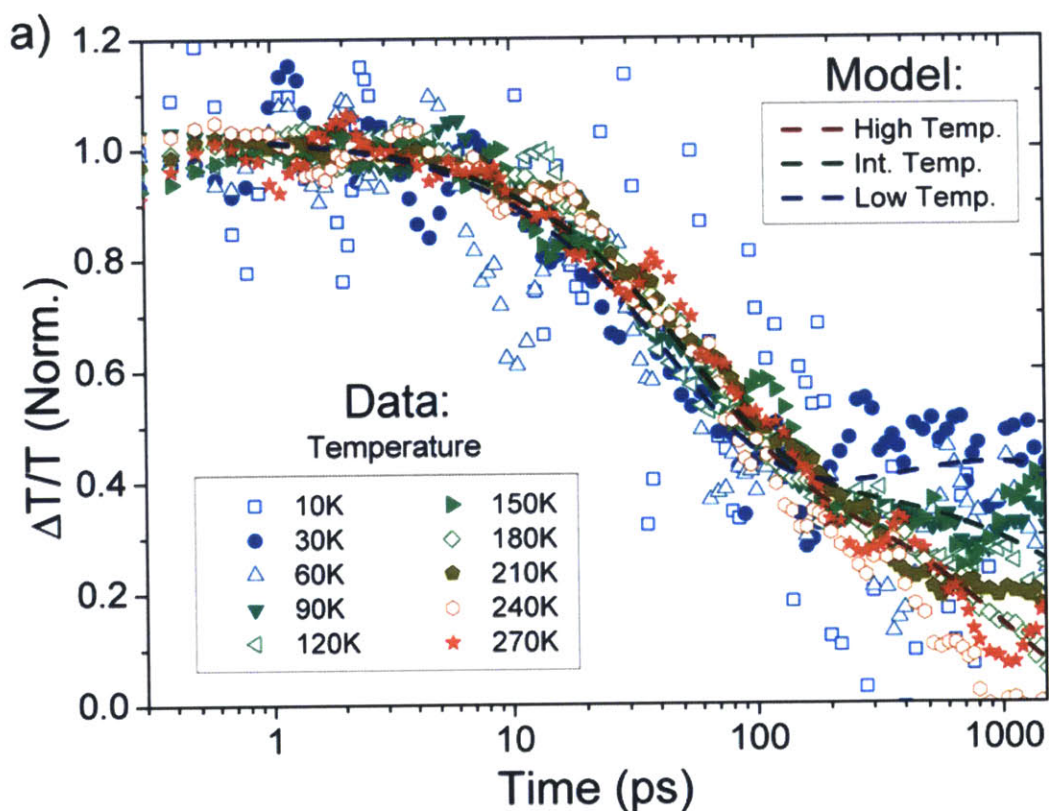
Figure 3-1. Decay of the singlet state in tetracene. Fission proceeds in tetracene with a 100 ps time constant, independent of temperature. Data taken from [44] with permission.

Pentacene, by contrast, is approximately 110 meV downhill,[46,47] and proceeds with near unity efficiency and a time constant on the order of 80 fs.[48] Figure 3-2 shows the evolution of the singlet and triplet populations in pentacene. The singlet extinguishes and the triplet grows in on the same ~80 fs timescale, demonstrating the extremely high speed of fission in this material.
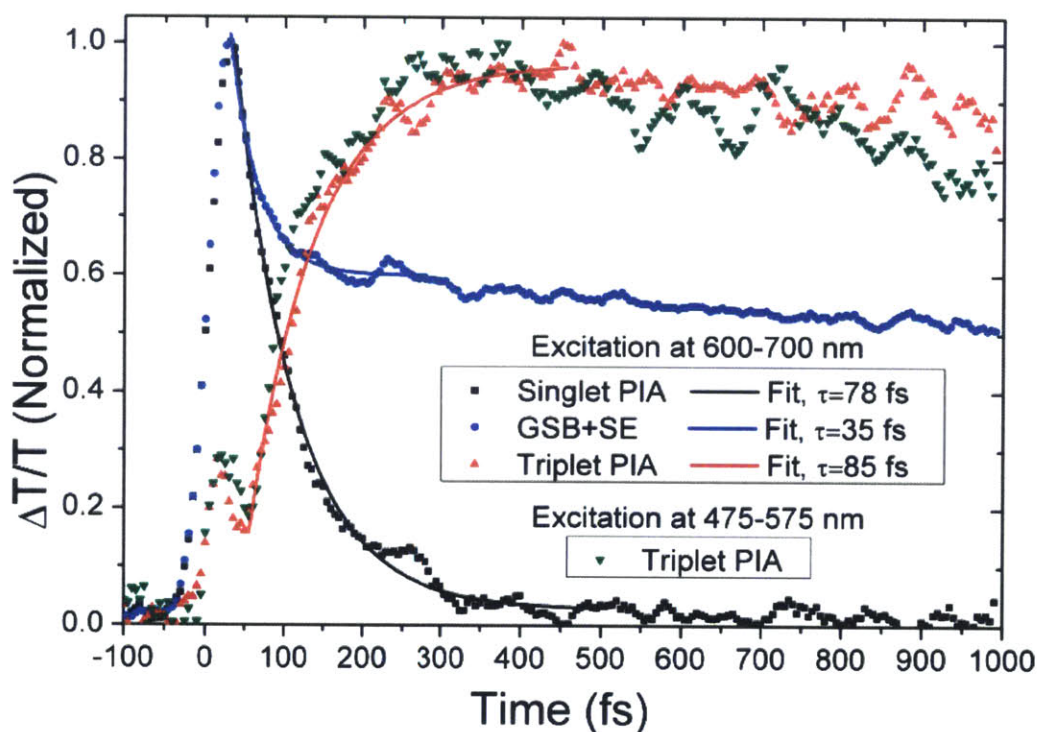
Figure 3-2. Transient dynamics of thin film pentacene. The singlet quenches with a timescale of 78 fs, while the triplet signal rises with a time constant of 85 fs. Fission occurs extremely fast in pentacene. Figure taken from [48] with permission.

Singlet fission also requires that spin be conserved. The decay $S_1 \rightarrow T_1$ is spin disallowed, and typically occurs on the micro- to milli-second timescale. Thus, intersystem crossing is not competitive with fission and can be ignored in these materials. Therefore, fission must proceed

through a state of two triplets with correlated spin, termed the triplet pair state. The triplet pair state has nine possible spin states. Because the starting state of singlet fission is of singlet character, the final triplet-triplet state must also have singlet character. This is a key feature of singlet fission and is discussed in some detail below.
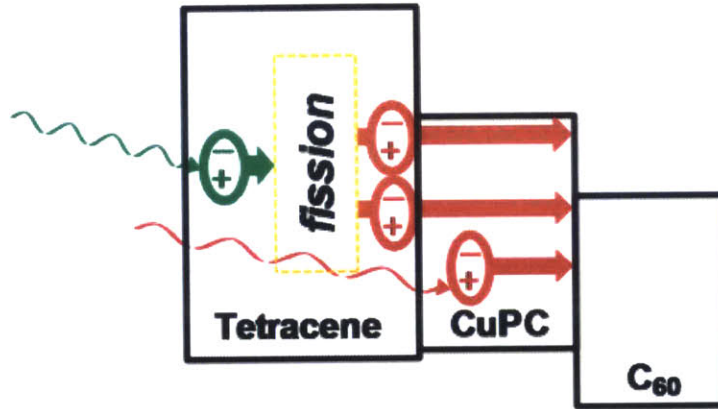
Figure 3-3. One scheme for increasing photocurrent in a fission device. The low-energy absorption is provided by the CuPC layer, while the tetracene provides double photocurrent from high energy photons. From ref. [49].

Spin conservation also means that there is no absorption cross section for energies between the T_1 and S_1 state. Thus, on its own, singlet fission doubles the potential photocurrent while halving the available voltage for no net gain in power efficiency. In order to increase the power efficiency this absorption must be made up elsewhere in the device. An example of a scheme to do so is shown in Figure 3-3. The CuPC layer provides low-wavelength absorption, while the tetracene provides two electrons from the high energy photons. The gains from this structure are clearly demonstrated in Figure 3-4. This has also been demonstrated in devices utilizing colloidal nanocrystals as the acceptor.[50,51]
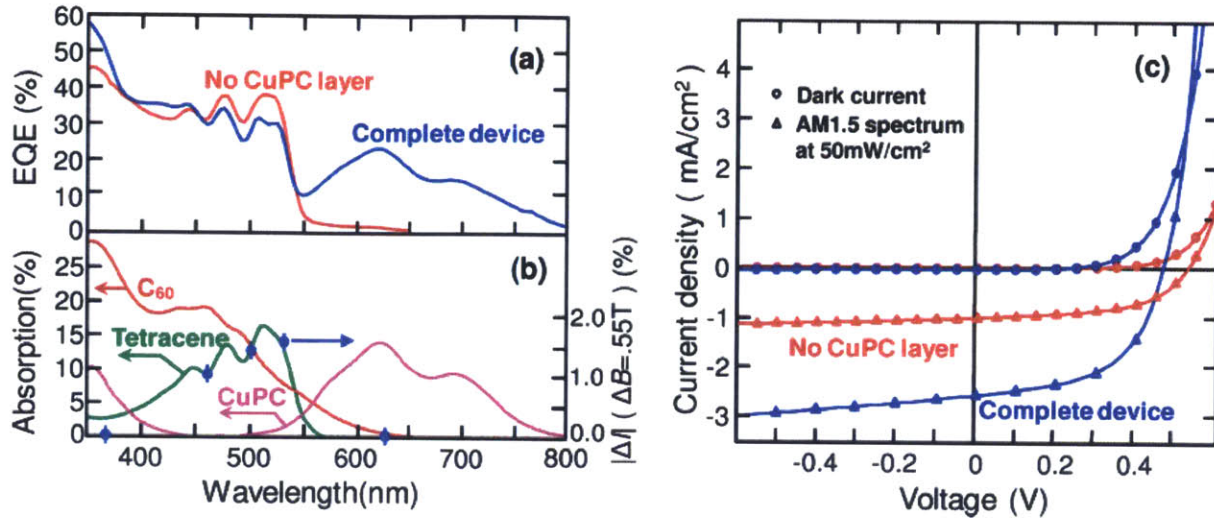
Figure 3-4. The addition of a low energy absorber increases the photocurrent from the solar cell, demonstrating the clear advantage for singlet fission. From ref [49].

3.3. Merrifield Model

In this section, we examine the role that the number of states has on the singlet fission rate. This will have a direct impact on the magnetic field effect in the next section. To do this, we utilize the Merrifield model.[27] Although this model has trouble reproducing short time dynamics and low-field modulations,[52] it is also straightforward to understand and conveys the dynamics well enough for our purposes here.

To start, we examine the system below. Generated singlet states transfer into one of nine triplet-triplet pair states, which then can separate into independent triplets. The reverse processes are also possible. The numbering scheme may seem odd, but stems from the fact that this model was initially developed to model fusion of triplets into a singlet.

$$S_1 \underset{k_2}{\overset{k_{-2}}{\rightleftharpoons}} (T_1T_1)^l \underset{k_1}{\overset{k_{-1}}{\rightleftharpoons}} T_1 + T_1 \qquad (3.1)$$
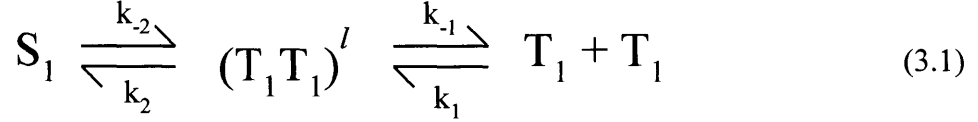
The rate between the singlet state and an individual triplet-triplet pair state will be the defined rate multiplied by the coupling $|C_l^s|^2$, defined such that

$$C_l^s = \langle S_1 | T_1 T_1{}^l \rangle \qquad (3.2)$$

In order to simplify the problem, we assume that the steady state concentration of the triplet-triplet pair state does not change, that is:

$$\frac{d[T_1T_1]^l}{dt} = 0 \qquad (3.3)$$

Thus, the magnetic field effect is now simplified to a simple rate problem, such that:

$$\frac{d[S_1]}{dt} = -k_{-2} \sum_{l=1}^{9} |C_l^s|^2 [S_1] + \sum_{l=1}^{9} k_2 |C_l^s|^2 [T_1T_1]^l \qquad (3.4)$$

$$\frac{d[T_1T_1]^l}{dt} = 0 = k_{-2}|C_l^s|^2[S_1] - k_2|C_l^s|^2[T_1T_1]^l - k_{-1}[T_1T_1]^l$$
$$+ k_1[T_1]^2 \qquad (3.5)$$

$$\frac{d[T_1]}{dt} = 2k_{-1} \sum_{l=1}^{9} [T_1T_1]^l + k_1[T_1]^2 \qquad (3.6)$$

Utilizing these equations and a mild amount of algebra, we can solve for the time dynamics of the system, such that:

$$\frac{d[S_1]}{dt} = -k_{fis}[S_1] + k_{fus}[T_1]^2 \qquad (3.7)$$

$$\frac{d[T_1]}{dt} = 2k_{fis}[S_1] - k_{fus}[T_1]^2 \qquad (3.8)$$

Where k_{fis} and k_{fus} are the rate of fission and fusion, respectively, and can be written as

35

$$k_{fis} = \sum_{l=1}^{9} \frac{k_{-2}|C_l^s|^2}{1 + {k_2}/{k_{-1}} |C_l^s|^2} \tag{3.9}$$

$$k_{fus} = \frac{k_1}{9} \sum_{l=1}^{9} \frac{{k_2}/{k_{-1}} |C_l^s|^2}{1 + {k_2}/{k_{-1}} |C_l^s|^2} \tag{3.10}$$

If we then assume that the singlet character is equally distributed across N states such that $|C_l^s|^2 = 1/N$, we can then qualitatively assess the effect that the number of states with singlet character has on the fission rate. It is trivial to see that

$$k_{fis} \propto \frac{N}{{k_2}/{k_{-1}} + N} \tag{3.11}$$

This result is plotted in Figure 3-5 for k_2/k_{-1} equal to 1. As the number of states with singlet character increases, so does the fission rate. Thus, if we understand how the number of states with singlet character changes with field, we can assess how the singlet fission rate will change with field.
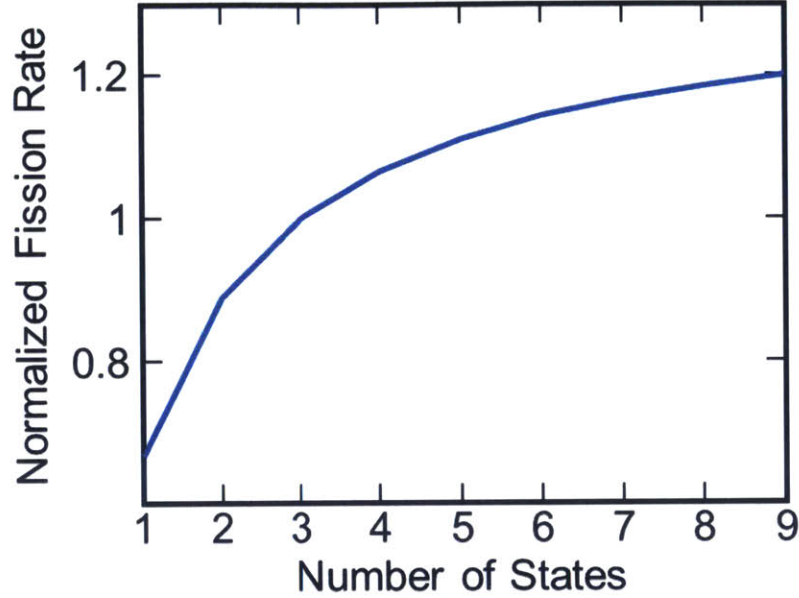
Figure 3-5. Fission rate vs number of states that have singlet character. k_2/k_{-1} is set to 1. The rate is normalized to that at 3 states with singlet character, as is the case for zero magnetic field.

3.4. Spin States of Singlet Fission

Thus, to determine the rate of fission, we need to determine how many triplet-triplet pair states have singlet character. To do so, we first slightly re-write the triplet eigenstates from Section 2.1.3, following Ref. [52]

$$x = \frac{1}{\sqrt{2}}(\beta\beta - \alpha\alpha) \tag{3.12}$$

$$y = \frac{i}{\sqrt{2}}(\beta\beta + \alpha\alpha) \tag{3.13}$$

$$z = \frac{1}{\sqrt{2}}(\alpha\beta + \beta\alpha) \tag{3.14}$$

Both sets of eigenstates are equally valid, but these simplify the resulting algebra considerably. We next turn our attention to the two-exciton state, corresponding to a four electron

37

system. This has 16 possible electron configurations: 2 singlet, 9 triplet, and 5 quintet states. We further examine the two singlet states

$$S = \frac{1}{\sqrt{2}}[(\alpha\beta)_1 - (\beta\alpha)_1]\frac{1}{\sqrt{2}}[(\alpha\beta)_2 - (\beta\alpha)_2] \tag{3.15}$$

$$S = \frac{1}{\sqrt{3}}[x_1 x_2 + y_1 y_2 + z_1 z_2] \tag{3.16}$$

Where the 1 and 2 subscripts refer to the first and second molecule, respectively. The first state is the singlet state of each of the individual molecules, as one would expect, and is uninteresting. Far more consequential is the second case, where we see that three triplet-triplet pair states that have singlet character, each with $|C_i^s|^2 = 1/3$. Therefore, at zero field, there are three states with singlet character.

In the high field limit, we can re-write the eigenstates as the z, $\beta\beta$, and $\alpha\alpha$ states. There are again three states with singlet character, namely the zz state in combination with the degenerate

$$T_{\pm} = \frac{1}{\sqrt{2}}[(\alpha\alpha)_1(\beta\beta)_2 \pm (\beta\beta)_1(\alpha\alpha)_2] \tag{3.17}$$

However, the spin-spin interaction between the electrons on the different molecules breaks this degeneracy, such that only the T+ state has singlet character. Thus, there exists only two states with singlet character, and fission is slowed. At intermediate magnetic fields, additional states have singlet character, and the fission rate is increased.[40] Thus, as a function of magnetic field, we expect the fission rate to increase at low fields before eventually saturating at a lower rate. This is a unique fingerprint with magnetic field and will be used extensively throughout this document.

38

Chapter 4: High Efficiency Singlet Fission Devices

4.1. Introduction

Although singlet fission has been demonstrated to proceed at high speed and high efficiency, a demonstration of high electron yield photovoltaics had yet to be achieved. In this section, we endeavor to build and quantify these high efficiency devices. We demonstrate that singlet fission does indeed proceed with efficiencies great than 100% through a simple electron-counting experiment. We demonstrate that a simple optical cavity can be used to boost absorption in the active layer, allowing for even higher efficiencies. Finally, we show that we can orthogonalize singlet fission from other device operations by utilizing a sensitization layer across two independent material systems. This section is adapted from references [53–59].

4.2. Materials and Methods

In this section, fabrication procedures are discussed. A basic introduction to our most prominent figures of merit, external quantum efficiency, internal quantum efficiency, and magnetic field effect, are provided, as well as a brief description of how they are measured in our laboratory.

4.2.1. Device Fabrication

The following details device fabrication for all devices in this section. Pentacene, PTCBI, and C_{60} were purchased from Luminescence Technology Corporation and further purified twice by vacuum sublimation. BCP and anhydrous chlorobenzene were purchased from Sigma-Aldrich and used as received. PEDOT:PSS (Clevios PVP AI 4083) was used as received. For Sections 4.1-

39

4.5, P3HT (Regio-regular trace metal basis 99.995% purity, MW 54,000-75,000) was purchased from Sigma-Aldrich and used as received. For Section 4.6, regio-regular P3HT (RMI-001EE) from Riekemetals was used instead because it allowed for much more consistent devices.

Organic photovoltaic structures were fabricated on pre-patterned indium tin oxide (150 nm) purchased from Luminescence Technology Corp. with a resistance of 15 Ohms per square. The substrates were cleaned in order of Micro90 detergent solution, deionized water, acetone, boiling isopropanol and then subject to 5 minutes of oxygen plasma cleaning. PEDOT:PSS was filtered by a 0.45 μm PVDF filter and spun on the pre-cleaned substrates in air at 4000 rpm for 60 seconds. The substrates were baked in a nitrogen glovebox (base level with less than 1 ppm O_2 and H_2O) for 20 minutes at 135 °C. In the glovebox, P3HT was dissolved in chlorobenzene at a concentration of 4 mg/mL and heated and stirred at 60 °C for 30 minutes. Once fully dissolved, the P3HT was filtered with a 0.2 μm PTFE filter and spun at 2000 rpm for 60 seconds onto the PEDOT:PSS coated substrates. Substrates were then baked at 110 °C for 20 minutes to remove any residual solvent.

Deposition of the anti-reflection coating (ARC), when used, began with the previously stated cleaning procedure followed by a deposition of 120 nm MgF_2 on the front surface of the substrate. The substrate was subsequently cleaned using the previously stated cleaning procedure but starting with acetone sonication as water might damage the MgF_2 coating. Further processing continued as usual.

All further organic layers were thermally evaporated at pressures less than 3×10^{-6} Torr at ~1 Å/s. The thermal evaporator was directly attached to the glovebox. The metal cathode was defined by a 1.44 mm diameter shadow mask. Devices were packaged in a dry nitrogen

environment using UV curing epoxy and glass substrates sized to cover all the active area. Thin film thicknesses were determined in-situ through use of quartz crystal oscillators. The tooling factor, the ratio between the nominal thickness and the actual thickness of thin films, was determined for each material before any device fabrication, and confirmed again at the conclusion using a Veeco optical interferometer using the monochromatic PSI mode (accurate 1– 35 nm step heights). Rotation of the substrate holder during thermal evaporation resulted in a thickness variation of ±10% across the width of the substrate holder.

4.2.2. External Quantum Efficiency

In the following sections we will focus on two main figures of merit: the external quantum efficiency (EQE) and the magnetic field effect (MFE). The EQE is a measure of how well a photovoltaic device converts incident light to electricity. It is a counting efficiency of the ratio between incident photons and output electrons, such that

$$EQE = \frac{Collected\ Electrons}{Incident\ Photons} \qquad (4.1)$$

EQE is typically expressed as a function of wavelength. The highest achievable EQE in standard single junction photovoltaic devices is 100%, and indeed, modern devices approach this limit quite closely.[6] Multiple exciton generation offers a route around this limit. An EQE greater than 100% was previously demonstrated in colloidal nanocrystals at energies greater than four times the bandgap deep in the UV,[60] a wavelength of little use to photovoltaics.

External quantum efficiency measurements were performed using a 150 W Xenon lamp coupled to a Newport monochromator with the output light mechanically chopped at a frequency greater than 200 Hz. The photocurrent was measured with a lock-in amplifier under low light

intensities ($<$ 100 μW/cm^2). A Newport 818-UV silicon photodetector calibrated by Newport and reported accurate to within 1% was used to determine the incident light intensity. This detector was also checked against a second Newport calibrated photodetector. Unless otherwise noted, all EQE measurements were performed at short circuit. A Keithley 2400 SourceMeter was used to apply any reverse biases.

4.2.3. Internal Quantum Efficiency

An important parameter wrapped up in the EQE is the absorption by the device. Internal quantum efficiency (IQE) is simply the EQE normalized by the absorption, such that

$$IQE = \frac{Collected\ Electrons}{Absorbed\ Photons} = \frac{EQE}{Absorption} \qquad (4.2)$$

Broadband absorption is a particular problem for organics; modern devices have IQEs near 100% but struggle to push their EQEs as high.[19] IQEs were calculated by dividing the measured EQE by the calculated absorption (see below).

4.2.4. Absorption Calculations

The optical constants n and k were determined from measured reflection (R) and transmission (T) of films deposited on a quartz substrate. As pointed out by Nitsche and Fritz[61] a simple calculation of k (from the absorption coefficient) and a Kramers-Kronig transform of k to obtain n are inaccurate when the frequency range over which k is measured is not infinite. Following their technique, we initially generated n by performing a Kramers-Kronig transform of k and refined both n and k iteratively until the simulated R and T curves had the least variance from

the experimentally measured *R* and *T*. Figure 4-1 shows the optical constants used for the materials in this chapter.

Using the optical constants and the transfer matrix method,[61,62] we calculated the absorption of the active layers for the given cavity structure. To determine each materials IQE, we varied the IQE of a given material until the IQEs multiplied by the absorption summed across all materials most accurately fit the measured EQE.
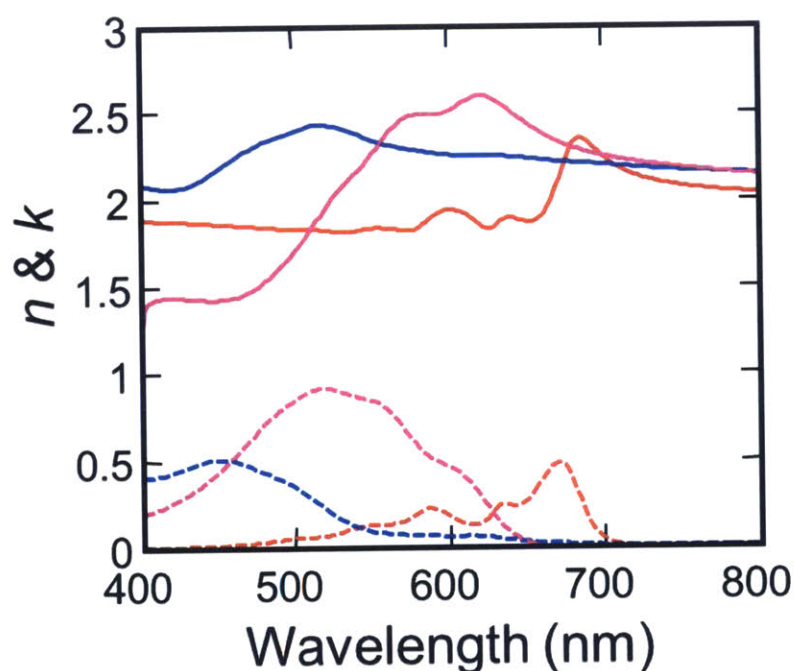
Figure 4-1. The real (—) and imaginary (– –) components of the index of refraction for pentacene (—), P3HT (—), and C60 (—) determined from layers deposited on quartz substrates.

4.2.5. Magnetic Field Effects

As discussed above, singlet fission has a magnetic field dependence. This allows us to utilize magnetic field effects (MFE) to diagnose what is occurring inside our device. Each

measurement provides three key results. First, it allows us to determine the presence of fission occurring in a molecule. Fission has a unique fingerprint with magnetic field – the rate increases at low fields and decreases at low fields, as discussed in Chapter 3. If our observable demonstrates this shape, we can be confident that it is somehow influenced by singlet fission. Second, the sign of the MFE allows us to determine whether our observable is proceeding through the singlet or the triplet channel. Slowing singlet fission with a magnetic field would naturally result in more singlet states and fewer triplet states, such that an increase in photocurrent would signal an observable sourced through the singlet state, while a decrease would signal an observable sourced through the triplet state. An example is provided in Figure 4-2. In this measurement, we monitor the fluorescence and the photocurrent from a tetracene solar cell. The fluorescence (red triangles) arises from the singlet state, so we see a positive MFE at high fields. Conversely, the photocurrent (blue circles) arises from the triplet state, so we see a negative MFE.
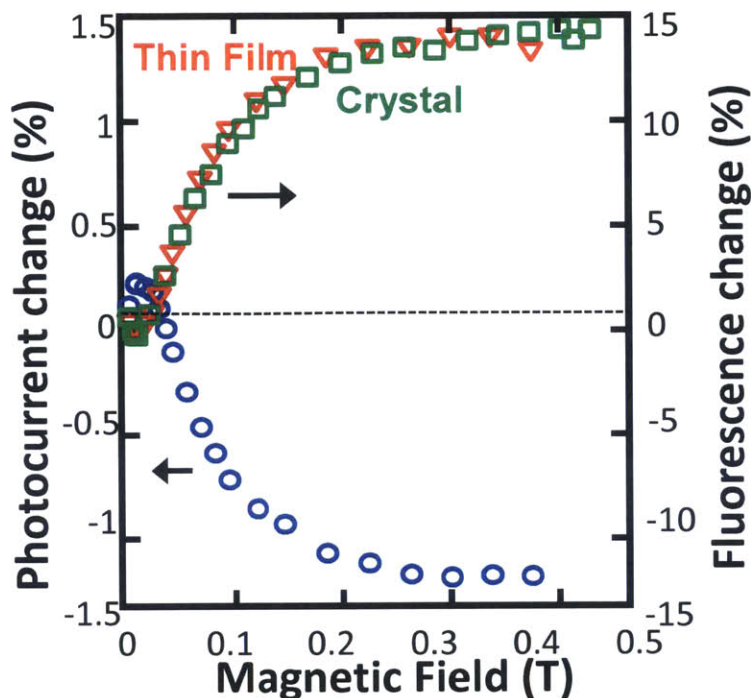
Figure 4-2. The MFE of a tetracene solar cell. Fluorescence from the singlet state (red triangles) gives a positive magnetic field effect, while photocurrent from the triplet state (blue circles) gives a negative effect. Data from Tony Wu.[54]

Finally, the magnitude of the MFE illuminates the workings of the rates inside of the device. Section 4.5 will discuss this in detail.

Measurements of the change in photocurrent with application of magnetic field were performed using a 1000 W Xe arc lamp (OBB) coupled to an OBB monochromator or with monochromatic light emitting diodes. Results using either system were identical. Light incident on the devices was mechanically chopped. While the device was under illumination, an electromagnet was energized at a frequency of 13 mHz with a duty cycle of 50%. The device current (measured by a lock-in amplifier) and the magnetic field (measured by a FWBell 5100 gaussmeter) were queried at a frequency of 1 Hz. Calculations of the change in photocurrent

occurred in the following steps: i) averaging the photocurrent when the applied magnetic field is at its maximum, ii) averaging the photocurrent when the applied magnetic field is zero, and iii) taking the difference between the two values and dividing by the current when the field is zero. Low incident light intensities ($< 1 \text{ mW/cm}^2$) were used to prevent device degradation during the experiment. All photodetector devices were reverse biased until the change in photocurrent was only attributed to singlet fission. For fluorescence measurements, emitted light was focused onto an appropriately filtered photodetector which was attached to the lock-in. A sample measurement as a function of time is shown in Figure 4-3.
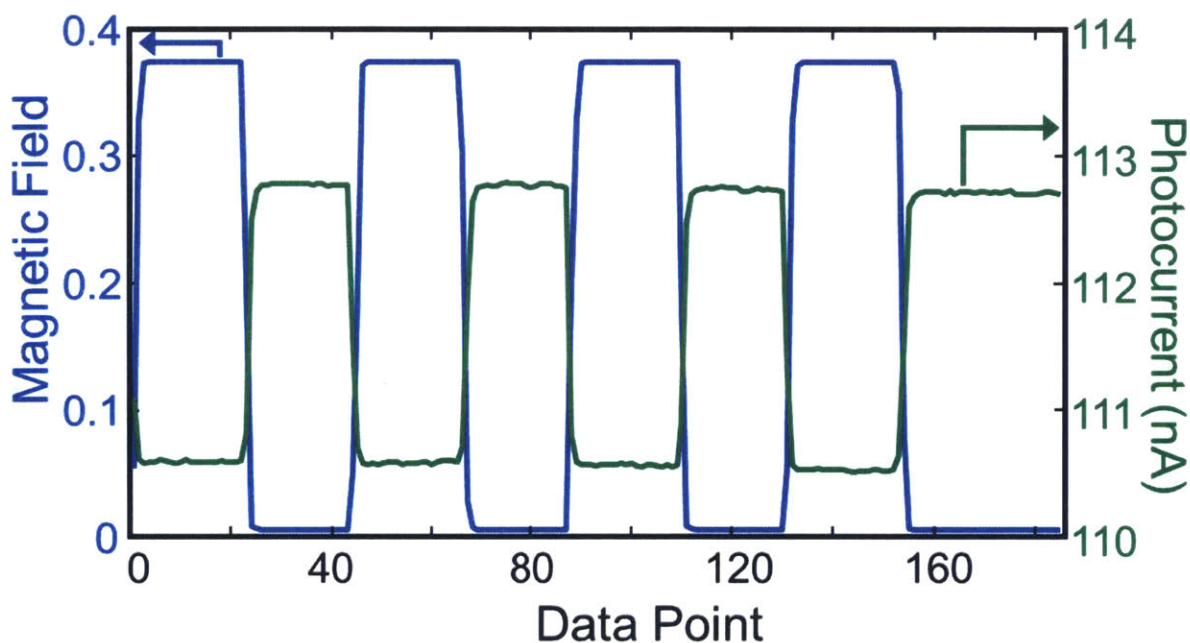
Figure 4-3. A sample output of the MFE system over time. The magnetic field (blue) is cycled and the photocurrent or fluorescence from the device (green) is monitored.

4.3. EQE and Device Modeling

To prove the efficiency of singlet fission, we build fission sensitized OPV devices and examine their EQEs as a function of device structure.

4.3.1. Device Structure

Pentacene has been shown to be both a fast fission material[39] and a strong photovoltaic performer when utilized in a junction with C_{60}.[63] A BCP blocking layer is used in conjunction with Ag to form the cathode, with the standard ITO as the anode. The pentacene layer is kept thin to reduce exciton diffusion losses. The EQE for this device can be seen in Figure 4-4. The EQE of the pentacene peak at 670 nm is only 24%; we attribute this to significant quenching of the excitons at the ITO anode.
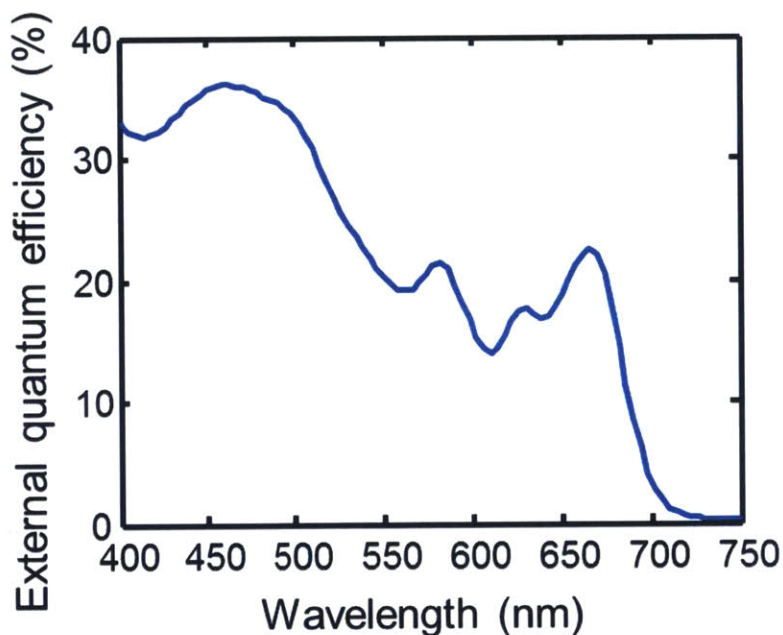
Figure 4-4. The EQE of a Pentacene:C_{60} solar cell.

To resolve this issue, we insert a thin layer of P3HT. P3HT has a shallower HOMO, allowing for charge extraction, yet larger singlet and triplet energies, blocking the migration of excitons to the ITO. With insertion of the P3HT, we observe an increase in EQE to 82%. Upon further investigation, this increase is due not only to the exciton blocking function, but also the fact that the pentacene crystallizes better on the P3HT. In Figure 4-5, we plot the x-ray diffraction intensity versus two theta for a 15 nm pentacene film with (a) the PEDOT:PSS-P3HT anode and (b) a bare ITO anode. The background amorphous x-ray scattering for each sample was subtracted using an appropriate control for ease of comparison. We clearly see significantly more diffraction from the pentacene film grown on P3HT. This suggests that non-crystalline pentacene has poor charge and/or exciton transport resulting in worse device performance. Indeed, reports of other pentacene solar cells find that PEDOT:PSS increases the crystalline content[64] and performance.[65]
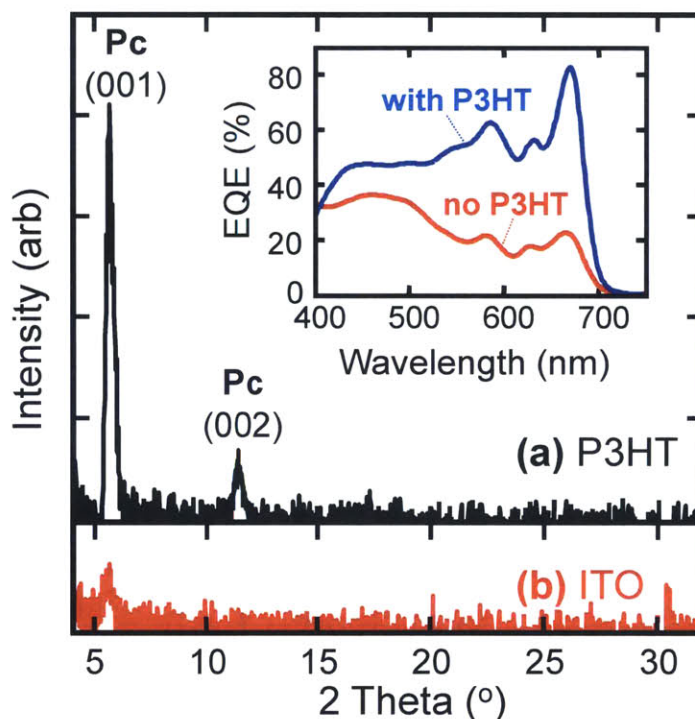
Figure 4-5. X-ray diffraction intensity from a 15 nanometer thick pentacene film deposited on (a) the PEDOT:PSS-P3HT anode and (b) oxygen plasma cleaned ITO. Inset are the EQE of the solar cells with PEDOT:PSS-P3HT (blue) and on bare ITO (red).

48
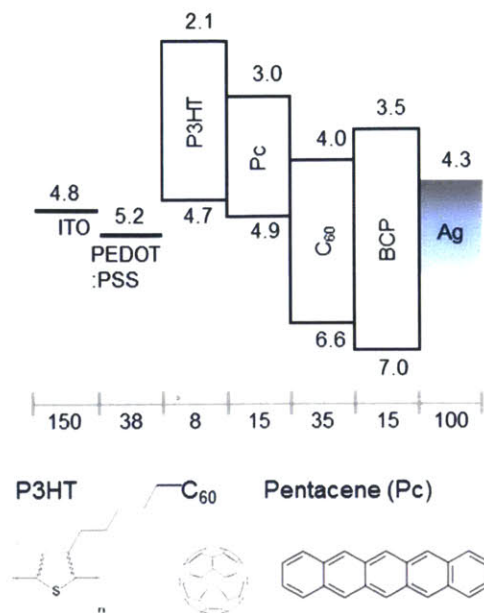
Figure 4-6. Chemical structures and architecture of the solar cell with the thickness of each layer in nanometers and energy levels of the lowest unoccupied and highest occupied molecular orbitals in eV.[51,66–70]

4.3.2. EQE greater than 100%

With the insertion of the P3HT layer, the final cell construction is shown in Figure 4-6. To characterize the cell, we measure the EQE and IQE as shown in Figure 4-7. The EQE at normal incidence is $(82\pm1)\%$ at the peak pentacene absorption wavelength $\lambda = 670$ nm. Optical modeling predicts that the internal quantum efficiency (IQE), which is defined as the number of electrons collected per photon absorbed, for photoexcitation of pentacene and P3HT is $(160\pm10)\%$ and $(150\pm10)\%$, respectively. The IQE of pentacene in this structure is approximately double that reported previously for pentacene,[63,66] and the high IQE of P3HT is consistent with the expected sensitization of P3HT by pentacene, as singlet excitons generated in P3HT are transferred to pentacene and then split into triplets. The EQE contributions of pentacene and P3HT are shown in cyan and magenta, respectively.
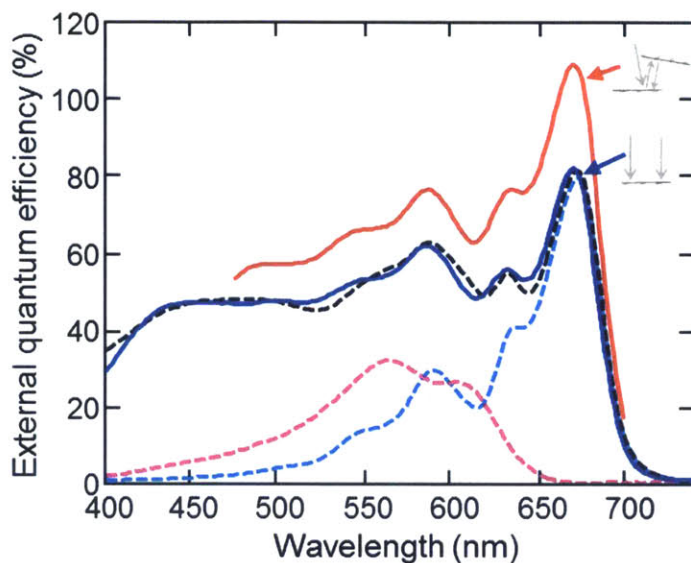
Figure 4-7. External quantum efficiency of devices without optical trapping (——), and device measured with light incident at 10° from normal with an external mirror reflecting the residual pump light (——). Optical fits from IQE modeling are shown with dashed lines: modeled pentacene EQE (– –), modeled P3HT EQE(– –), and modeled device EQE (– –) for comparison to the measured device efficiency without optical trapping.

The 15-nm-thick film of pentacene in the solar cell microcavity absorbs only 49% of the incident light at $\lambda = 670$ nm according to optical modeling and hence the efficiency should improve if a light-trapping scheme is employed. Therefore, we measured the EQE in configurations designed to simulate two conventional optical trapping schemes. The first scheme mounts the cell at 45° to the incident light, with a mirror that directs reflected photons back to the device. This configuration models a saw tooth geometry such that incident light bounces at least twice within the structure.[71,72] In the second scheme, the incident angle is reduced to 10° from the normal, modeling an optical collector that focuses light through a small hole in a mirror held parallel to the surface of the cell.[62] The peak EQE at $\lambda = 670$ nm for the solar cell mounted at 45° is (102±1)%, increasing to (109±1)% for incidence at 10° from the normal. Both light-trapping schemes yield efficiencies that meet or exceed the one electron per incident photon benchmark.

4.4. Current-Voltage Curve

The current-voltage characteristics of the planar pentacene solar cell are shown in Figure 4-8. The short circuit current measured at AM1.5 matches the integrated EQE measured at < 1 mW/cm^2 to within 6%, demonstrating that the fission process in pentacene is not significantly intensity dependent. As expected, the enhanced EQE does not correspond to a high power efficiency. The open circuit voltage is 0.36 V, identical to the values of previous pentacene devices. It is defined by the pentacene triplet energy of 0.86 eV.[31,50] Power efficiency is notably low at 1.8% for a device with such high EQEs. The reason for this is straightforward: as mentioned above, singlet fission materials require an external layer to absorb photons between the T_1 and S_1 states. There is no such absorption in this structure, so in doing singlet fission we halve the voltage of the cell while doubling the current. Future cells must provide this absorption, which can be provided by low-bandgap organic materials,[49] colloidal nanocrystals,[50] or traditional photovoltaic materials such as silicon.
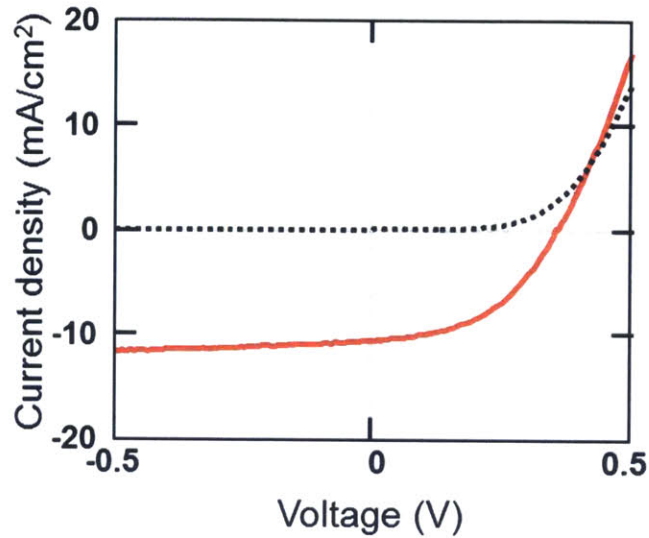
Figure 4-8. The current density-voltage characteristic of the pentacene solar cell measured under dark (– –) or AM1.5G 100 mW/cm2 (—) conditions without optical trapping. The power efficiency is (1.8±0.1)%.

4.5. Magnetic Field Effects

Independent confirmation of the high internal quantum efficiency within the cell is provided by analysis of the photocurrent under a magnetic field. The crucial rates are identified in Figure 4-9. The singlet exciton can either directly dissociate into a single electron-hole pair, k_S, or undergo fission resulting in generation of two electron-hole pairs, $k_{fis}(B)$. In absence of a magnetic field, three out of nine triplet-pair states have singlet character. Under a high magnetic field ($B > 0.2$ T), the number of triplet-triplet pairs with singlet character reduces to two, reducing the singlet fission rate, $k_{fis}(B)$. The photocurrent yield changes if there is effective competition between fission and the dissociation of the singlet exciton. Note that it is not possible to generate a magnetic field effect on the photocurrent yield unless there is a singlet loss mechanism that competes with the fission process.
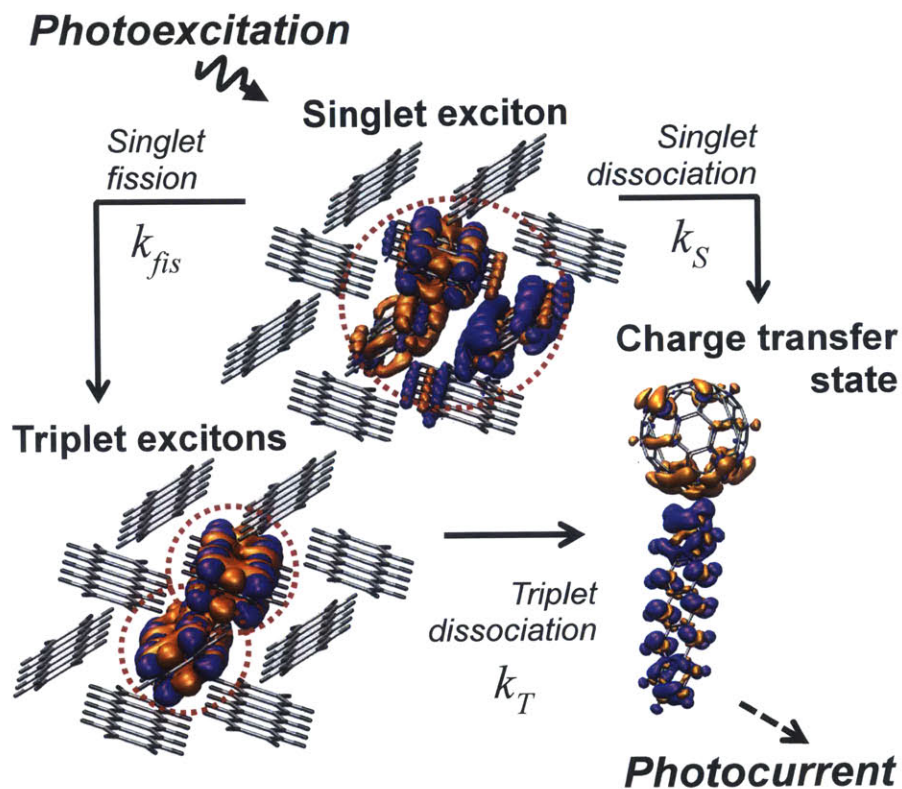
Figure 4-9. A schematic of singlet exciton fission in pentacene based on calculations of the singlet and triplet excitons and charge transfer states at the pentacene/fullerene interface, with the purple (orange) density indicating where less (more) electron density is found in the excited state. The delocalized singlet exciton and two localized triplet excitons are circled in red. The loss pathway for singlet excitons is direct dissociation into charge prior to singlet exciton fission.

To probe the system, we fabricate a range of devices and measure the change in photocurrent as a function of the magnetic field. Two example curves are shown in Figure 4-10 for a solar cell and a photodetector. The photodetector structure is a set of thin layers of C_{60} and pentacene stacked sequentially to allow for very thin layers.
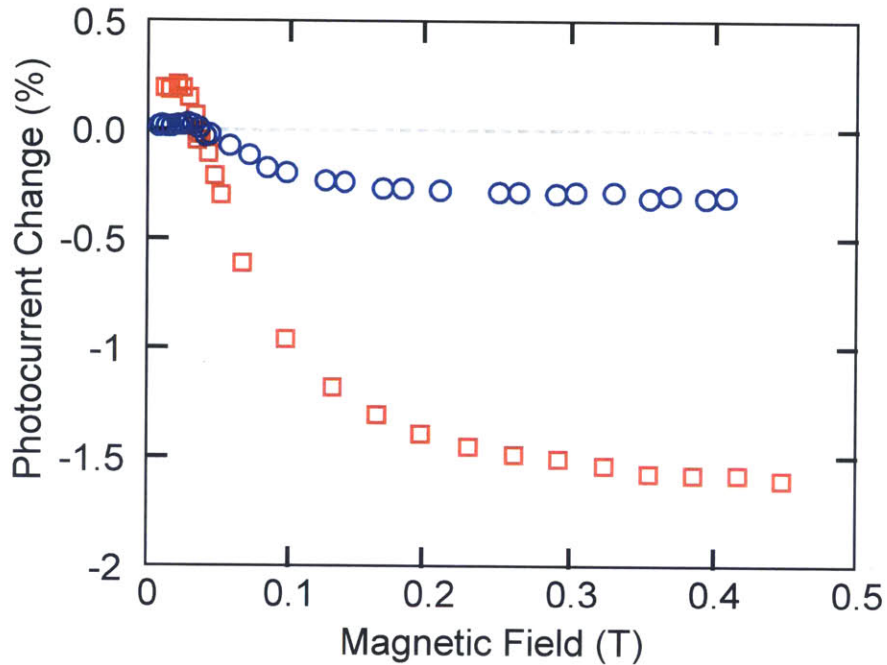
Figure 4-10. Change in photocurrent as a function of external magnetic field for a photodetector (□) and a solar cell (○). The photodetector curve was taken at a reverse bias of −4 V. Both curves first increase and then decrease before saturating at magnetic fields greater than 0.4 T. The large difference in the change in photocurrent observed at B = 0.4 T is due to the increased dissociation of the singlet into charge in the photodetector structure.

4.5.1. MFE Model

Two critical rates control the efficiency of the fission process: the direct breakup of the singlet exciton into a charge transfer state and fission into two triplets. The fission rate is independent of thickness, while singlet breakup involves both exciton diffusion to the interface and exciton dissociation and therefore varies with thickness. Because the fission rate is magnetic field dependent, we can apply a magnetic field to determine the efficiency of fission in devices. A change in the photocurrent will only be detected when these rates are competitive. At extremely thin layers, we expect singlet breakup to outcompete fission by a wide margin, so slowing the fission rate will not affect the photocurrent. Alternatively, at extremely thick layers we expect fission to be much faster than exciton diffusion and breakup, so that slowing the fission rate a

moderate amount will not change the rate; i.e. all excitons still have time to fission. It is in between these two extremes that we examine by varying the pentacene thickness.

To quantify our intuition, we develop a model based upon the Merrifield model.[25,26,73] Knowing how the rate of fission depends on the magnetic field, we can update our kinetic to that in Figure 4-11.
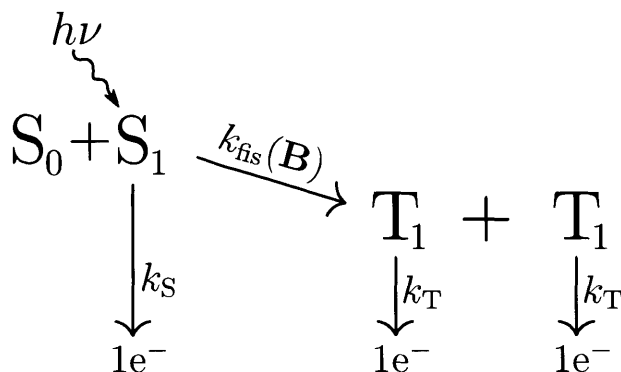
Figure 4-11. Simplified kinetic scheme of singlet fission.

Thus, we generate an expression relating the photocurrent $I(B)$ to the rate constants:

$$I(B) \propto \frac{k_{out}}{\phi}\left[\,e^-\,\right] = \frac{k_S}{k_{fis}(B) + k_S} + 2\frac{k_{fis}(B)}{k_{fis}(B) + k_S} \qquad (4.3)$$

For convenience, we write $k_{fis}(B) = \chi(B)k_{fis}^0$, where $\chi(B)$ is the modulation of the zero-field fission rate k_{fis}^0 due to an external magnetic field. The normalized change in photocurrent is thus given by

$$\delta = \frac{I(B) - I(0)}{I(0)} = \frac{k_S k_{fis}^0 (\chi - 1)}{\left(2k_{fis}^0 + k_S\right)\left(\chi k_{fis}^0 + k_S\right)} \qquad (4.4)$$

55

where $I(B)$ is the photocurrent as a function of magnetic field strength. Dissociation of the singlet exciton directly into charge is only likely to compete with fission for pentacene molecules directly adjacent to the acceptor. Indeed, reductions in the singlet exciton lifetime of pentacene have been observed in very thin pentacene films (0.6 monolayer) adjacent to a C_{60} layer.[41] Thus, we can approximately model pentacene films of varying thickness by changing the effective rate of singlet dissociation.

Analytically, we can solve for χ at a given value of the magnetic field by noting that the magnitude of δ is maximized when $k_S = k_{fis}^0 \sqrt{2\chi}$. This yields:

$$\chi = \frac{2\delta_{max}^2 + \delta_{max} + 1 + 2\sqrt{2}\delta_{max}\sqrt{\delta_{max}+1}}{\left(\delta_{max}-1\right)^2} \qquad (4.5)$$

The result for χ can be used to directly obtain the triplet yield of singlet fission from the magnetic field modulation in photocurrent:

$$\eta_{fis} = \frac{2}{1+k_S/k_{fis}^0} = \frac{(1-\delta)\chi - 1 \pm \sqrt{\left(\delta(\chi+2)-\chi+1\right)^2 - 8\delta^2\chi}}{(\delta+1)(\chi-1)} \qquad (4.6)$$

4.5.2. MFE Measurements

To obtain an independent measure of the yield of singlet fission, we fabricated multiple devices while varying the thickness of pentacene, see Figure 4-12. For thin layers of pentacene (d < 5 nm) we increased the optical absorption by employing the multilayer photodetector architecture.[62,74] Photodetectors were measured in reverse bias to improve charge extraction. As a test of generality, both C_{60} and 3,4,9,10-perylene tetracarboxylic bisbenzimidazole (PTCBI) were used as acceptor molecules and found to yield similar results. Devices with thicker layers of pentacene employed the same device architecture as Figure 4-6. The magnetic field modulation of

photocurrent at 0.4 T is shown in Figure 4-12(a). It peaks at $\delta_{max} = -(2.7\pm0.1)\%$ in 2-nm-thick layers of pentacene sandwiched between acceptor layers. From Eq. 4.5, we obtain $\chi = 0.85$, identical to the value assumed in *Ref* [74] based on tetracene measurements.

In Figure 4-12(b) we apply Eq. (4.6) to transform the magnetic field modulation data into the expected yield of triplet excitons from singlet fission. We find that singlet fission is incomplete in pentacene films with thickness $d < 5$ nm, accounting for the relatively low IQE in the photodetector structures. The triplet yield approaches 200% in thicker films, providing independent confirmation of the high IQE calculated for the device structure shown in Figure 4-6.

The IQE, as discussed above, is shown in Figure 4-12(c) and compared to predictions based on the magnetic field effect. The IQE is suppressed in thin layers of pentacene, increases to a maximum for $d \sim 15$ nm, and then is reduced in thicker films. Decreases in IQE for thicker films are presumably due to triplet exciton diffusion limitations and lower than unity charge collection efficiency. There are two important conclusions from this IQE comparison. First, the yield of singlet fission can be conveniently determined directly from the normalized change in photocurrent under a magnetic field. A high yield is characterized by a vanishing modulation of photocurrent under magnetic field. Second, singlet fission in pentacene requires a relatively thick film to minimize losses due to singlet exciton dissociation. Fission is not effective in fine-grained blends of pentacene and fullerene or perylene-based acceptors.
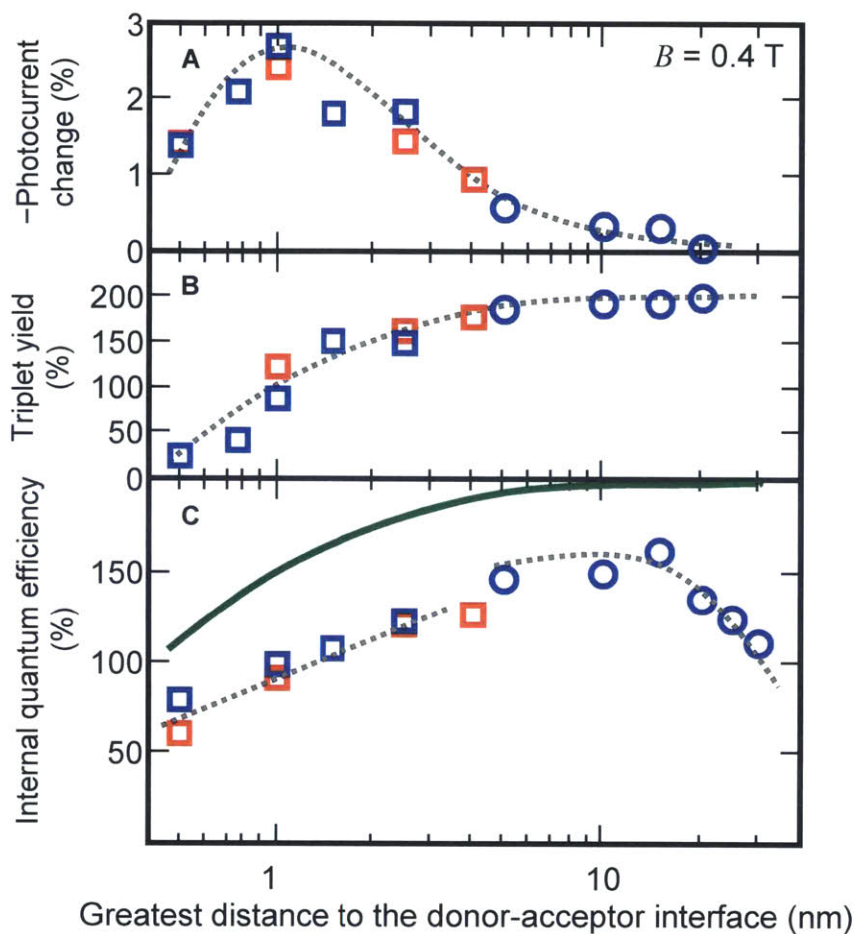
Figure 4-12. (a) The magnetic field dependent change in photocurrent measured at B = 0.4 T as a function of pentacene layer thickness. Square symbols are measured in photodetector structures and each pentacene layer is sandwiched between C60 (□) or PTCBI (□) acceptor films. Measurements in the solar cell architecture are circles (○). (b) The triplet yield from singlet exciton fission.. (c) A comparison of the maximum achievable quantum yield determined from the magnetic field effect (—) with the internal quantum efficiency as determined from EQE measurements and the calculated optical absorption. The reduction in quantum efficiency observed in thin layers of pentacene is found to originate in incomplete singlet exciton fission. Grey dashed lines are a guide to the eye.

Finally, we note that while Merrifield's theory allows one to calculate $\chi(B) = k_{fis}(B) / k_{fis}^0$ from first principles, it requires knowledge of the zero-field-splitting parameters D and E in the Hamiltonian for pentacene triplet excitons and also the ratio k_{-1}/k_2. These were fitting parameters in Merrifield's work. As shown above, we were instead able to obtain an expression for $\chi(B = 0.4$

T) requiring only the experimental values of δ_{max} at $B = 0.4$ T. This leads to an expression that gives the fission yield of a device simply by measuring its δ at $B = 0.4$ T. We do not need to calculate or fit the line shapes of the change in photocurrent versus magnetic field.

Implicit in our model is the assumption that $\chi(B)$ is invariant with pentacene layer thickness. This assumption might break down for very thin layers (< 2 nm) of pentacene, as χ represents a balance of the forward and backward rates linking the singlet exciton and the triplet-triplet pair. Direct dissociation of the triplet-triplet pair would alter the balance and increase $\chi(B)$ closer to one, resulting in a change in photocurrent trending toward zero as the pentacene layer thickness is decreased. Nevertheless, we assume that the change in $\chi(B)$ for very thin pentacene films is small because triplet dissociation into charge (~400 fs) is slower than singlet fission (80 fs) for pentacene monolayers on C_{60}.[41]

4.5.3. Tetracene Efficiency

Finally, these experiments were repeated for tetracene.[54] Compared with pentacene, singlet fission in tetracene is much slower, on the order of 90 ps.[44] This has potentially profound device implications – more time needed for fission to occur means greater thicknesses of tetracene are needed to achieve high EQEs. Indeed, this is the case, as shown in Figure 4-13. The magnetic field effect on photocurrent peaks at larger distances to the interface, and we do not see high (>150%) triplet yields until almost 30 nm thick films, an order of magnitude higher than that of pentacene. This is reflected in the relatively low IQEs in the tetracene system, Figure 4-13(d).
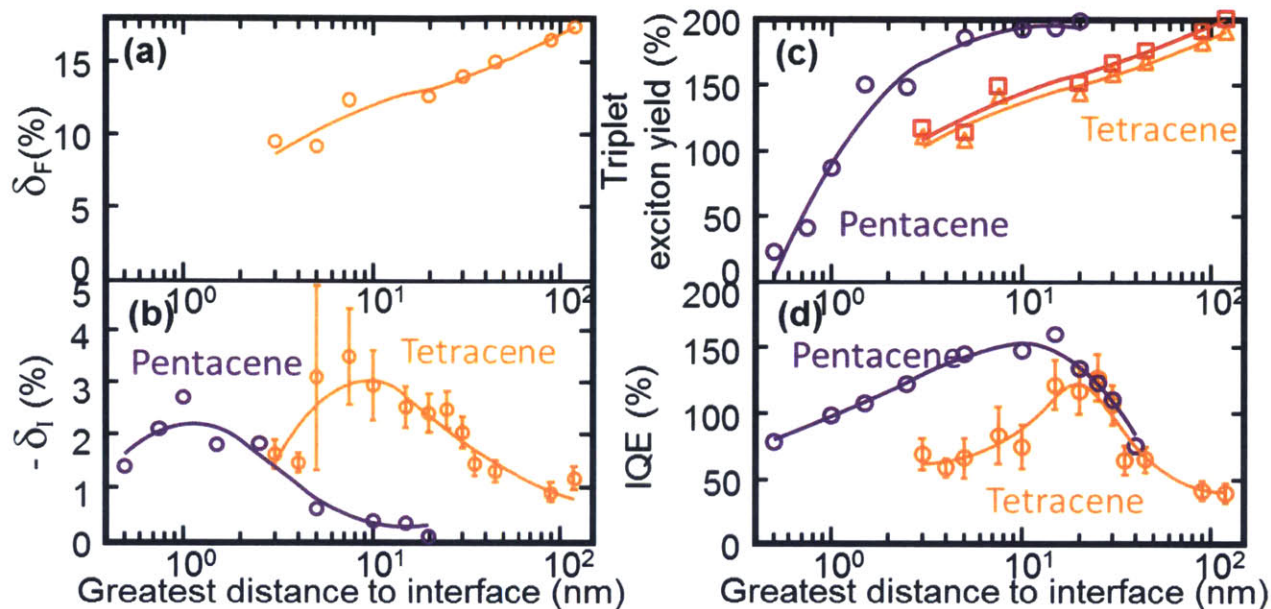
Figure 4-13. Efficiency of singlet fission in tetracene. (a) Fluorescence magnetic field effect as a function of distance to the interface. (b) Photocurrent magnetic field effect. Compared with pentacene, tetracene peaks at greater distances, signifying a slower fission rate. (c) Triplet yield calculations. Slowing fission results in more singlet breakup, reducing the triplet yield. (d) IQE calculations. A reduced triplet yield leads to a reduction in IQE as compared with pentacene. Data from Tony Wu.[54]

4.6. Slow Light Absorption Enhancement

In order to improve the efficiency of singlet fission devices, absorption must be increased, but thickening the pentacene layer leads to exciton diffusion losses, while utilizing a blend results in incomplete fission. Light management, however, is a feasible method to improve absorption within thin pentacene layers. Enhanced absorption has been observed for structures including micro-lens arrays[75], pyramidal reflectors[76], non-planar substrates and V-shaped structures[71], Distributed Bragg Reflectors (DBR)[77], and plasmonic structures[78]. Almost all of these approaches require transparent/semi-transparent cathodes or growing the organic solar cell on structured substrates. In contrast, we demonstrate a simple approach for enhancing absorption in thin film

organic solar cells by exploiting the slow light modes that appear at the band edge of a DBR. Using this approach we show over a 50% enhancement in absorption and external quantum efficiency (EQE) of singlet exciton fission based solar cells.
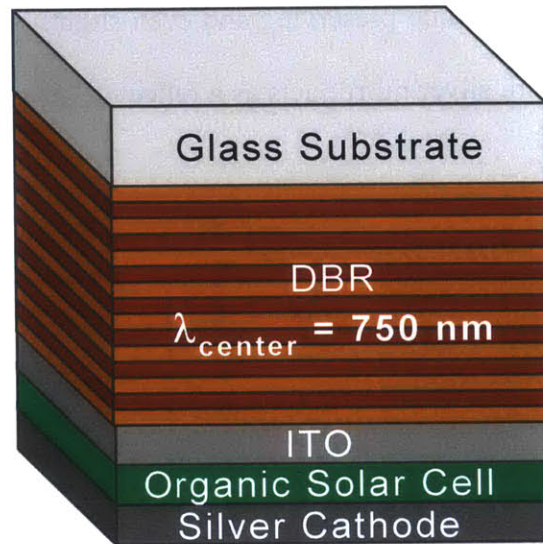
Figure 4-14. Schematic diagram of distributed Bragg reflector light management system and organic solar cell.

The placement of the DBR between the glass substrate and the ITO anode, shown in Figure 4-14, achieves absorption enhancements in the organic solar cell without increasing the solar cell device fabrication complexity. The absorption enhancement, highlighted in Figure 4-15(a) and (b), arises due to the presence of long lived slow light modes that exist at the bandedge and the associated increase in photon density of states. The dwell time calculated from the phase change per unit frequency of the reflection coefficient of the transmission matrix is plotted as a function of wavelength is shown in Figure 4-15(c). We see that the high frequency bandedge mode increases the photon dwell time (effective interaction length) between the absorbing organic layers and light by a factor of 2.7. This agrees closely with the factor of 2.5 increase in absorbance observed in the

solar cell with the DBR. The DBR is designed to have the high frequency band edge overlap with the spectral position of the singlet exciton absorption of pentacene. The intensity distribution for λ = 670 nm is shown in Figure 4-15(d) where the ITO thickness is chosen to place the intensity maximum in the spatial position of the pentacene layer. These factors result in an enhancement of the absorption at the band edge while preserving and even slightly enhancing the absorption at higher frequencies. The bottom silver mirror acts as a reflector, providing additional optical path length.
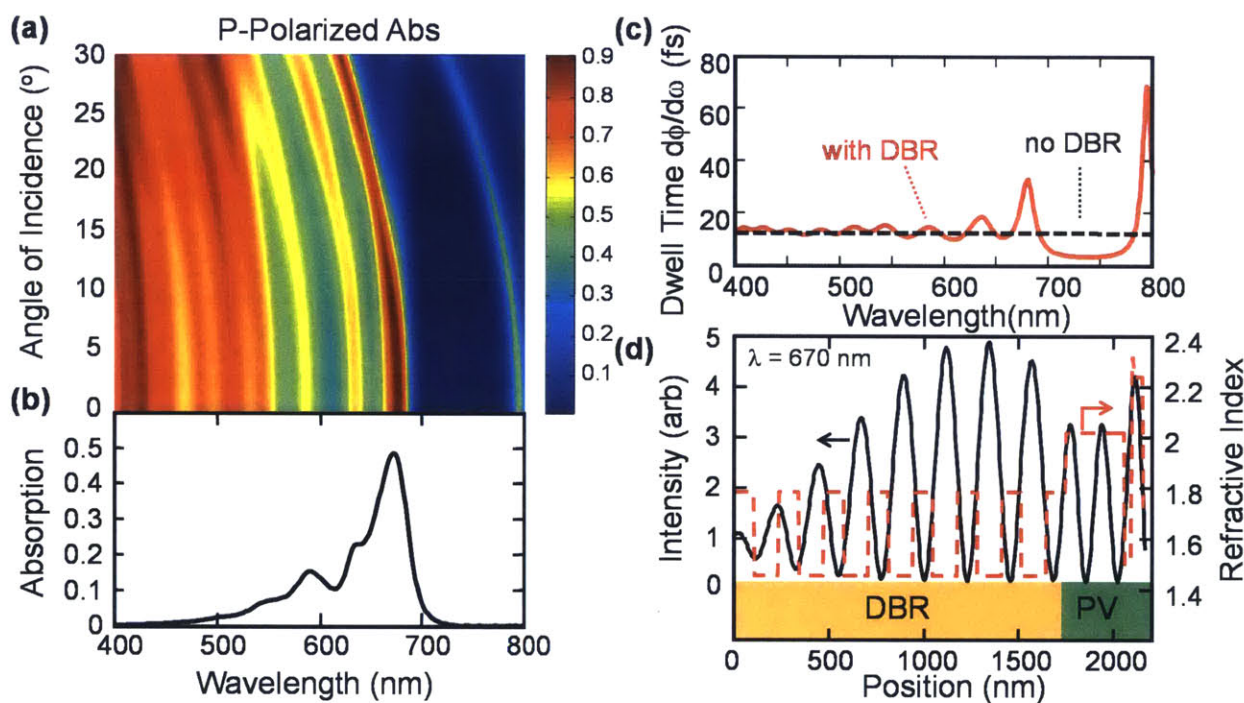
Figure 4-15. Modeled p-polarized absorption of (a) the DBR enhanced solar cell as a function of angle incidence and (b) pentacene within the solar cell cavity at normal incidence without the DBR. (c) Dwell time as a function of wavelength. The solid red line corresponds to the solar cell with the DBR and the dashed black line is without. (d) Light intensity and refractive index for λ = 670 nm plotted as function of position for the solar cell with the DBR light management system.

Due to the dispersion of the DBR, the absorption enhancement shifts to higher frequencies for angles off normal incidence as shown in the simulated device absorption in Figure 4-15(a). The band edge can be spectrally tuned by tilting the device relative to the incident light. To ensure larger angular tolerance, the DBR was designed to intentionally have absorption maximum at λ = 679 nm which is slightly red shifted from the absorption maxima of pentacene. When the DBR band-edge mode is tuned to the peak wavelength of pentacene's extinction coefficient we observe an EQE peak of $126\pm1\%$, see Figure 4-16. A control solar cell fabricated identically but without the DBR, achieved a peak EQE of only 83% and exhibited nearly zero change in EQE with angle. The DBR enhanced device demonstrated EQE greater than 100% for incident angles over the range +/- 27°, with a relatively flat response; see inset of Figure 4-17. Device EQE measurements were performed with a spot size significantly smaller than the device area such that no light was lost from the solar cell when the device was turned.
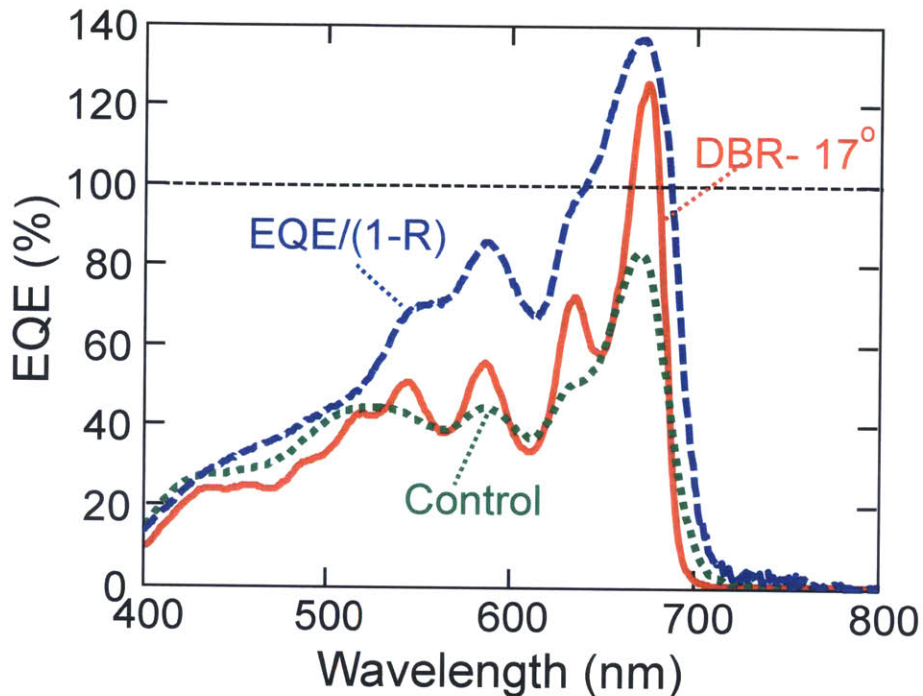
Figure 4-16. External quantum efficiency for a slow light DBR cavity (solid, red) at which the DBR absorption is tuned to maximize the absorption in pentacene. The control device (dotted, green) is without the DBR. The EQE divided by 1 minus the reflection (dashed, blue) provides a lower bound on the internal quantum efficiency.

The DBR band edge also provides a convenient way to accurately measure the minimum internal quantum efficiency (IQE) in an organic solar cell. The conventional method for determining IQE is to measure the EQE of the solar cell and then calculate the absorption in the device, using a transfer matrix method or otherwise[62] as discussed above. Measuring the absorption of the device directly is possible but properly attributing the amount of absorption occurring in each layer is difficult, with losses in the metal[79] requiring special attention. As we can see from optical modeling in Figure 4-15(a), with the DBR the predicted absorption for the device exceeds 80% for a significant range of incident angles. In contrast, a device without the DBR has a maximum pentacene absorption of nearly 50% for normal incidence, Figure 4-15(b). We performed a measurement of the reflection from the device at the angle of peak EQE, eliminating

the need to model the device absorption. In Figure 4-16 we plot the EQE divided by 1-*R*, where *R* is the reflection, and find a peak EQE/(1-*R*) of 137%. Including calculations of the loss of photons due to metal absorption leads to an IQE of 147%. A full transfer matrix calculation finds an IQE of 155±10% across all angles of incidence, in agreement with the IQE measured previously for this device.[53]
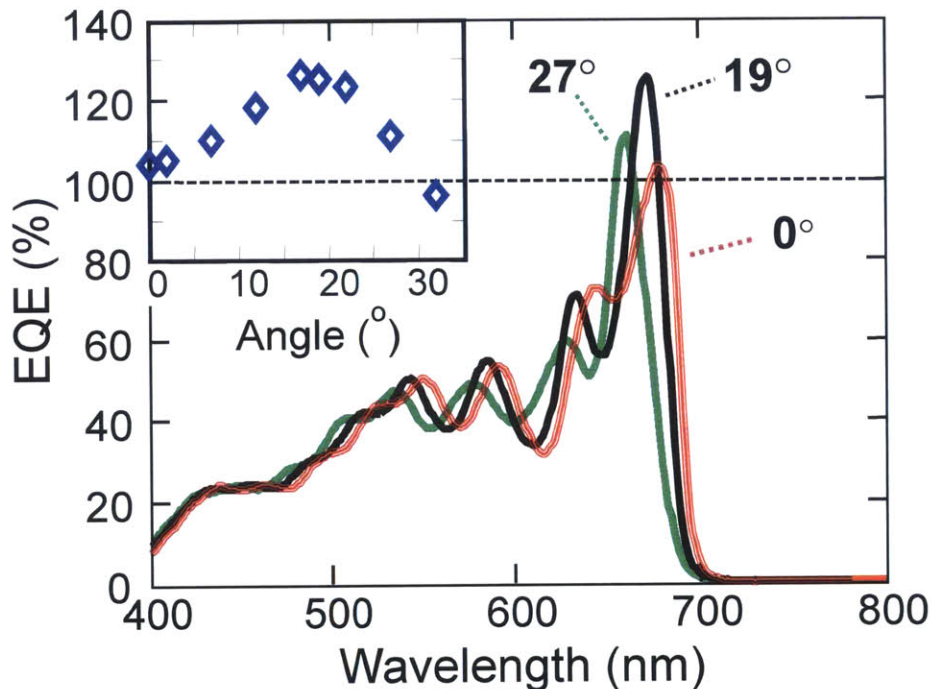
Figure 4-17. EQE as a function of wavelength for 0, 19, and 27 degrees angle of incidence on the DBR solar cell. Inset is the peak EQE as a function of angle of incidence in diamond symbols using the same y-axis.

Achieving high singlet fission efficiencies in a solar cell performance requires optimizing the tradeoff between insufficient absorption in thin films, and exciton diffusion losses in thicker films[62]. Use of a DBR band edge mode optical structure alleviates the constraint in planar pentacene solar cells, pushing the absorption in pentacene close to 80%, and significantly simplifying the calculation of the minimum IQE. The final EQE result of 126% at $\lambda = 670$ nm

should solidify singlet exciton fission as a realistic contender in the race to push mainstream solar cells beyond single junction efficiency limits.

4.7. Fission Sensitization of Non-Fission Materials

Although singlet fission holds great potential to help solar energy conversion, most singlet fission materials are not effective solar cell materials. Therefore, we would like to orthogonalize singlet fission from the rest of photovoltaic processes such as absorption, exciton diffusion, and charge transport. To that end, we develop the device shown in Figure 4-18.[56] The device is designed for the rubrene singlet fission layer to sensitize the TPTPA layer to singlet fission as follows. Photons are absorbed in the TPTPA layer and transfer to the rubrene layer, where the excitons undergo singlet fission. In this way, the rubrene can be kept exceedingly thin (5 nm in this device), yet singlet fission can occur for a large number of photons. PDI-CN2 was used as an acceptor because of its ability to break up the rubrene triplet.
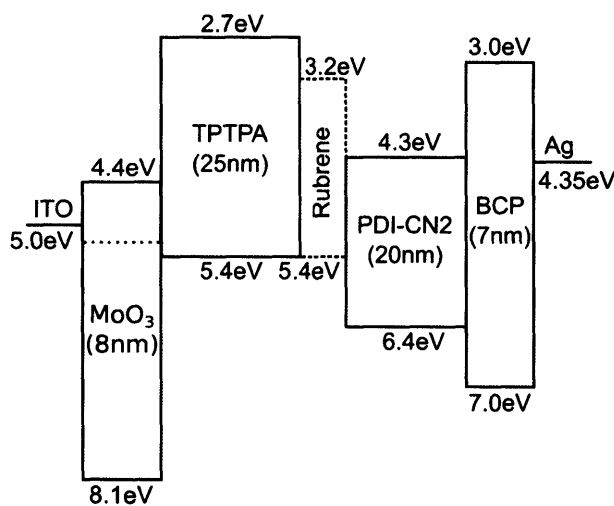
Figure 4-18. Band structure of singlet fission sensitized device.

Evidence for singlet fission sensitization can be found in Figure 4-19. TPTPA is the sole material absorbing between 350 and 450 nm. The EQE of this material doubles upon insertion of the rubrene. Because no other material absorbs in that region, the current increase must be due to an increase in TPTPA photocurrent. The increase in EQE in the 500 nm region is due to the absorption of the rubrene. The sensitization is further confirmed by the magnetic field effect in Figure 4-19(b). Without rubrene in the device, there is no magnetic field effect (dashed lines). When the rubrene is inserted, we see the classical singlet fission signature. Exciting the rubrene with 500 nm light shows direct excitation magnetic field effect. 365 nm excitation exclusively excites the TPTPA. The only way a magnetic field effect can be observed is through the proposed sensitization mechanism. The reduced magnitude for the rubrene curve is due to the fact that PDI-2CN also absorbs at 500 nm, contributing field-independent current and thus reducing the overall magnitude of the delta.
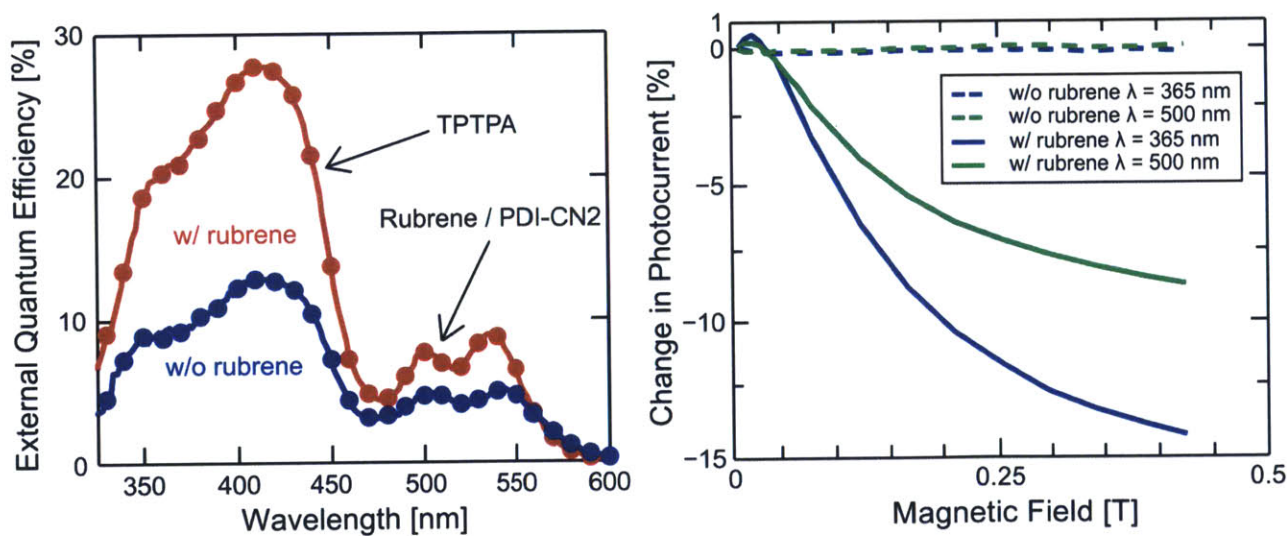
Figure 4-19. EQE and magnetic field effects for the rubrene sensitized solar cells.

The P3HT/pentacene system was also examined for sensitization. Unfortunately, due to the overlapping absorption of the various layers it is not trivial to prove the sensitization effect. To examine more closely, we measure the magnetic field effect at high fields as a function of wavelength (see Figure 4-20). If the P3HT was not being sensitized, the magnetic field effect should only trace the pentacene photocurrent, while sensitization should lead to the magnetic field effect tracing both the P3HT and pentacene contributions. From inspection of Figure 4-20, it is apparent that the P3HT is indeed sensitized, confirming its high IQE as calculated in the previous section. Sensitization has been shown to be a powerful tool for implementing highly efficient singlet fission solar cells.
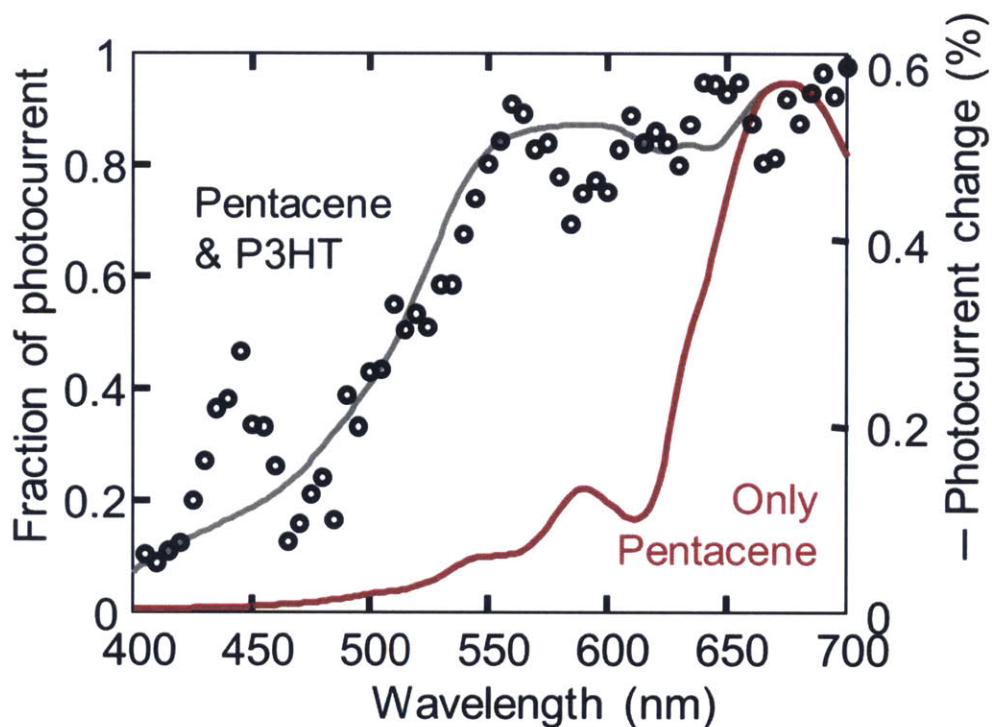
Figure 4-20. Magnetic field effect as a function of wavelength in the P3HT/pentacene system. The magnetic field traces the sum of the current from the pentacene and P3HT, demonstrating that singlet fission is occurring for excitons generated in both layers.

Chapter 5: Making Triplet Excitons Bright

5.1. Introduction

Although we demonstrated that singlet fission can be quite efficient in devices, the spin 1 final state is challenging to couple to an inorganic material such as silicon. In this chapter, we investigate the use of colloidal nanocrystals to act as a mediating layer – accept the triplet exciton and fluoresce utilizing the strong intersystem coupling in those systems. We show that these inorganic nanocrystals are an especially effective means of harvesting non-emissive triplets with energies in the infrared, allowing us to 'brighten' the triplet for use in many applications including transfer to silicon. The following is adapted from reference [80].

5.2. Materials and Methods

In this section we describe the synthesis procedures for our devices, as well as the experimental method for our optical measurements.

5.2.1. PbS Colloidal Nanocrystal Synthesis

The lead sulfide nanocrystal (NC) synthesis was adapted from Zhao et al.[81] Specifically, lead(II) acetate trihydrate (11.38 g, 30 mmol), 1-octadecene and oleic acid (varied quantities as designated by Table 5-1) were degassed in a 1000 ml three-neck round-bottom flask at 100 °C until the solution turned clear. The solution was cannula transferred to a nitrogen-flushed 1000 mL four-neck round-bottom flask equipped with a mechanical stirrer. Under nitrogen flow, the solution was heated to the injection temperature (see below), at which point a mixture of bis(trimethylsilyl)sulfide (3.15 ml, 15 mmol) in 1-octadecene (150 ml) was rapidly injected. The

resulting nanocrystals were transferred to a nitrogen glovebox where flocculation was performed

three times with anhydrous butanol, methanol, and/or acetone. The nanocrystals were redispersed

in hexanes or octane.

First absorption feature (nm)	Quantity in reaction pot (ml)		Injection temp (°C)	Growth time (s)	Flocculation solvent
	1-octadecene	oleic acid			
931	300	21	120	0	acetone
1010	263	37	150	30	butanol and methanol
1135	225	75	150	60	butanol and methanol
1308	150	150	150	30	butanol

Table 5-1. Synthesis conditions for the colloidal nanocrystals.

5.2.2. Sample Fabrication

The glass substrate was cleaned by sequential sonication in Micro90 detergent solution,

deionized water, and acetone, after which it was immersed in boiling isopropanol and then dried

under a stream of pure N_2. The nanocrystals and substrates were loaded into a dry nitrogen

glovebox with H_2O and O_2 concentrations less than 1 ppm. Solutions of oleic acid (OA) capped

nanocrystals dissolved at 25 mg/mL in octane were spin-cast onto the cleaned soda lime glass at a

speed of 2500 rpm and a ramp rate of 2000 rpm/s for a total of 60 seconds. For ligand exchanged

samples, the single layer of nanocrystals was exposed to a 0.01 M solution of ligand in

acetonitrile.[82] The exposure time varied between 30 seconds to 30 minutes. After exposure, the

excess ligand was removed by three rinse cycles with pure acetonitrile. The resulting nanocrystal

layer is 50.0 +/- 5.4 nm thick.

Tetracene layers were thermally evaporated at pressures less than 3×10^{-6} Torr at rates between 1 and 3 Å/s. The thermal evaporator is directly attached to the glovebox. The tetracene was purchased from Sigma-Aldrich and purified three time by vacuum sublimation before use. Samples were packed in the pure nitrogen glovebox using UV-curing epoxy and a second glass substrate. Care was taken to shadow the active area of the substrates with Al foil during UV exposure.

5.2.3. Excitation and Absorption Measurements

Photoluminescence excitation spectra were taken on the packaged samples. Briefly, a 250 W tungsten lamp was filtered by a monochromator with a spectral resolution of 4 nm at full width half maximum. Long pass filters were used to eliminate second harmonic light from the monochromator. The incident light was mechanically chopped at a frequency of 270 Hz. The sample was illuminated at either 30 or 45 degrees from normal incidence, and emission normal to the sample was captured in free space with a lens. The signal from an InGaAs detector was coupled to a lock-in amplifier. Appropriate short and long pass filters were used to eliminate stray pump light and emission from tetracene.

Absorption measurements were performed with the same lamp, monochromator, and chopping scheme but in an integrating sphere. The angle of incidence during absorption was matched to that during excitation.

Magnetic field effects were measured as described in Section 4.2.5.

5.2.4. Transient Measurements

In the default configuration for time-resolved single-photon counting, samples (identical to those used in steady state spectroscopy) were excited by a train of 532 nm, 63 ps-duration pulses at a repetition rate of 200 kHz generated by a PicoQuant LDH-P-FA-530B. The considerable waiting time between pulses (5 μs) was essential to allow the delayed fluorescence – consistent with a small, residual population of long-lived, isolated/trapped triplets, as well as long-lived 'trap' states on the nanocrystals – to decay to the noise floor of the detector. ($<10^{-3}$ of the peak signal in this configuration) The pump was attenuated to yield pulses with an irradiance of ~20 pJ/cm^2, such that the photoexcitations from a single pulse had an average separation > 50 nm in either tetracene or the film of PbS nanocrystals. Under these conditions the photoluminescence decay dynamics were independent of excitation intensity. Accordingly, we consider bimolecular recombination channels to be unimportant.

The short-wave infrared (SWIR) emission from the PbS nanocrystals was collected and imaged onto an InGaAs/InP single-photon counting avalanche photodiode (Micro Photon Devices $IR-DH-025-C), fitted with a long-pass filter (Chroma Technology Corp.) to suppress the scattered photons from the visible pump. The arrival times of all photons were recorded using a PicoQuant Picoharp in T2 (time-tagged, time-resolved) mode, and the decay traces were generated by correlating the photon arrivals with the sync pulse from the laser using custom software. The aggregate time resolution, judged from the onset of the response to unfiltered pump scatter, was ~300 ps. This stemmed primarily from the uncertainty in the detector response at the low over-voltages required for low-noise operation.

5.2.5. Ultraviolet Photoelectron Spectroscopy

Films of oleic acid capped PbS colloidal nanocrystals were spin cast from an approximately 125 mg/mL solution in an oxygen- and water-free glovebox onto glass substrates coated by thermal evaporation with Cr (10 nm) / Au (100 nm) anodes. The samples were then ligand exchanged with hexanoic acid as described previously. Conductive carbon tape was used to make electrical contact between the Cr/Au anode and a stainless steel sample plate. Samples were transported from the glovebox to an ultrahigh vacuum chamber (10^{-10} mbar base pressure) without exposure to air using a load-locked transfer system. Ultraviolet illumination at 21.22 eV was provided by a He(I) discharge lamp, and emitted electrons were collected at an escape angle of 0° from substrate normal and measured using an Omicron electron spectrometer. Samples were biased at -5.0 V to enable accurate determination of the low-kinetic-energy cutoff. Single scans were collected in <60 seconds to minimize charging and UV-induced degradation of the sample. The Fermi level and valence band binding energy were determined from the intercept of a linear extrapolation of the deep- and shallow-binding energy cutoffs, respectively, to a linear extrapolation of the baseline. The instrumental accuracy of UPS is ~0.1 eV.[70]

The conduction band energy was determined by subtracting the optical bandgap energy (0.95 eV, determined from the energy of the first excitonic peak in the optical absorption spectrum of a ligand-exchanged PbS NC film) and a correction for the exciton binding energy from the valence band energy, such that

$$E_C = E_V - E_g^{opt} - 1.786\frac{e^2}{4\pi\varepsilon_0\varepsilon_{NC}R}$$

(5.1)

where e is the charge of the electron, ε_0 is the permittivity of free space, ε_{NC} is the optical dielectric constant of the nanocrystal core material (ε_∞^{PbS} = 17.2), and R is the quantum dot radius (determined by matching the first absorption peak in solution to a published sizing curve).[83,84]

5.3. Device Structure

The proposed triplet energy transfer process is depicted schematically in Figure 5-1. We employ Lead (II) Sulfide (PbS) colloidal nanocrystals as the inorganic semiconductor acceptor for a non-emissive triplet exciton. Triplet excitons are generated in tetracene via singlet fission, which produces dark[85] triplet excitons rapidly (τ < 200 ps)[44,86,87,59] and at yields approaching 200% in neat films.[43,54] The respective energy levels of tetracene and the nanocrystals as determined by ultraviolet photoelectron spectroscopy (UPS) are shown in Figure 5-2(a). The interface between tetracene and the nanocrystals is a type I heterojunction. Further, excitonic energy transfer is energetically preferred over two consecutive charge transfers since both of the possible charge transfer intermediates are expected to have higher energies than the initial tetracene triplet energy (1.25 eV).[42,51,88]. The morphology of the sample is shown in Figure 5-2(b). It consists of several monolayers of PbS nanocrystals that are coated with a thermally-evaporated layer of tetracene. The tetracene layer is quite rough and consistent with Stranski-Krastanov growth of an initial inhomogeneous coating of tetracene followed by island formation.
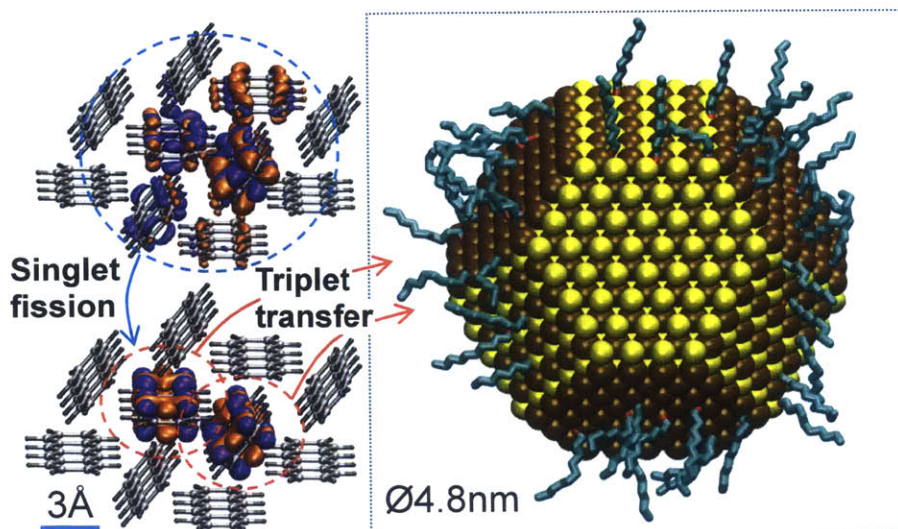
Figure 5-1. Schematic of triplet exciton transfer from tetracene to a PbS nanocrystal with decanoic acid ligands. Singlet excitons in tetracene first undergo singlet fission then triplet transfer to the nanocrystal. The tetracene simulations are from Ref. [54]. Note that the figure is not to scale; the tetracene molecules have been expanded relative to the nanocrystal to show the excitonic states.
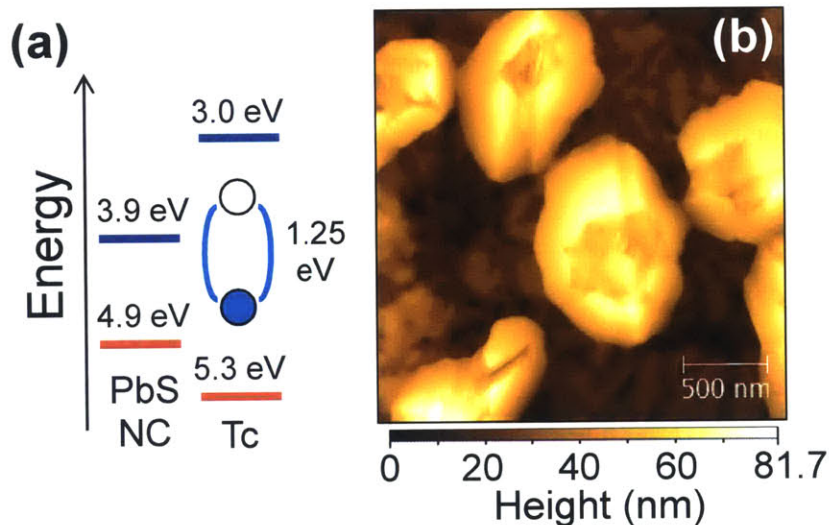
Figure 5-2. (a) Energy level diagram of the tetracene-PbS nanocrystal interface, with the tetracene HOMO (red) energy from UPS measurements[89] and a lower bound for the LUMO (blue) energy obtained by adding the singlet energy from the emission peak.[43,44] This method does not account for Coulombic stabilization. Nanocrystal valence (blue) and conduction (red) band energy levels are from UPS measurements, and are accurate to within 0.1 eV. The tetracene triplet exciton is schematically represented by a bound electron and hole within the energy gap of tetracene. The tetracene triplet exciton energy is 1.25 eV.[42,51,88] (b) AFM micrograph of the tetracene layer on PbS nanocrystals.

5.4. Photoluminescence Quantum Yield (PLQY) Measurements

Energy transfer from tetracene is probed by measuring the near-infrared emission from the nanocrystals while preferentially exciting the tetracene layer. In Figure 5-3(a) we measure the excitation spectrum of a thin film of PbS nanocrystals coated with a 20-nm-thick film of tetracene. The absorption spectra of tetracene and the nanocrystals are distinct, with PbS absorption dominant at longer wavelengths ($\lambda > 550$ nm), and PbS and tetracene both absorbing at shorter wavelengths ($\lambda < 550$ nm); see Figure 5-3(b). The absorption of tetracene is structured, with three characteristic peaks in the blue-green spectrum.[44,90] Thus, the appearance of tetracene peaks in the excitation spectrum of PbS nanocrystal luminescence confirms energy transfer from tetracene to the nanocrystals.

To control the yield of exciton harvesting, we note that the rate of energy transfer generally increases with decreasing distance between the donor and acceptor.[91,92] Our PbS nanocrystals are synthesized with insulating oleic acid (OA) ligands, which passivate surface traps and provide solubility in organic solvents. In the solid state, however, the ligand acts as a spacer between the nanocrystals and the tetracene. Using solid-state ligand exchange, the OA ligand can be replaced with a number of shorter alkyl carboxylic acid derivatives.[82] We highlight two examples in Figure 5-3, decanoic (capric) acid (DA) and caprylic (octanoic) acid (CA). As shown in Figure 5-3(a), both ligands result in improved energy transfer, demonstrated by the increased excitation efficiency in the regions of tetracene absorption. Decreasing the ligand length reduces the quantum yield of the nanocrystals, however. The typical quantum yield of our films of OA-functionalized nanocrystals is approximately 9%, decreasing to 0.5% for the shorter CA-functionalized nanocrystals.

Correcting the excitation spectra in Figure 5-3(a) for the absorption spectra shown in Figure 5-3(b) gives the relative photoluminescence quantum yield shown in Figure 5-3(c). It is evident that the intrinsic quantum yield of emission from PbS nanocrystals is largely independent of incident wavelength in our measurement range. The tetracene-coated samples, however, exhibit either dips or peaks in their blue-green spectrum depending on the ligand length. These features result from the competition between 'shadowing' – the absorption of photons in tetracene that would otherwise have been absorbed by the nanocrystals – and efficient energy transfer from tetracene to the PbS nanocrystals. The wavelength dependent quantum yield of photons from the nanocrystal can be expressed as:

$$QY(\lambda) = QY_{NC} \left(\frac{ABS_{NC}(\lambda) + \eta_{fis}\eta_{ET}ABS_{Tc}(\lambda)}{ABS_{NC}(\lambda) + ABS_{Tc}(\lambda)} \right) \tag{5.2}$$

where ABS_{NC} is the absorption of the nanocrystal, QY_{NC} is the intrinsic quantum yield of the nanocrystal, ABS_{Tc} is the absorption of tetracene, η_{fis} is the yield of excitons in tetracene after singlet exciton fission, and η_{ET} is the exciton transfer efficiency from tetracene to the nanocrystal.
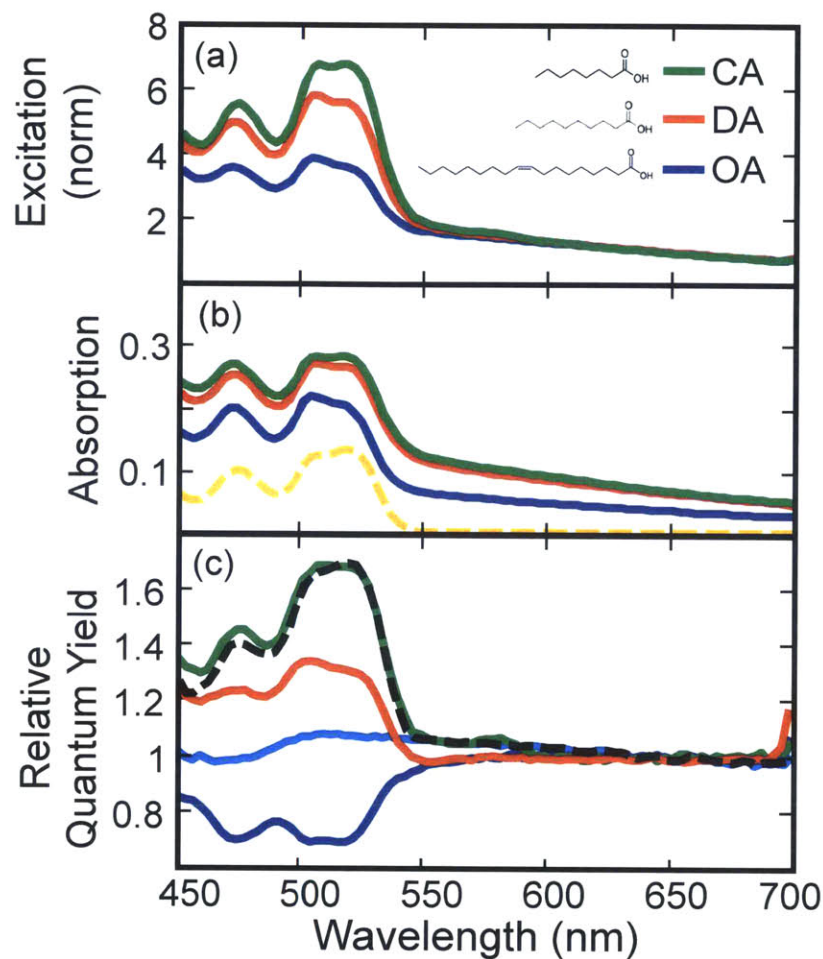
Figure 5-3. Steady state observations of triplet transfer. (a) Excitation spectrum for tetracene-capped films of 0.95 eV PbS nanocrystals with OA, DA, and CA ligands. Normalized by the mean value between 630 to 670 nm. Nanocrystal emission was measured for all wavelengths greater than 950 nm. (b) Visible absorption versus wavelength of each of the films in (a). Also plotted is the absorption of tetracene (orange dashes). (c) Relative photoluminescence quantum yield of each of the films in (a) and a neat film of nanocrystals (light blue) normalized by the mean value between 630 to 670 nm. The fit to the QY for the nanocrystals with a CA ligand is shown as a dashed black line. The tetracene layer is 20 nm thick. Ligand chemical structures are inset and are CA, DA, and OA from top to bottom.

5.5. PLQY Calculations

The absorption, reflection, and transmission of each layer are determined using an Aquila NKD-8000. The optical constants (n and k) are found using the method described in Section 4.2.4 from the measured reflection and transmission spectrum of each material. The photoluminescence quantum yield (PLQY) of each material is determined by a linear regression of the absorption of each material to the excitation curve. Optical effects on the absorption within each layer due to the differing dielectric constants of the nanocrystals and tetracene were taken into account using the transfer matrix method. The ratio of the PLQY for the tetracene and the nanocrystal layers gives the yield of excitons transferred to the nanocrystals per photon absorbed in tetracene. Because singlet exciton fission generates up to two triplet excitons for every absorbed photon, this value can range from 0–2. Accordingly, to obtain a lower bound the transfer efficiency (η_{ET}), we assume perfectly efficient fission ($\eta_{fis} = 2$).

Analysis of the photoluminescence quantum yield shows that the efficiency of energy transfer is notably improved when the nanocrystal ligand is short. In Figure 5-3(c) we find that nanocrystals treated with OA exhibit dips in the quantum yield for regions of strong tetracene absorption while CA-treated nanocrystals have peaks. Using the measured absorption spectra for neat films of tetracene and PbS nanocrystals we can determine the product $\eta_{fis}\eta_{ET}$ by fitting, as described above. An example fit is plotted in Figure 5-3(c), where $\eta_{fis}\eta_{ET} = 2.0$. Averaging thirteen different samples with caprylic acid ligands, we determine $\eta_{fis}\eta_{ET} = 1.80 \pm 0.26$.

The critical observation that $\eta_{fis}\eta_{ET} > 1$ provides definitive proof that the direct transfer of triplet excitons is the primary method of energy transfer in our device, because only the efficient transfer of triplets generated in pairs by fission could result in more excitons transferred to the

79

nanocrystals than photons absorbed in the tetracene. Specifically, assuming $\eta_{fis} = 2$, the lower bound for the efficiency of triplet transfer to CA-treated nanocrystals is $\eta_{ET} = 0.90 \pm 0.13$. Furthermore, as shown in Figure 5-4, we find that the transfer efficiency has an exponential dependence on the number of carbon-carbon bonds in the alkyl carboxylic acid ligand, which is consistent with Dexter transfer. The fit follows $\exp(-2\beta_n n)$ where $\beta_n = 0.098$ (C-C bonds)$^{-1}$ and n is the number of C-C bonds. Assuming a radial ligand morphology, this extracted value of β_n is nearly one order of magnitude greater than typically observed in charge transfer studies.[93] We note, however, that this measurement is a steady-state characterization of the yield of energy transfer, rather than a direct measurement of its rate. Indeed, the spatial dependence of the rate cannot be determined in the presence of competing channels that may also depend on the length of the nanocrystal ligands.
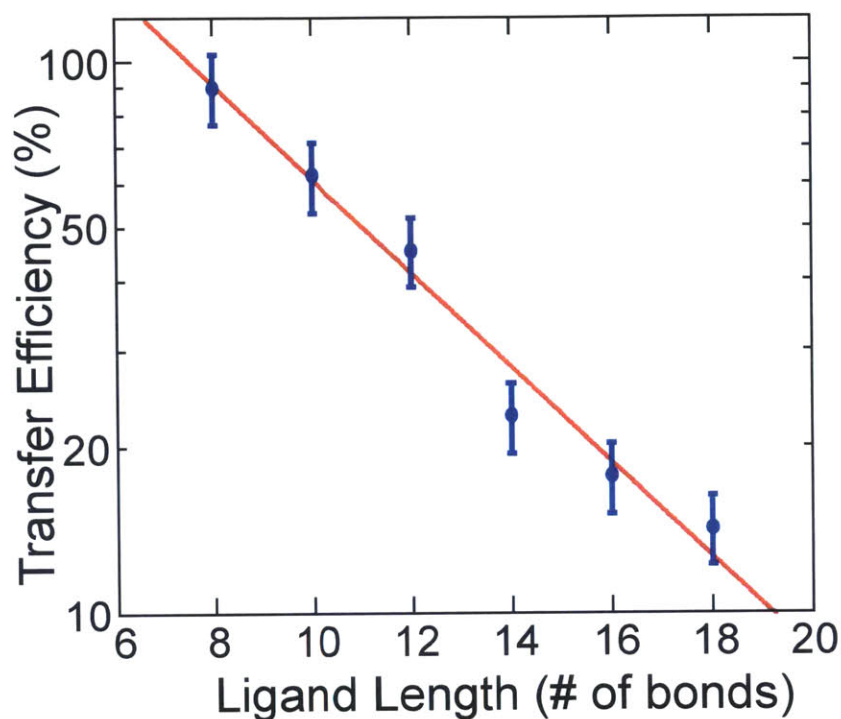
Figure 5-4. Energy transfer efficiency versus the number of carbon-carbon single bonds in the nanocrystal ligand. 0.95 eV PbS nanocrystals were used and we assumed a singlet fission efficiency of $\eta_{fis} = 2$. The solid line is an exponential fit.

5.6. Magnetic Field Effects

Triplet exciton transfer from tetracene to the PbS nanocrystals is confirmed and additionally distinguished from singlet exciton transfer via the steady state magnetic field dependence of singlet exciton fission.[86] A magnetic field $B > 0.4$ T slows the effective rate of triplet generation, shifting the balance from triplets towards singlets.[25,86,90] Magnetic field studies are especially useful in devices, since they can isolate the contribution of fission to the overall performance. In Figure 5-5 we plot the steady-state change in fluorescence from the tetracene coating and fluorescence from the tetracene coated nanocrystal film as a function of magnetic field. When exciting both tetracene and the PbS nanocrystals with continuous-wave light ($\lambda = 460$ nm),

we observe that the magnetic field dependence of each material is characteristic of singlet exciton fission, and closely matches previous photocurrent- and emission-based measurements.[51,53,54,86] Further, the dependences have opposite sign, which occurs because the inhibition of fission preserves singlets, leading to additional photoluminescence from the tetracene, while decreasing the reservoir of triplets, so that the nanocrystals emit less light. We emphasize that the field-dependence is due to singlet fission – as shown in Figure 5-5, the nanocrystal fluorescence is unaffected by the magnetic field when the bilayer film is excited at wavelengths where tetracene does not absorb. This is consistent with theoretical predications that a $B = 0.5$ T field is insufficient to significantly perturb the excitonic states of colloidal nanocrystals at room temperature.[94] We also observed no significant change in linewidth or position of the emission spectrum under a $B = 0.5$ T magnetic field.
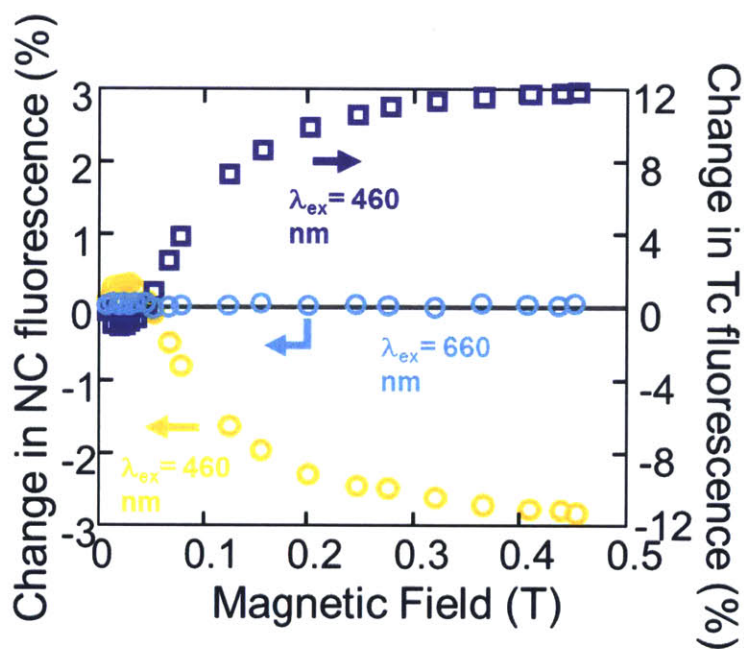
Figure 5-5. Change in emission from 0.95 eV ($\lambda = 1308$ nm) PbS-OA nanocrystal thin films coated with 40 nm of tetracene (circles) and fluorescence from the tetracene coating (squares) as a function of external magnetic field,
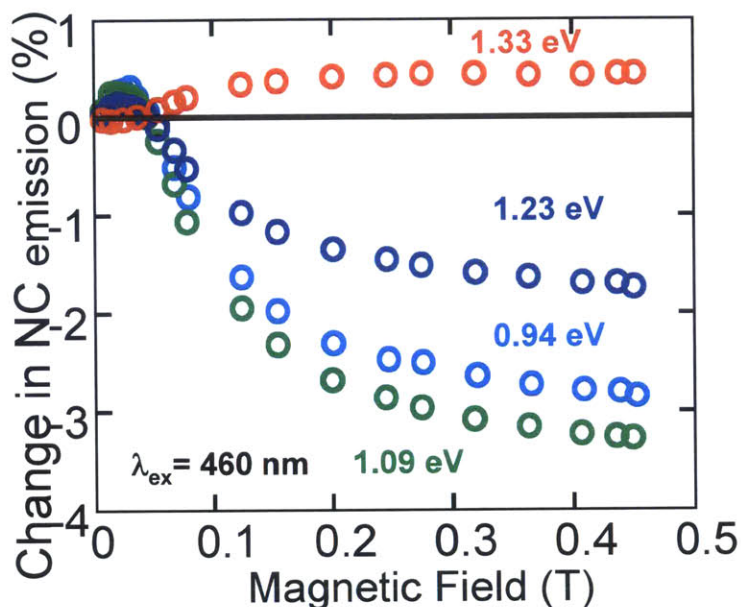
Figure 5-6. Change in PbS-OA nanocrystal thin film emission for various nanocrystal energies characterized by the energy of the first absorption peak in solution. Samples were coated with 40 nm of tetracene. The change in fluorescence is positive for nanocrystals films with energy greater than the triplet energy of tetracene. All data points indicate the energy of the first absorption peak. The bilayer films are excited with λ = 460 nm light.

The activation energy dependence of the triplet energy transfer process is shown in Figure 5-6. Dexter energy transfer favors acceptor materials with excited states equal or less in energy than the excited state in the donor. In PbS nanocrystals, this energy is strongly dependent on the size of the particles due to quantum confinement.[51,84,88,95] Thus, through the synthesis of different sized nanocrystals, we can examine the magnetic-field–dependence of fluorescence for nanocrystals with a range of exciton energies; see Figure 5-6. Nanocrystals with exciton energy greater than the tetracene triplet energy of 1.25 eV[42,51,88] exhibit a positive change in fluorescence

under large magnetic field, indicating energy transfer in these systems is primarily from singlet excitons. The 'threshold' transition to a negative magnetic field effect when nanocrystals' optical gap is less than 1.25 eV is difficult to reconcile with efficient singlet transfer, and instead indicates that singlet exciton fission and triplet exciton transfer overwhelms Förster transfer in this system when the transfer is exothermic.

5.7. Transient Measurements

Finally, the dynamics of triplet exciton transfer are obtained using transient near-infrared photoluminescence spectroscopy. In Figure 5-7 we observe that the photoluminescence decay of the nanocrystal layer is multi-exponential with a longest lifetime of nearly 1 μs. The intrinsic nanocrystal decay dynamics do not change significantly upon coating the nanocrystals with tetracene. However, when tetracene is optically excited, the resulting nanocrystal transient shows enhanced emission at all times following the initial excitation. In light of our previous findings, we presume this delayed emission to result from the influx of long-lived triplet excitons from tetracene.
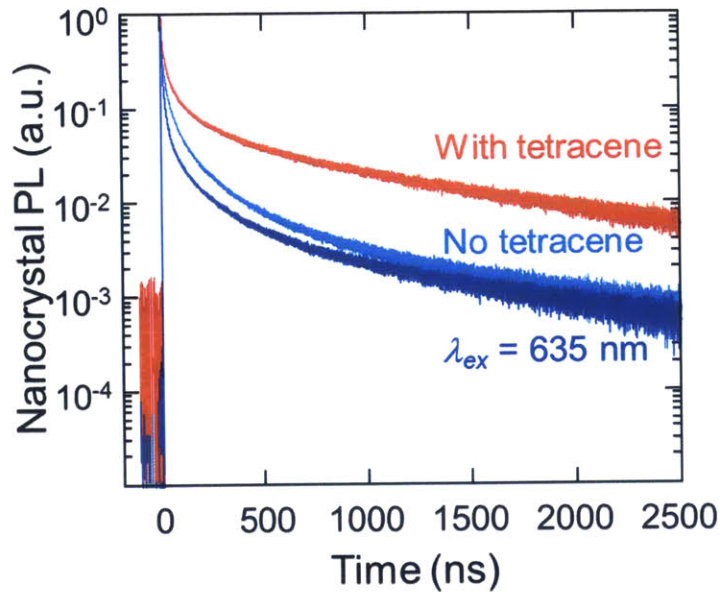
Figure 5-7. Near-infrared nanocrystal fluorescence as a function of time for tetracene-coated 0.95 eV (λ = 1308 nm) PbS-CA nanocrystals thin films pumped within the tetracene absorption band at λ = 532 nm (red), and beyond the tetracene absorption band at λ = 635 nm (dark blue). We also plot the transient response of the pure nanocrystal film with no tetracene coating to pulsed excitation at λ = 532 nm (light blue).

To obtain the time-dependent flux of excitons from the tetracene to the nanocrystal layer and distinguish between direct optical pumping of the nanocrystals and triplet transfer from tetracene, we deconvolve the photoluminescent impulse response of the nanocrystals from the total transient response. Fast Fourier Transforms are performed on the short wavelength infrared photoluminescence from both neat films of nanocrystals and tetracene coated nanocrystals. The resultant data is divided (equivalent to deconvolution in the time domain) to provide the frequency response of the exciton flux. The data is then converted back to the time domain via an inverse Fourier Transform. The time domain description of the exciton flux to the nanocrystals consists of a large initial impulse (representing the direct pumping of the nanocrystals with the laser) and a long tail (representing the flux of triplets from the tetracene). The impulse was removed by deleting

85

the first data point (corresponding to the first 64 ps) and the remaining signal due to the triplet flux was smoothed by a low pass filter and plotted in Figure 5-8. To obtain the time domain dynamics of the nanocrystal fluorescence that results from triplet energy transfer (orange curve of the inset in Figure 5-8), the unsmoothed triplet flux in the frequency domain was re-convolved with the nanocrystal impulse response function. This represents the photoluminescence due to the triplet current only. We note that our instrument response is approximately 300 ps, so further analysis is required to understand the short time dynamics.

The resulting exciton flux is plotted in Figure 5-8. It appears to be predominantly diffusion-limited but with a rapid initial component due to energy transfer from tetracene molecules immediately adjacent to the nanocrystals. In the inset of Figure 5-8, we show that the initial time constant of energy transfer to the nanocrystals is < 10 ns.
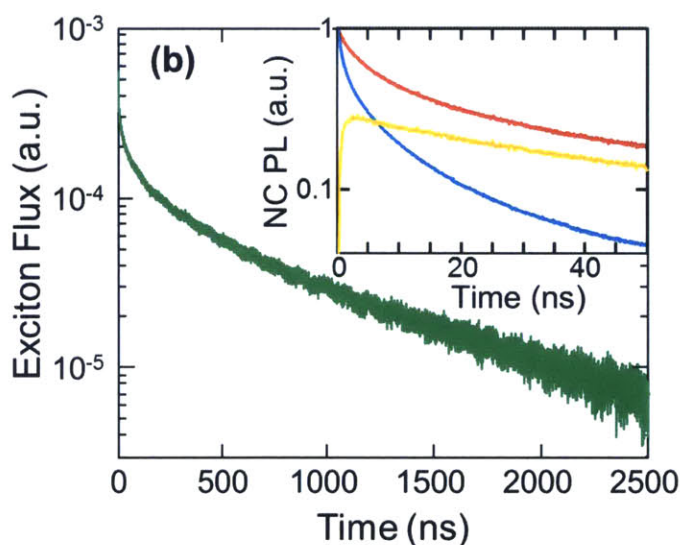
Figure 5-8. The exciton flux from tetracene to the nanocrystal film obtained by deconvolving the photoluminescence impulse response of the nanocrystals without tetracene from the tetracene-sensitized transient response. **Inset:** *The nanocrystal PL (NC PL) transient with direct optical pumping of the nanocrystals removed (orange), compared to the 'with tetracene' and 'no tetracene' transients from Figure 5-7. Emission stemming from transferred triplets dominates after 10 ns.*

Two independent control experiments were performed to gauge the 'intrinsic' decay kinetics of the nanocrystal PbS film and are featured in Figure 5-7. Firstly, as a shadow mask was used during tetracene deposition, the sample could be translated to probe a region where identically-prepared nanocrystals did not have a tetracene cap. These decay dynamics are labelled "No tetracene". Further, to address the possibility that the presence of the tetracene capping layer might induce interfacial states with altered decay kinetics, the excitation wavelength could be changed to 635 nm – a wavelength where the tetracene does not absorb – by replacing the usual excitation source with a PicoQuant P-C-635M. These kinetics are labeled "λ_{ex}=635 nm", and were taken using a pump irradiance of ~11 pJ/cm^2/pulse. As is clear from the figure, similar kinetics are recorded for either 'control' configuration, and both show significantly (>10x) reduced emission at all times more than 100 ns after photoexcitation compared to the neat film of nanocrystals. This is consistent with our hypothesis that the enhanced 'delayed' nanocrystal emission results from the transfer of additional energy from long-lived triplet excitons generated in the tetracene cap.

As shown in Figure 5-9(a), measurements of the visible transient fluorescence from tetracene do not conclusively demonstrate triplet exciton energy transfer. Indeed, the fluorescence (>1 ns) of tetracene is not noticeably quenched when deposited on top of a layer of nanocrystals that show evidence of energy transfer in steady state. For comparison, some quenching of the photoluminescence was observed when a neat layer of tetracene was capped with C$_{60}$.
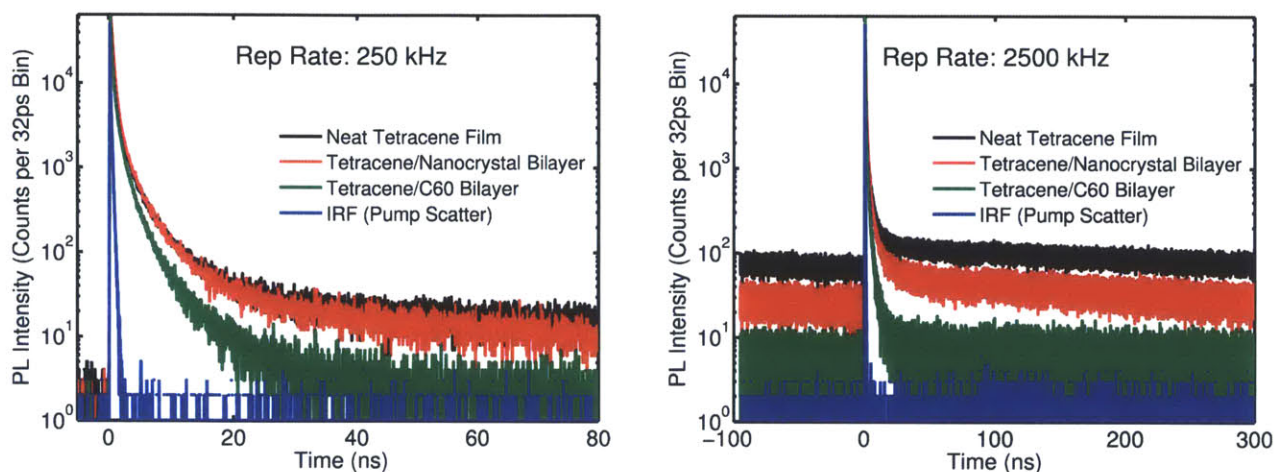
Figure 5-9. Measurements of tetracene fluorescence as a function of pump pulse repetition rate: (left) 250 kHz, and (right) 2.5 MHz. Three samples are compared: a 40-nm-thick layer of neat tetracene, a 40-nm-thick layer of tetracene deposited on a PbS film, and a 40-nm-thick layer of tetracene deposited on the fullerene C60. There is little evidence for instantaneous quenching of the tetracene fluorescence by PbS nanocrystals, even though these same films show efficient triplet transfer. As shown in the right figure, we do observe the expected quenching in the quasi-static background when we create a much-larger pool of non-geminate triplets by increasing the repetition rate of the laser. We associate this with the transfer of 'free' triplets to PbS prior to their fusion back into singlet excitons.

To understand this result, it is important to recall that the vast majority of singlet excitons decay via fission to produce triplet pairs, as this process (τ~100 ps)[43,44] kinetically out-competes radiative emission by more than an order of magnitude.[43,96] Thus, the overwhelming majority of the emission observed after 1 ns results from singlet excitons regenerated from triplet-triplet interactions. Many of these interactions are 'geminate' – occurring between two spin-correlated triplets that arose from the same 'parent' singlet.[37] This is particularly the case at the low excitation densities employed here, where non-geminate bimolecular encounters are unlikely.

With this foreknowledge, the lack of fluorescence quenching when tetracene is in contact with the nanocrystals has two implications. First, that the direct quenching of singlets by the nanocrystals (via energy transfer following diffusion) must be negligible compared to their intrinsic decay channels (*i.e.* exciton fission). This is unsurprising given the rapidity of exciton

fission – the rather modest effect of the conventional electron acceptor C_{60} has a similar origin. Secondly, in the low-flux limit, these data make clear that the transfer of triplet excitons (as confirmed by our other techniques) does not significantly affect the amount of 'delayed' fluorescence, which is consistent with our understanding that non-geminate bimolecular events are rare under these conditions.

Interestingly, at higher laser repetition rates, triplet exciton transfer is suggested by the reduced quasi-steady-state 'background.' This 'background' arises from the increased delayed fluorescence from non-geminate interactions between the much-larger quasi-steady-state population of long-lived triplets[97] that rapidly build up in the film under more frequent illumination. As shown Figure 5-9(b), we observe a notable decrease in the 'background' fluorescence from a tetracene-nanocrystal bilayer relative to the tetracene alone. This result is consistent with the loss of photoexcitations to the nanocrystals, and occurs on a timescale where free triplets form the majority of the remaining excited states.

5.8. Photovoltaic Devices

Inverted photovoltaic devices were constructed to verify the energy level-based prediction that the tetracene/PbS interface does not dissociate excitons. The energy level diagram is shown in Figure 5-10(a). Two layers of nanocrystals were spun on the ITO and ligand exchanged to caprylic acid. These layers were followed by 20 nm of tetracene, 8 nm of m-MTDATA as an exciton blocking layer,[54] and 5 nm MoO_3 to improve contact to the gold cathode (80 nm). The external quantum efficiency of these devices is plotted in Figure 5-10(b). The overall EQE is low, due to the low conductivity of the nanocrystals and poor hole extraction of the device. However,

the absorption peaks of tetracene are clearly visible. This indicates that photons absorbed in the tetracene generate photocurrent. However, UPS results indicate that the HOMO level of the nanocrystals is ill-suited for charge transfer state formation, as charge formation is endothermic by 0.15 eV. Thus, this photocurrent must be via triplet transfer to the nanocrystals followed by field dissociation of the exciton in the nanocrystal layer.
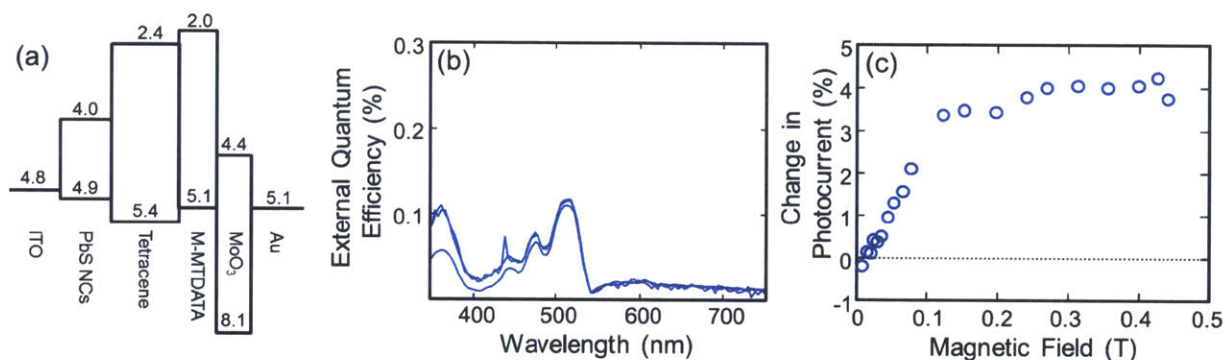
Figure 5-10. (a) Energy level diagram of a tetracene/PbS photovoltaic device. Levels are from Ref. [54,56] (b) External quantum efficiency of the devices from part (a). Note the peaks of tetracene absorption. (c) Magnetic field effect on photocurrent of the constructed device. Note the strong, monotonic, positive change in photocurrent at small magnetic fields, followed by saturation at larger ones, consistent with triplet-charge annihilation.

Further evidence of the lack of any charge transfer state formation is derived from the comparison of the magnetic field effect on fluorescence or photocurrent with and without the presence of electrical contacts. As shown in Figure 5-10(c), triplet-charge annihilation[57] (characterized in the magnetic field effect by a rapid increase in the photocurrent at low magnetic fields followed by rapid saturation) is readily apparent when the contacts are present, but no triplet-charge annihilation is found in any of the bilayer optical structures (see Figure 5-5), indicating a lack of free charge in those films. It is expected that charge is formed within the nanocrystal layer

90

in the presence of an electric field, which is created in the electrical device at the ITO/PbS Schottky contact and by the alignment of the anode and cathode under short circuit conditions.

Thus, we have shown that the transfer of triplets from tetracene to a colloidal nanocrystal is both efficient and rapid, and will be a key component of future attempts to couple the gain from singlet fission to a silicon solar cell.

Chapter 6: Triplet-triplet Annihilation Upconversion

6.1. Introduction

Upconversion would allow for efficient harvesting of the infrared portion of the spectrum, increasing the efficiency for all types of solar cells. Here, we detail our efforts to develop an efficient, low power upconversion process. We detail the absorption and emission of the device, demonstrating unequivocally that the upconversion proceeds through the nanocrystals and can be utilized from 1100 nm, the deepest TTA upconversion so far demonstrated.

6.2. Upconversion Background

Optical upconversion is a process that converts two or more low-energy photons into a single high-energy photon. It has many applications, including biological imaging[98], pathogen detection[99], optical data storage[100], night vision[101], 2D[102] and 3D[103] displays, and photovoltaics[104]. In photovoltaic applications specifically, an optical upconversion layer can capture sub-bandgap photons, increasing the efficiency of a conventional single junction device beyond the Shockley-Queisser limit[7,105].

There are two general approaches to optical upconversion. For high intensity, coherent light, it is possible to directly generate higher harmonics by exploiting the nonlinearity susceptibility of many materials[106]. The process can be very efficient when properly phase-matched, and it is widely employed—for example, in frequency-doubled lasers[107]. However, it is poorly suited to the conversion of broadband, incoherent sunlight[108].

To upconvert incoherent light at relatively low intensities, it is generally necessary to first store the input energy in the form of a long-lived atomic or molecular excited state. Then a higher

energy state can be reached through energy transfer or subsequent absorption. For upconversion of infrared photons, lanthanide ions in inorganic hosts have been a popular choice[109]. However, absorption in lanthanides is weak and narrow, necessitating relatively high incident power. The most efficient system to date is $NaYF_4$: Er^{3+}, Yb^{3+}, converting $\lambda = 980$ nm to 540 nm light at 80 W cm^{-2} with an internal quantum efficiency of 23%[110].

Sensitized triplet-triplet annihilation (TTA) is a promising alternative approach at lower excitation intensities[111–114]. But since molecular triplet excitons are typically dark and inefficiently created by direct optical excitation, the process requires a sensitizer to generate triplets. The sensitizer, typically an organometallic complex[115], absorbs incident light, forming an excited singlet state, which is then converted to a triplet state through intersystem crossing. Energy is transferred from the excited triplet state of the sensitizer to a triplet state of the annihilator. The annihilator, which is commonly an oligoacene derivative[115], has large singlet-triplet splitting. When two annihilator molecules in the triplet state meet, they undergo TTA to form a single spin-singlet exciton, leading to blue-shifted emission. Despite feasibility at subsolar irradiance[116] and internal quantum efficiencies as high as 32% for green-to-blue conversion[117,118], demonstrations of NIR-to-visible upconversion have been limited to incident wavelengths shorter than $\lambda = 790$ nm[119], precluding their application to a variety of solar cells, including crystalline silicon. This is because nonradiative losses in the sensitizer increase with decreasing energy gap[120], limiting the number of effective sensitizers in the near infrared. There is also typically an energy loss of hundreds of meV during the sensitization process due to the exchange splitting between sensitizer singlet and triplet states[114]. Finally, most demonstrations to date have been in solution, which is not ideal for practical applications. Solid-state alternatives with active species dispersed in gel-like polymers tend to have lower efficiency as slower diffusion impedes energy transfer[121].

6.3. Colloidal Nanocrystals as Sensitizer

To address these problems, we replace the molecular sensitizers with inorganic colloidal nanocrystals (NCs). The bandgap of NCs is highly tunable, allowing broadband absorption deep into the NIR[95]. Splitting between the singlet and triplet states in these materials is also negligible[122], minimizing energy loss during sensitization. Finally, we adopt a device structure of solid-state thin films, ensuring a high concentration of active species and short diffusion path lengths for optimal energy transfer. Indeed, it has recently been shown that triplets generated by singlet exciton fission in thin tetracene films can energy transfer efficiently to PbS NCs[80,123]. Here, we demonstrate the reverse process of energy transfer from PbS NCs to the triplet states of the organic material rubrene, achieving sensitization of upconversion from beyond $\lambda = 1$ μm in a solid-state geometry.

Ø4.8nm   Transfer   TTA
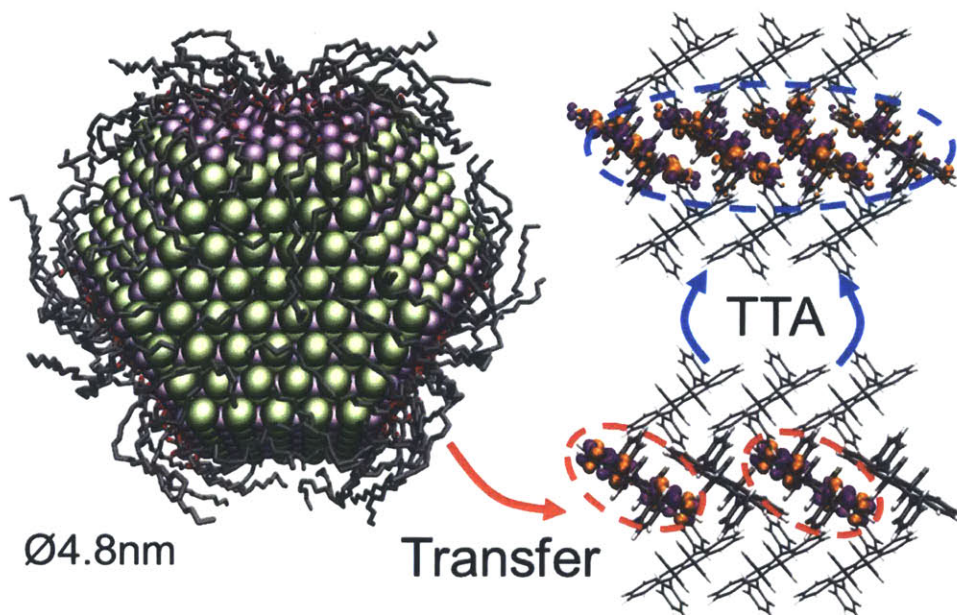
Figure 6-1. The upconversion process. The colloidal nanocrystal sensitizer absorbs light and generates triplet states, which can the Dexter transfer to the rubrene annihilator. When two triplets meet, they perform triplet-triplet

annihilation, generating a singlet state which can then fluoresce with twice the energy of the incident light. The ligands on the nanocrystal are simulated oleic acid.

To build these devices, a thin layer of NCs is first spun on glass as the sensitizer. Rubrene is utilized as the annihilator. We found that adding .5% by volume of 5,10,15,20-Tetraphenylbisbenz[5,6]indeno[1,2,3-cd:1',2',3'-lm]perylene (DBP) increases the fluorescence intensity by a factor of 30 from the device. Doping rubrene with DBP is commonly employed in OLEDs to increase the emissivity in solid state.[124] All annihilator films are 80 nm thick. All devices are fabricated in a glovebox and encapsulated before testing in the air.

The upconversion process is illustrated in Figure 6-1. The colloidal nanocrystal, shown here with oleic acid ligands, absorbs light and generates triplet states. These transfer to the rubrene annihilator via Dexter transfer. When two triplets meet, they perform triplet-triplet annihilation, generating a single singlet state, which can then FRET to the DBP emitter molecule, which emits light with high efficiency. The energy levels of this process are drawn in Figure 6-2.
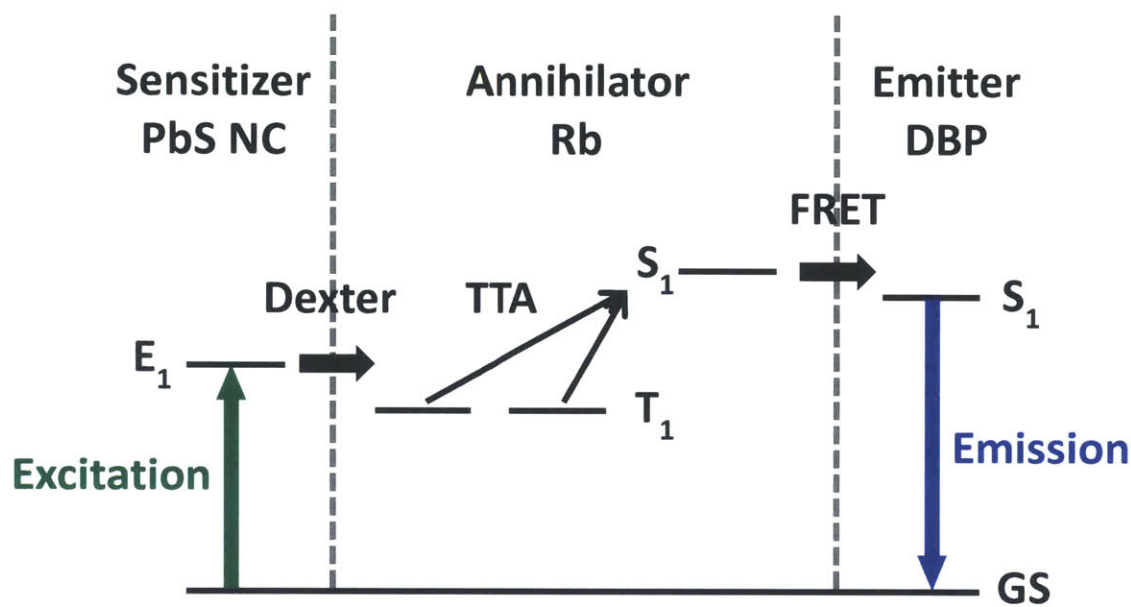
Figure 6-2. Energy level diagram of the upconversion process. Low energy light excites the nanocrystal, which Dexter transfers to the rubrene triplet. This performs triplet-triplet annihilation to the singlet state, which then FRETs to the DBP emitter molecule.

We fabricate devices with three sizes of PbS NCs. Their first absorption peaks are at 834 nm, 947 nm, and 1011 nm, respectively, as shown in Figure 6-3. We utilize thin layers of nanocrystals to maximize the transfer efficiency; in practice this results in sub-monolayer coverage, see Figure 6-4. Rubrene was chosen as the annihilator as its first excited triplet state is at 1.14 eV[125], well-positioned for NIR sensitization. Furthermore, its high-lying second excited triplet state is reported to allow a TTA yield that exceeds the statistical limit of 40% assuming a 1:3 ratio of singlets to triplets and the recycling of high energy triplets formed by TTA[126,127].

To demonstrate triplet transfer, we excite the samples with a 100 mW 808 nm CW laser and monitor the output from the rubrene:DBP annihilator. Clear emission from DBP is observed, as shown in Figure 6-3 (black line) and Figure 6-6. Control films without the NCs have no visible

emission under the same conditions, proving the transfer of triplets from the NCs to the rubrene. In all cases, singlet transfer from the NCs to the rubrene is energetically forbidden.
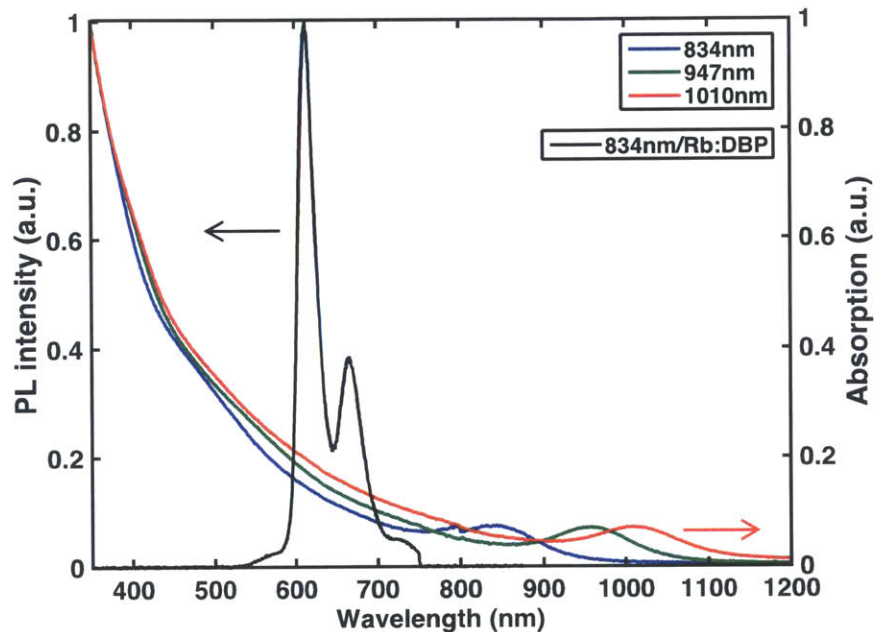
Figure 6-3. Absorption of the colloidal nanocrystals (red, blue, green) and emission from the DBP (black). This demonstrates the clear upconversion advantage, as light absorbed at 1000 nm can be converted to light at 600 nm.
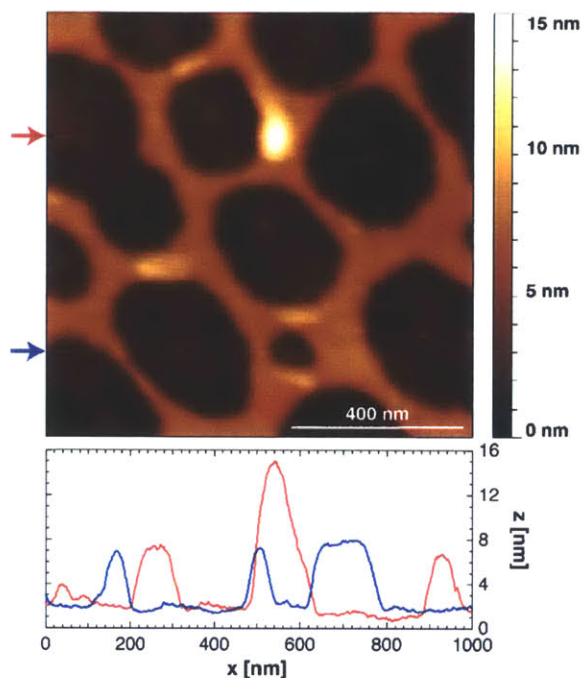
Figure 6-4. AFM of the thin nanocrystal layer. Incomplete coverage of the glass slide is observed.

6.4. DBP as emitter

The addition of DBP allows for a strong increase in PLQY. Because rubrene is a fission material, getting the singlet out of the system before it fissions back to two triplets is of utmost importance. The inclusion of the DBP allows for the singlet to transfer to that molecule, where it has too little energy to fission. Thus, it fluoresces with high efficiency. The gains of this process are demonstrated in Figure 6-5. The addition of DBP redshifts the emission by approximately 40 nm, but increases the brightness by a factor of 30 due to minimizing loss by singlet fission.
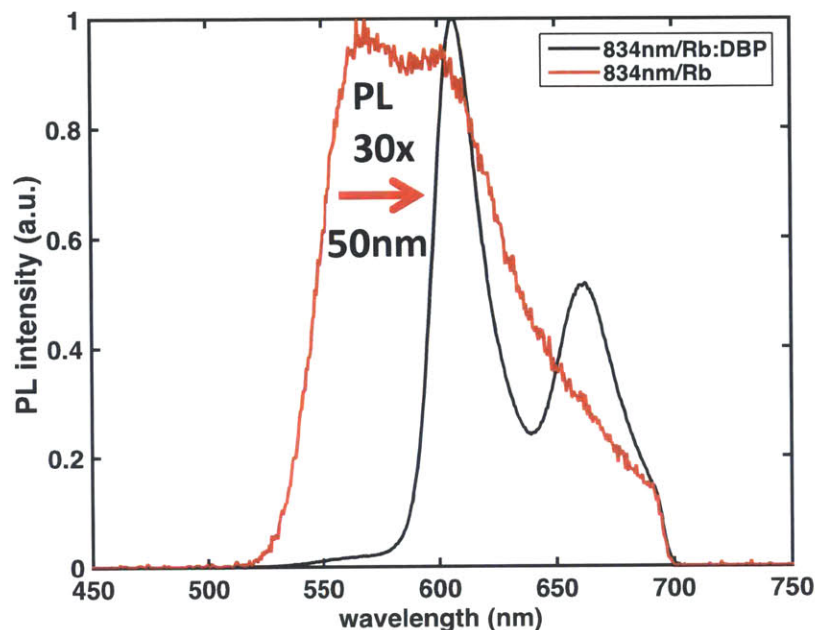
Figure 6-5. The gains of DBP doping. The sacrifice of 40 nm of photoluminescence allows for a 30x increase in brightness.

6.5. Yield

To determine the upconversion quantum efficiency, η_{UC}, defined as the combined efficiencies of triplet generation, transfer, and annihilation, we measure the PL quantum yield (PLQY) of the film in an integrating sphere[128]. By convention, the quantum efficiency is normalized to 100% if two photons give rise to one higher energy photon[115].

We find that the highest quantum efficiency is attained when the NCs are sub-monolayer, due to minimized re-absorption by the NCs and a shorter diffusion path length to reach the bilayer interface. The weak NIR absorption of the sub-monolayer film makes direct measurement of the optical density challenging. Instead, we waveguide pump the sample in an integrating sphere and

measure the PLQY excited at 808nm. The upconversion efficiency is determined by normalizing this to the PLQY of the organic on the same sample excited at 460 nm.

Upconversion efficiency for the three sizes of PbS NCs, excited at 808 nm, are η_{UC} (850 nm) = 1.23%, η_{UC} (960 nm) = 0.51%, η_{UC} (1010 nm) = 0.21%. Upconversion efficiency is the product of the efficiencies of triplet energy transfer and TTA. Since the annihilator is kept constant for varying NC sizes, the decrease in η_{UC} as the energy of the NCs is reduced indicates that the number of triplets transferring decreases as the initial state energy approaches that of rubrene. This could be due to less efficient energy transfer or an increase in non-radiative pathways in the NCs at lower energies.

6.6. Intensity dependence

In TTA-based upconversion, an important figure of merit is the threshold excitation intensity at which the dependence of emission on incident light intensity transitions from quadratic to linear[116,129]. Below the threshold, the triplet population varies linearly with excitation power because the triplet lifetime is controlled by a first-order loss process such as non-radiative decay or quenching by ground state oxygen[127]. TTA, which is bimolecular, is therefore quadratic with pump intensity. However, when the triplet density is sufficiently high, TTA becomes the dominant decay process. With TTA controlling the lifetime of the triplet species, the triplet density varies as the square root of pump intensity. Thus, the TTA process becomes linear with pump power, and the transition corresponds to the excitation intensity required to reach maximum efficiency[116,129]. Figure 6-7 shows that for the NC-sensitized thin-film samples, the transition occurs close to 10 W cm^{-2} for λ = 850 nm and 960 nm NCs. Given the slight absorption by the sub-monolayer NC film,

we note that this is equivalent to absorbed power density of 10 mW cm^{-2}. Similar thresholds are observed for TTA in electrically-pumped organic LEDs, confirming that triplet exciton confinement in solid-state films can substantially lower the necessary excitation power required for efficient TTA[124].
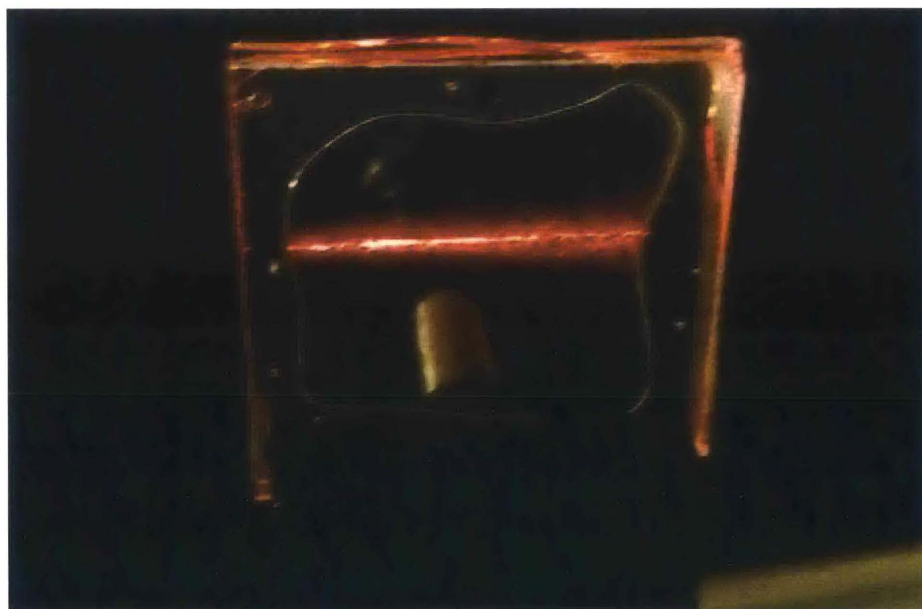
Figure 6-6. Upconverted light. 808 nm CW light is incident on the Rb:DBP:834 nm nanocrystal sample, giving off red upconverted light.
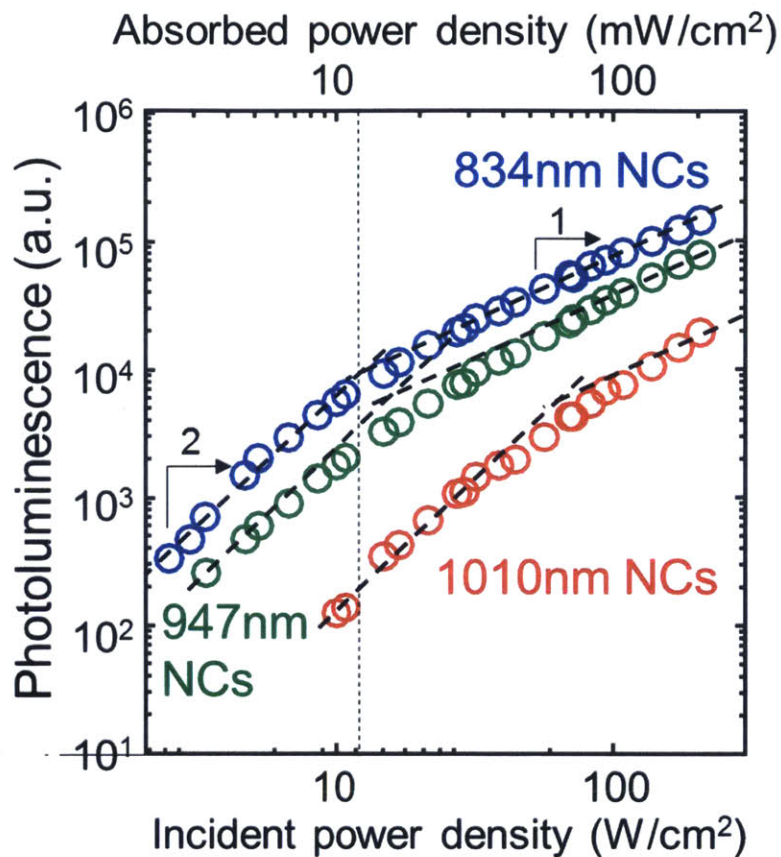
Figure 6-7. Intensity dependence of the upconversion devices. The absorbed power density is for the 834 nm nanocrystals, demonstrating a threshold of less than one sun.

6.7. Excitation Spectra

To show that PbS NCs sensitize over a broad wavelength range and extend beyond 1 micron, we measure the visible emission from the rubrene:DBP annihilator sensitized by 1011nm NCs while sweeping the excitation wavelengths. The excitation spectrum in Figure 6-8 agrees well with the absorption profile of the NCs in solution. Given that the rubrene triplet energy is about 1.14 eV, this demonstrates that sensitization by NCs requires minimal energy offset. By reducing the energetic loss in the sensitizer, we are able to capture a greater portion of the initial photonic

energy, allowing for a much larger energetic difference between absorption and emission. This allows us to demonstrate upconversion from past 1 micron for the first time. In fact, the energetic difference between absorption and emission is the highest measured for rubrene.[115,129]
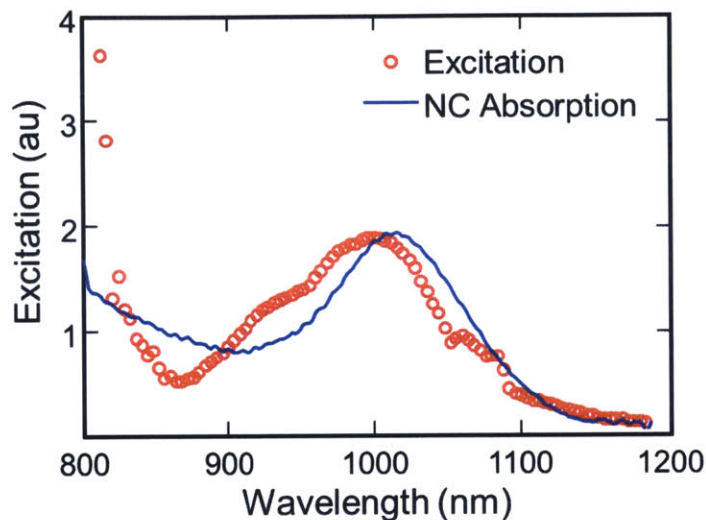
Figure 6-8. The excitation spectra for a bilayer of 1010 nm NCs and rubrene:DBP (red). The spectra neatly traces the absorption of the 1010 nm NCs in solution (blue), unequivocally demonstrating that the upconversion process proceeds through the NCs. Upconversion proceeds from 1100 nm.

6.8. Magnetic Field Effect

Finally, like singlet fission, the triplet-triplet annihilation process should demonstrate a magnetic field effect. A 947 nm nanocrystal sample with Rb:DBP was excited at 808 nm, and the rubrene fluorescence monitored. The negative delta shown in Figure 6-9 is consistent with previous reports of TTA magnetic field effect.[26]
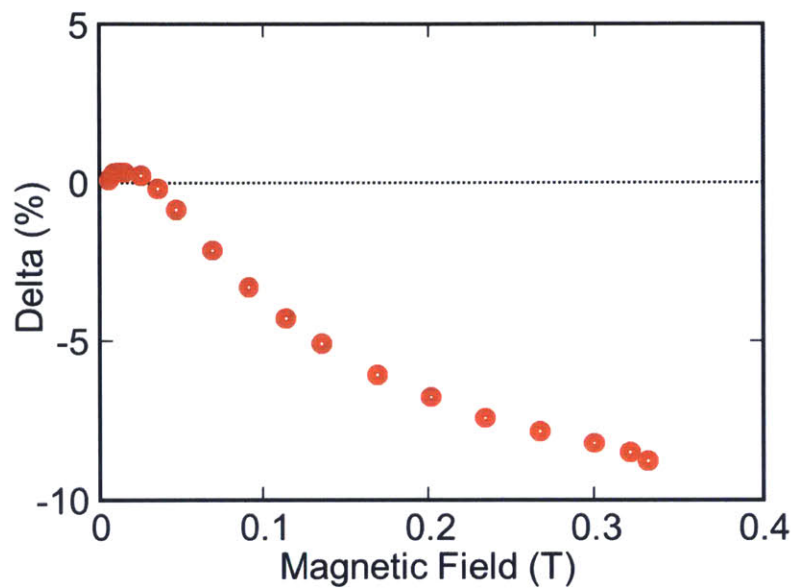
Figure 6-9. Magnetic field effect of upconversion. 947 nm nanocrystal:Rb:DBP device was excited at 808 nm and the rubrene fluorescence measured as described above.

6.9. Transient Measurements

To reveal the underlying physical processes and identify further device optimization pathways, we measure the PL dynamics of our hybrid films. In all cases, films were excited at $\lambda = 785$nm—well below the optical gaps of rubrene or DBP—so that the pump pulse was exclusively absorbed by the NCs. A shadow mask was used during organic deposition so that, on the same sample, we can optically access both bilayer regions as well as areas that had the sub-monolayer NC film alone. Monitoring the infrared PL dynamics of the $\lambda = 960$nm NCs alone (Figure 6-10), we observe that the decay is slow—multi-exponential at early times giving way to a monoexponential decay with $\tau = 2.4\mu$s. This is consistent with the isolated-NC dynamics measured in solution plus some additional early-time quenching, likely via transfer to neighboring NCs that are either permanently non-emissive or transiently 'blinked'[130,131].

By contrast, the addition of the organic layer adds new decay pathways, clearly accelerating the PL decay at early times. Noting that the dynamics from all bilayers evolve to match those measured for the NC-only regions after 3 μs, we assert a simple model where there are two sub-populations of NCs: those which are able to transfer excitations to the organic, and those which are not. In addition to kinetic competition, this could arise from morphological heterogeneity which may leave some NCs distant from a hetero-interface. Under this model, the fraction of NCs participating in transfer is given by the ratio of the late-time decay amplitudes when the data is normalized to the peak. We observe that this fraction varies between films and is 63% for the sample in Figure 6-10. Subtraction of this 'non-interacting' decay component from the dynamics of the bilayer allows us to isolate the dynamics of NCs affected by the presence of rubrene. We observe that the transfer dynamics are slow, with decay components from 300–500ns. This is consistent with our previous work on the reverse process—triplet transfer from organic materials to NCs—with these very long oleic acid ligands[80]. However, given the very slow decay dynamics of PbS NCs, even these transfer rates kinetically outcompete other processes so that transfer is reasonably efficient (>80%) from participating NCs. Instead, these measurements highlight a promising near-term target for optimization: a two-fold increase in performance could be obtained if the film morphology allowed all excitations to be harvested.
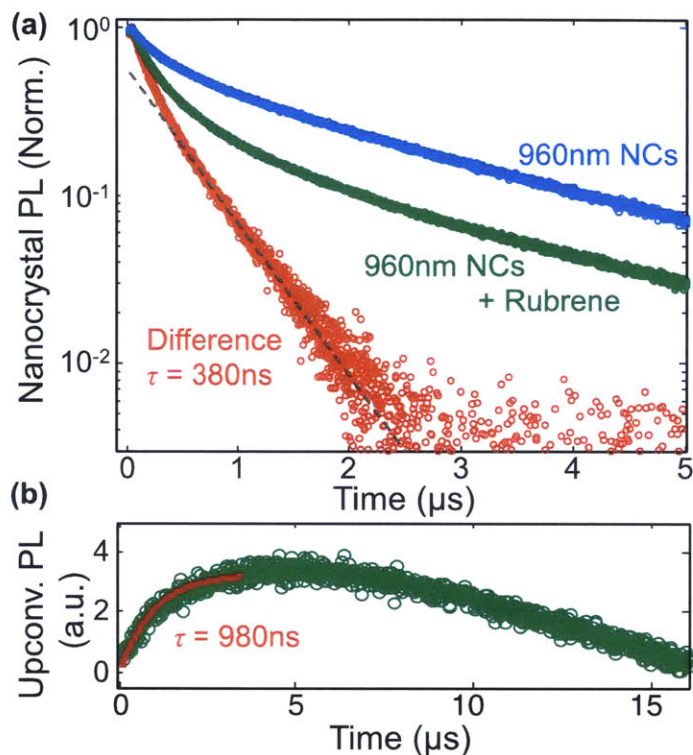
Figure 6-10. (a) Quenching of the infrared emission from PbS NCs in the presence of rubrene with 0.5% DBP. The extracted dynamics of triplet transfer (red) are largely monoexponential. (b) The corresponding rising dynamics of visible emission from the DBP show a characteristic time constant of 980ns, comprised of triplet transfer to rubrene, diffusion-mediated TTA, and energy transfer to the DBP. The slow subsequent decay reflects the very long lifetime of isolated triplets in rubrene—so long that a fraction of photoexcitations survives until the subsequent excitation pulse 16μs later.

Lastly, to confirm that the quenching process is indeed energy transfer resulting in visible emission, we measure the rising dynamics of the PL from the DBP in the bilayer regions on the same film of λ = 960nm NCs. We observe that all dynamics are slow, with the PL rising on a 980ns timescale. This primarily reflects the additional time required for TTA to occur via diffusion. The emission then decays much more slowly (~5μs), reflecting the very long lifetimes of isolated triplets in oligoacenes[132]. Although this explains why we are able to achieve efficient upconversion at low excitation densities, an associated consequence is that excitations in the organic, likely

trapped triplet excitons[97], survive until the next excitation pulse, building up a quasi-steady-state population of triplets. As a result, we vary the repetition rate and observe that the rise-time of the visible emission depends on the quasi-steady-state excitation, accelerating at higher densities to approach the transfer rate extracted from the quenching measurements.

In conclusion, we demonstrate sensitization of TTA-based upconversion by PbS colloidal NCs, reducing exchange splitting losses in the conversion of singlets to triplets, and enabling efficient solid-state upconversion from $\lambda > 1$ µm to the visible. Given the bandgap tunability of NCs, this approach can be extended further into the NIR with molecular annihilators that have lower triplet energies than rubrene, allowing for facile collection of the NIR for photovoltaic devices and the efficient use of optical upconversion in other applications such as night vision and 3D displays.

Chapter 7: Spin Dependent Charge Transfer State Design

7.1. Introduction

Charge transfer states play a crucial role in organic photovoltaics, mediating both photocurrent generation and recombination losses. In this section, we examine recombination losses as a function of the electron-hole spacing in fluorescent charge transfer states, including direct monitoring of both singlet and triplet charge transfer state dynamics. We demonstrate that large donor-acceptor separations minimize back transfer from the charge transfer state to a low-lying triplet exciton 'drain' or the ground state by utilizing external pressure to modulate molecular spacing. The triplet drain quenches triplet charge transfer states that would otherwise be spin-protected against recombination, and switches the most efficient origin of the photocurrent from triplet to singlet CT states. This work is adapted from reference [133] and a paper currently under review.

7.2. Materials and Methods

7.2.1. Sample Fabrication

To characterize CT state dynamics of m-MTDATA:3TPYMB and m-MTDATA:t-Bu-PBD we deposited thin films for pressure testing and made OPV devices to obtain the magnetic field dependence of photocurrent. OPV devices consisted of 60 nm of a 1:1 molar donor-acceptor blend thermally evaporated on 15 ohms per square ITO and capped with 100 nm of Aluminum. All organic materials were purchased from Lumtec (Luminescence Technology Corp.) and used as received. The blended heterojunction films for pressure testing consisted of 60 nm of a 1:1 molar blend thermally evaporated on thick glass samples with 100 nm of Aluminum deposited on top of

the blend for consistency in reflection under pressure. The samples were then encapsulated with thin flexible glass covers and epoxy.

7.2.2. Pressure Measurements

Pressure was applied using a motorized micrometer system with known force through a probe. The applied force distorts the substrate, and we estimated the contact area (radius ~100 μm) to obtain the applied pressure on the film through the top flexible cover glass. Optical characterization was performed through the substrate using a microscope setup with a λ = 405 nm pulsed 31.25 kHz excitation laser (PicoQuant LDH) focused to ~10 μm spot size. A 405 nm dichroic and a 450 nm long-pass filter was used to filter CT state emissions. A spectrometer (Princeton Instrument Acton) was used to take steady state PL measurements. Time-resolved PL measurements were taken using an avalanche photodiode single-photon detector (Picoquant PDM).

7.2.3. Magnetic Field Dependence

Magnetic field measurements were made as described previously in Section 4.2.5.

7.2.4. T-Bu-PBD Triplet Energy

We were unable to obtain clean phosphorescent spectra for t-Bu-PBD at low temperature. Previous measurements of the low temperature phosphorescence of t-Bu-PBD derivatives estimate that the t-Bu-PBD triplet is 2.54eV.[134] We test this estimation by comparing the triplet energy of t-Bu-PBD to the phosphor FIrpic, which has a triplet energy of 2.65 eV.[135] FIrpic was doped at 5%

weight into both N,N'-dicarbazolyl-3,5-benzene (MCP) and t-Bu-PBD; see Figure 7-1. The MCP-doped film phosphoresces brightly (green line) while the t-Bu-PBD doped film (purple line) is less than 2% as bright. Charge transfer state formation is not energetically favorable.[136,137] This demonstrates the triplet energy of t-Bu-PBD is less than that of FIrpic, which is traditionally accepted to be approximately 2.65 eV. We conclude that t-Bu-PBD acts as a triplet exciton acceptor for triplet m-MTDATA:t-Bu-PBD exciplexes.
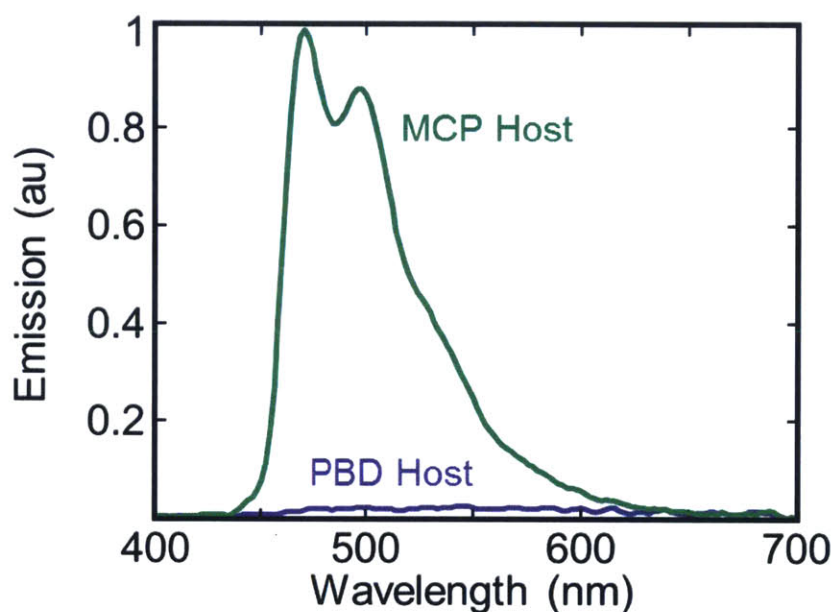
Figure 7-1. t-Bu-PBD host significantly quenches the triplet emission from FIrpic, demonstrating a lower energy triplet state in t-Bu-PBD.

7.3. Charge Transfer (CT) States

Charge transfer (CT) states are bound combinations of an electron and a hole located on separate molecules.[138–140] They are formed on neighboring molecules at donor-acceptor interfaces in organic photovoltaics (OPVs) after dissociation of excitons or during recombination of free

charge.[141–143] Modern OPVs demonstrate ultrafast formation of CT states from excitons, and efficient dissociation of CT states into charge under short circuit conditions.[144] Indeed, internal quantum efficiencies of many OPVs now commonly approach 100%.[19] But charge recombination losses mediated by CT states remain a problem in even the best devices,[145–148] increasing dramatically at weaker internal electric fields, reducing open circuit voltage and power efficiency.

Synthetic control over donor and acceptor OPV materials enables us to engineer the physical separation of the electron and hole at the donor-acceptor interface. This prompts an important question in OPV: *What's the effect of the CT state size?* On one hand, separated CT states have smaller Coulombic binding energies, which should improve the photocurrent yield. But large separations are also expected to possess weaker coupling to the initial exciton, potentially reducing the exciton dissociation rate at donor-acceptor interfaces.[149] In addition, increased charge separation significantly reduces exchange splitting between singlet and triplet CT states. When the two are nearly degenerate, intersystem crossing between the two is fast, facilitating spin engineering that could improve the efficiency of OPVs. For example, spin 1 triplet CT states are forbidden from recombining to the ground state, which is typically a spin 0 singlet. Traditional OPV designs demand, however, that the CT state energy be as high as possible in order to maximize the open circuit voltage.[150,151] Typically, this pushes the CT energy above the energy of the triplet exciton on the donor or acceptor. As the lowest energy excited state in the system, the triplet exciton traps the energy originally contained in the CT state until it eventually recombines to the ground state, creating a crucial loss pathway, or 'triplet drain'.[140,146]
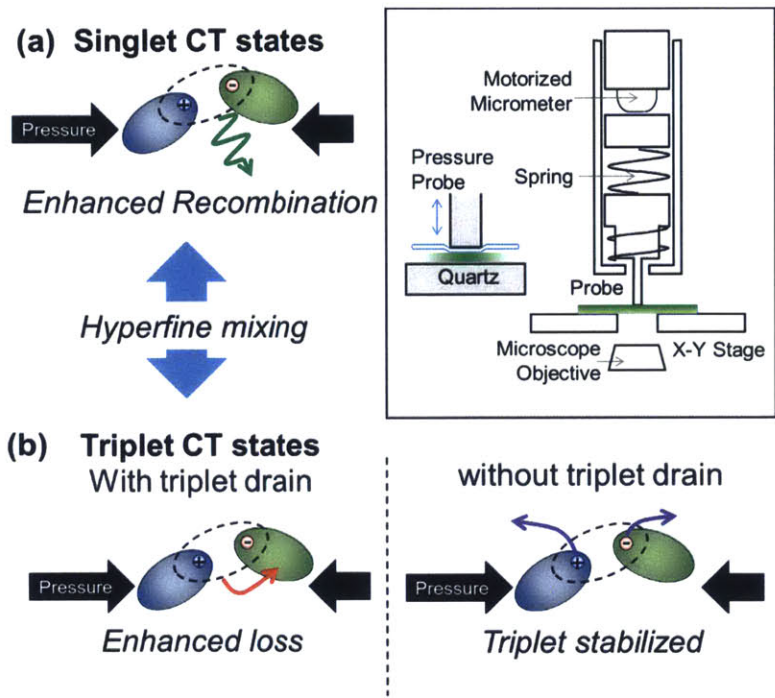
Figure 7-2. Schematic of expected changes in (a) singlet and (b) triplet CT states as a function of their size. The possible triplet dynamics are dependent on the presence of a triplet quenching state or 'drain' on the donor or the acceptor. (inset) The measurement apparatus used to apply pressure to the films.

In the following, we characterize the complex set of tradeoffs for singlet and triplet CT states by applying external pressure to donor-acceptor blends[152,153] and observe its effect on the principal spin-dependent loss pathways (Figure 7-2). Singlet CT states recombine directly to the singlet ground state of the donor and acceptor, and we find that this loss pathway is exacerbated as the CT state is physically constrained. Applied pressure also enhances back transfer from triplet CT states to low-lying triplet exciton drains present on either the donor or acceptor.[145,154] Applying a magnetic field to decrease the conversion of singlet CT states to triplet CT states allows us to identify the spin of the CT states responsible for efficient generation of photocurrent. We find that when a triplet drain is present, singlet CT states are responsible for the efficient generation of photocurrent, but in the absence of a triplet drain, photocurrent is more efficiently generated from

112

the triplet CT states. Consequently, we find that the CT states of *conventional* OPVs should be designed to be as physically large as possible, in order to minimize the back transfer from triplet CT states to triplet excitons, and with minimal sources of spin mixing within the CT manifold, in order to prevent intersystem crossing from the original singlet CT state. In the absence of low-lying triplet excitons, however, we find that triplet CT states are the most efficient source of photocurrent because they are spin-protected against recombination. Devices without triplet drains tolerate compressed CT states, even showing extended CT state lifetimes under applied pressure.

7.4. CT State Dynamics

Singlet and triplet CT states are monitored as a function of size using a set of exciplex emitters originally designed for thermally activated delayed fluorescence (TADF) in organic light-emitting devices (OLEDs). Two specific TADF thin film blends were selected: 4,4',4''-tris[3-methylphenyl(phenyl)amino]triphenylamine (m-MTDATA) as the donor and either tris-[3-(3-pyridyl)mesityl]borane (3TPYMB) or 2-(biphenyl-4-yl)-5-(4-tert-butylphenyl)-1,3,4-oxadiazole (t-Bu-PBD) as the acceptor (Figure 7-3(a)). These materials have been demonstrated to fluoresce from the exciplex CT state with efficiencies of approximately 20%, and they exhibit the bi-exponential transient fluorescence decays and temperature dependence characteristic of single-molecule TADF emitters.[137]
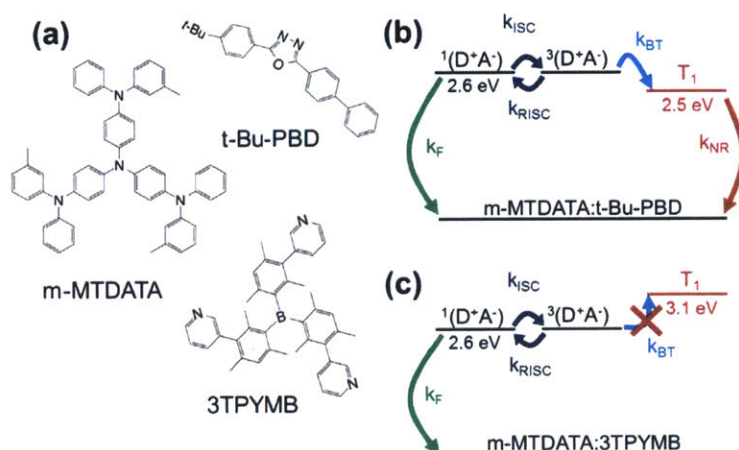
Figure 7-3. (a) Chemical structures of m-MTDATA, t-Bu-PBD, and 3TPYMB. (b) The crucial energy levels and rates for the m-MTDATA:t-Bu-PBD and (c) m-MTDATA:3TPYMB systems. The excitonic triplet state T1 state is for the acceptor; the excitonic triplet of m-MTDATA is approximately 2.7 eV (not shown).

The dynamics of both systems are shown in the rate diagrams of Figure 7-3(b) and (c). Three critical states define the system: singlet CT state $^1(D^+A^-)$, triplet CT state $^3(D^+A^-)$, and excitonic triplet states. In both systems, the singlet CT state lies at approximately 2.6 eV as determined by exciplex CT state fluorescence. The triplet CT state is nearly iso-energetic with the singlet CT state; the triplet CT for the t-Bu-PBD acceptor system is estimated to be between 5 meV and 50 meV lower than that of the singlet CT state.[137,155] Note that the observed CT state emission in these systems is due to the exciplex singlet CT state between nearest neighbor donor-acceptor molecules. Spin-orbit coupling induced intersystem crossing (ISC) and reverse intersystem crossing (RISC) modulates interaction between singlet and triplet exciplex CT states. Additionally, donor/acceptor systems like this may also contain another intersystem crossing mechanism, in which temporary delocalization of a CT state to form a polaron pair (PP) results in degeneracy of the singlet and triplet states, which are then interconverted through hyperfine

114

coupling with the local magnetic nuclei. This mechanism is affected by an external magnetic field, as will be discussed below.[156,157] To eliminate complications from potential interactions with m-MTDATA excimers,[155] we focus on the relative changes incurred when the acceptor changes from 3TPYMB to t-Bu-PBD while maintaining a constant fraction of the m-MTDATA donor molecules.

Of particular importance to these systems are the excitonic triplet energies. The m-MTDATA triplet exciton lies at 2.7 eV,[137] and is therefore uphill from the triplet CT state. The 3TPYMB triplet exciton lies at approximately 3.1 eV and is energetically inaccessible from the triplet CT state, effectively preventing back transfer to a triplet drain on 3TPYMB. In contrast, the t-Bu-PBD triplet exciton lies at 2.6 eV[158] or below (see Section 7.2.4), approximately isoenergetic with the m-MTDATA:t-Bu-PBD CT state. Thus, the triplet back transfer is blocked in the m-MTDATA:3TPYMB system due to the high energies of the triplet excitons, while the m-MTDATA:t-Bu-PBD system has potentially significant triplet back transfer. Since modern OPVs typically possess triplet drains, the t-Bu-PBD system may be a closer analog for conventional high efficiency devices.

7.5. Pressure Measurements

Pressure effect measurements were performed using mechanical setup shown in Figure 7-2. As expected, emission from the exciplex CT state in a blended film quenches both exciton fluorescence and phosphorescence from the donor and acceptor materials.[137] Figure 7-4 demonstrates the effects of pressure on steady-state photoluminescence (PL) of the CT state emission. Increasing external pressure leads to a redshift in emission energy. The redshift is due to both solvation effect from increased molecular density and increased Coulomb interaction

between the donor and acceptor in the compressed geometry.[159,160] A significant increase in fluorescence intensity was also observed. In order to better understand the dynamics of the system, we measured time resolved fluorescence using time-correlated single photon detector. Figure 7-4 illustrates a typical transient PL measurement under no external pressure. It is evident that there are distinct prompt and delayed dynamics in the system. We define the prompt emission to be within the first $0.3 - 0.7$ μs and delayed emission to be between $4 - 9$ μs for m-MTDATA:t-Bu-PBD and $8 - 12$ μs for m-MTDATA:3TPYMB (Figure 7-5). Following Goushi *et al.*[137] we attribute the prompt emission to singlet CT states and the delayed emission to dynamics of triplet CT states. We fit a single exponential to each of these time windows, and compare the pressure dependent transient dynamics of m-MTDATA:t-Bu-PBD and m-MTDATA:3TPYMB. This reveals the effect of the low-lying t-Bu-PBD triplet exciton drain on the dynamics of singlet and triplet CT states.
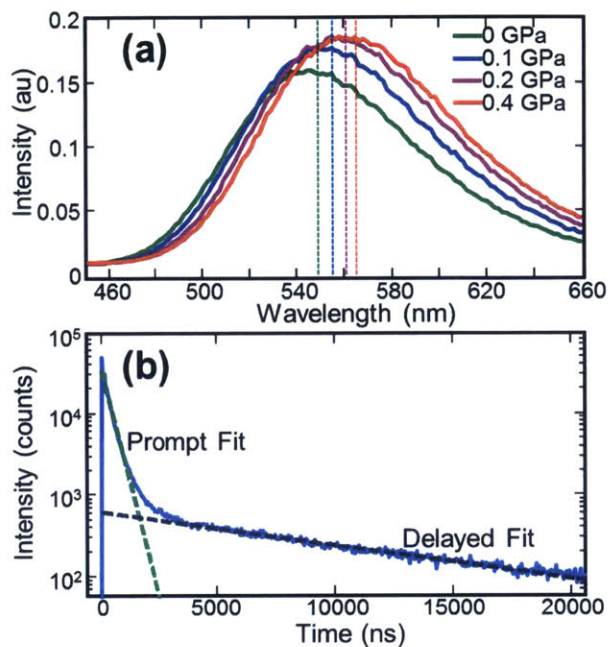
Figure 7-4. (a) Measured m-MTDATA:3TPYMB film PL under pressure. Vertical line indicates the peak wavelength. (b) Transient PL for the m-MTDATA:t-Bu-PBD system. Green and purple dashed lines indicate fitted prompt and delay lifetimes, respectively.

As the molecules are pushed closer together, the red shift in the emission spectrum suggests that overlap between the donor HOMO and acceptor LUMO increases, with significant additional consequences for the photophysics. Recombination processes back to localized states increase – most notably fluorescence from the singlet CT state due to an increase in the transition dipole moment. We also expect both the forward and reverse intersystem crossing rates to slow for CT states localized on neighboring molecules; the exchange splitting is proportional to the overlap of the donor HOMO and the acceptor LUMO and therefore will increase under pressure, and to first order the mixing between triplet and singlet states is inversely proportional to the exchange splitting.
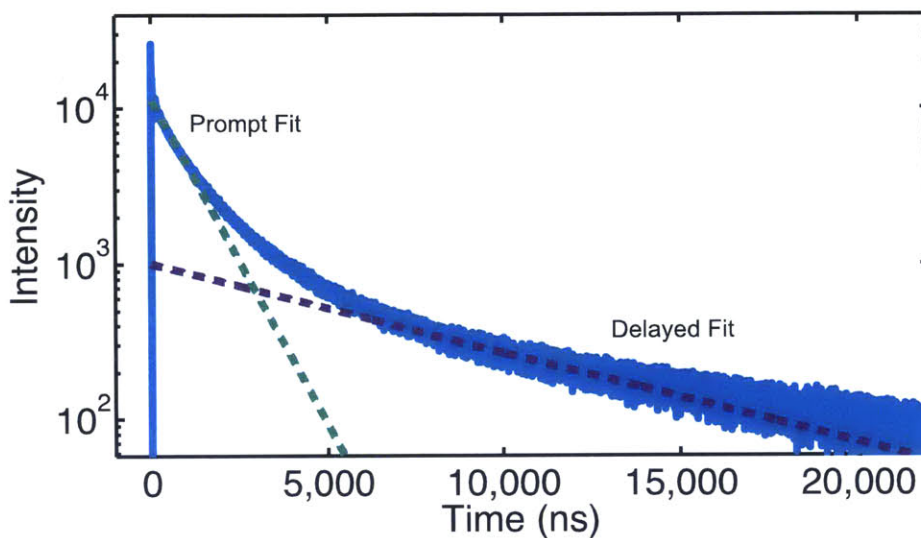
Figure 7-5. Transient PL for the m-MTDATA:3TPYMB system. Green and purple dashed lines indicate fitted prompt and delay lifetimes, respectively.

The trends in prompt dynamics under pressure are shown in Figure 7-6, with the transient lifetime and intensity data plotted in Figure 7-6(a) and (b), respectively. A large increase in prompt intensity is observed in both material systems. The accompanying prompt lifetime change is determined by competition between a decrease in the ISC rate and an increase in fluorescence rate. Indeed, for the m-MTDATA:t-Bu-PBD system, we see little change in the overall lifetime, reflecting that the increase in recombination rate is offset by the decrease in ISC rate. However, a similar prompt lifetime measurement of the m-MTDATA:3TPYMB system shows that the increase in recombination rate dominates the decrease in ISC rate.
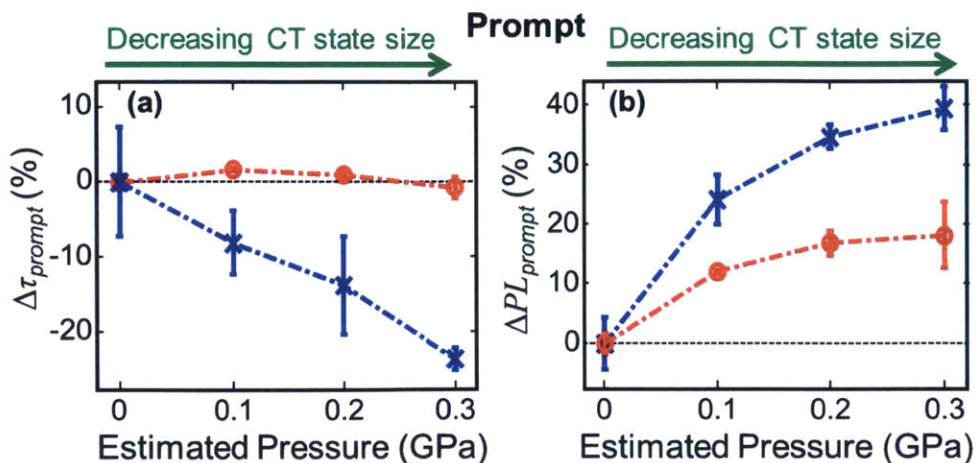
Figure 7-6. (a) Prompt lifetime and (b) integrated prompt intensity changes with applied pressure for the two exciplex systems, where prompt emission is defined as 0.3 μs to 0.7 μs after excitation. Blue data points are from the m-MTDATA:3TPYMB system; red are from m-MTDATA:t-Bu-PBD. Error bars are calculated using standard deviation of 6 independent measurements at each pressure to indicate measurement variations.

The trends in delayed dynamics under pressure are shown in Figure 7-7. The delayed dynamics, which primarily reflect those of triplet CT states, show significant deviation between the two material systems. In the m-MTDATA:3TPYMB system, the probability of back transfer to a molecular triplet exciton is small, thus, an increase in delayed lifetime is observed due to the reduced rate of reverse intersystem crossing. The effect of changes in the exchange splitting is insignificant to the intensity of integrated delayed emission, which still tracks the change in prompt intensity and radiative rate. In the m-MTDATA:t-Bu-PBD system, by contrast, increasing the pressure significantly decreases the delayed lifetime and intensity. We attribute this to an increase in triplet back transfer loss: the exciplexes are drained through this loss channel due to better coupling with the localized t-Bu-PBD triplet (reflected in the decreased lifetime). Thus, triplet back transfer is a significant loss mechanism in the m-MTDATA:t-Bu-PBD system that only worsens as the spacing between electron and hole decreases.
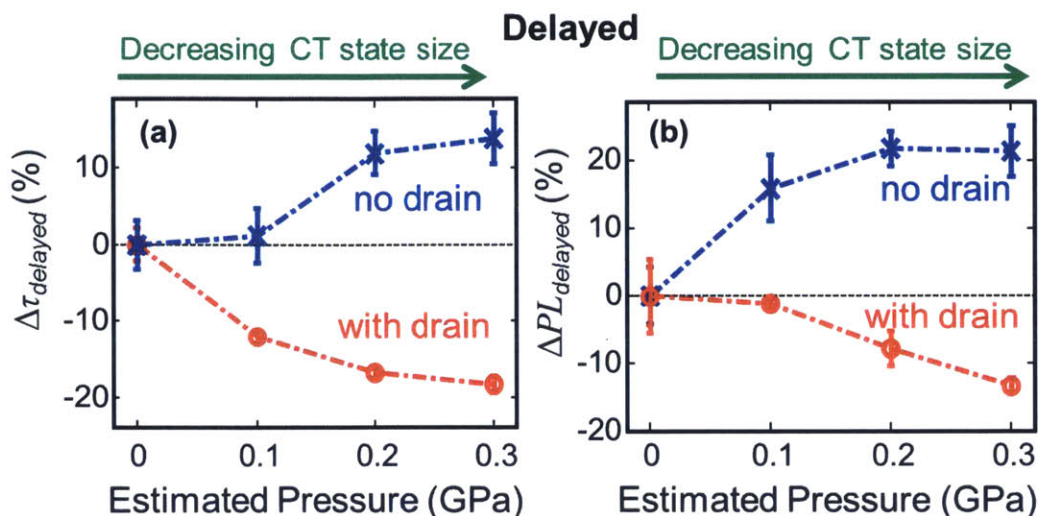
Figure 7-7. (a) Delayed lifetime and (b) integrated delayed intensity changes with applied pressure for the two exciplex systems. Blue data points are from the m-MTDATA:3TPYMB system, where delayed emission is defined to be in the time span of 8 μs to 12 μs after excitation; red data points are from m-MTDATA:t-Bu-PBD, where delayed emission is defined to be in the time span of 4 μs to 9 μs after excitation. The delayed fluorescence quenching with increasing pressure in m-MTDATA:t-Bu-PBD clearly indicates triplet back transfer to a triplet drain. Error bars are calculated using standard deviation of 6 independent measurements at each pressure to indicate measurement variations.

7.6. Magnetic Field Measurements

Next, we probe the CT state populations and resulting changes in photocurrent by applying an external magnetic field to the device and simultaneously monitoring fluorescence and photocurrent.[157] The magnetic fields used in this experiment split two of the three triplet levels by up to ~ 50 μeV. This Zeeman splitting is inconsequential to the intersystem crossing between tightly bound CT states, because the exchange splitting between the singlet and triplet states is much larger than 50 μeV. Instead, the magnetic field only modulates intersystem crossing between singlet and triplet states of larger CT states (PPs) whose exchange splitting is much less than ~ 50 μeV. Indeed, as noted by Frankevich, *et al.*,[157] the magnetic field effect is due to an initial

population of singlet CT states that temporarily *separate* beyond their exchange radius, forming Coulombically-bound polaron pair states with zero effective exchange splitting. Such an extended singlet state may undergo intersystem crossing to a triplet mediated by hyperfine interactions. Otherwise, if the state remains as a singlet, it may collapse back and radiatively recombine within the spin-relaxation time.[156,157] Therefore, we expect the magnetic field-induced increase in the probability of geminately recombining to singlet CT state to lead to an increase in the fluorescence quantum yield. Indeed, an increase in fluorescence under magnetic field was observed in both material systems; see Figure 7-8(a).
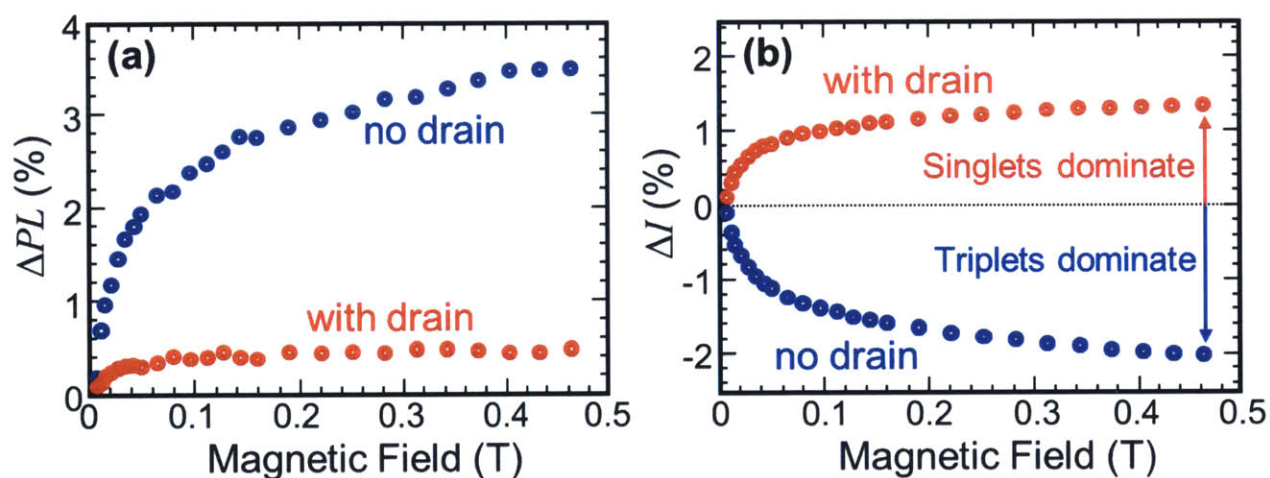
Figure 7-8. (a) Magnetic field effect on fluorescence for the m-MTDATA:t-Bu-PBD (red) and m-MTDATA:3TPYMB (blue) systems. Increases in photoluminescence from both systems demonstrate that the applied magnetic field increases the population of singlet CT states. (b) The magnetic field effect on photocurrent for the m-MTDATA:t-Bu-PBD (red) and m-MTDATA:3TPYMB (blue) systems. The positive magnetic field effect with the t-Bu-PBD acceptor indicates that current is most efficiently collected from the singlet CT state, while the negative magnetic field effect with the 3TPYMB acceptor indicates that current is more efficiently collected from the triplet CT state.

However, there is a striking difference between these material systems when we examine the magnetic field effect on photocurrent measured simultaneously with the fluorescence in Figure 7-8(b). In the m-MTDATA:t-Bu-PBD system, the magnetic field effect on the photocurrent is also positive, *i.e.*, as the singlet CT population increases with applied field, the photocurrent simultaneously increases. This signifies that the photocurrent is more efficiently generated from the singlet CT state, confirming our observation of significant back transfer loss processes quenching the triplet CT states in this material system. Photocurrent from the m-MTDATA:3TPYMB system, however, shows the opposite effect, decreasing with applied magnetic field. As the singlet CT population increases with an applied external magnetic field, the triplet CT population must correspondingly decrease. Because the change in the photocurrent is negative with increasing applied field, we conclude that photocurrent must be more effectively collected through the triplet CT state in the m-MTDATA:3TPYMB system. Indeed, given the dependence of its triplet CT state lifetime on pressure, the magnetic field effect suggests that m-MTDATA:3TPYMB is spin protected in the triplet state. This direct measurement of CT state fluorescence and photocurrent generation under magnetic field indicates that triplet CT is more efficient in photocurrent generation in this system, since recombination to the ground state is spin-forbidden, and recombination to a triplet exciton is energetically unfavorable. These results are reminiscent of recent studies of the P3HT:PCBM OPV system, where alternative methods showed evidence that the spin-protection of triplet CT states can lead to longer lifetimes and greater probability of dissociation to free charges.[156,157] We also note that there was no measurable magnetic field effect on dark conductivity of our devices, indicating the absence of complicating magnetoresistance phenomena.

Finally, we examine the effects on actual device performance in Figure 7-9. Drastic performance reduction due to triplet back transfer is readily apparent in m-MTDATA:t-Bu-PBD. Allowing the triplet CT state to generate photocurrent in the m-MTDATA:3TPYMB system is associated with a factor of four increase in peak external quantum efficiency as compared to the t-Bu-PBD system, unequivocally demonstrating the necessity of minimizing triplet back transfer in future photovoltaic material designs and the potential benefits of spin-protected triplet CT states. In Figure 7-9 we show that open circuit voltage of m-MTDATA:3TPYMB is significantly higher than that of m-MTDATA:t-Bu-PBD, demonstrating that the decrease in recombination losses resulting from spin-protection in the absence of a triplet drain is preserved at weaker internal electric fields.
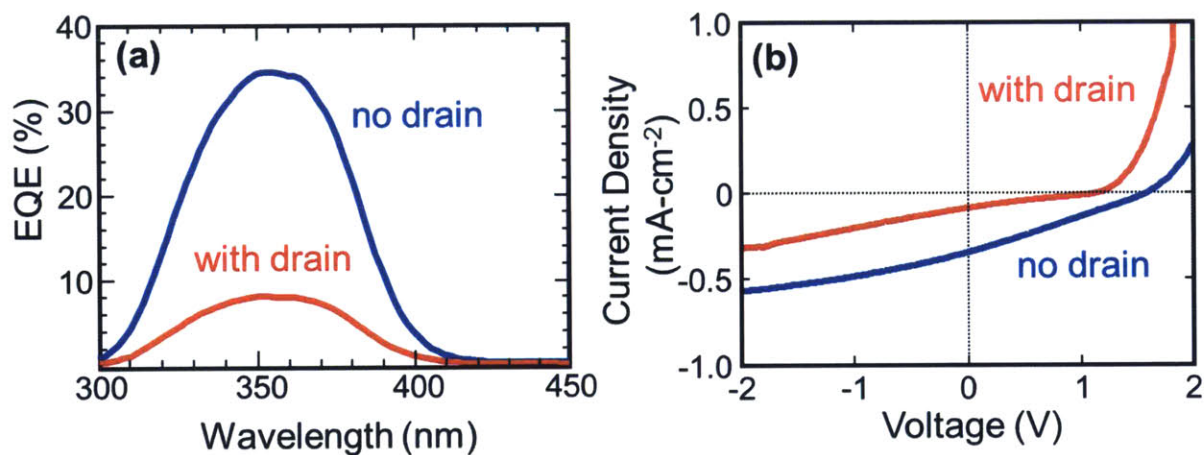
Figure 7-9. (a) External quantum efficiencies of m-MTDATA:3TPYMB (blue) and m-MTDATA:t-Bu-PBD blends (red). Triplet back transfer to the triplet drain on t-Bu-PBD is associated with decreased efficiency relative to the 3TPYMB system. (b) Current-voltage curves for the m-MTDATA:3TPYMB (blue) and m-MTDATA:t-Bu-PBD blends (red). Turning off the triplet drain correlates to a large increase in open circuit voltage.

7.7. CT State Design Rules

Open circuit voltage maximization in OPVs typically requires that CT states be as high in energy as possible - higher, in fact, than the triplet exciton.[150,151] Under this constraint, our work demonstrates the ability to reduce CT state recombination and back transfer losses by maximizing the electron-hole spacing at the interface. The optimum size of the CT state then occurs when the formation rate of the CT state from the molecular exciton is on the order of the excitonic recombination loss rate. Our results also indicate that the current paradigm regarding the necessity of maximal-energy CT states may not be as absolute as it is currently believed to be. Substantial benefits in both EQE and open circuit voltage were shown to result from the spin-protection of triplet CT states when the CT energy is low enough to cutoff back transfer to triplet excitons. Ideal OPV materials, instead, may look more like inorganic quantum dots or OLED TADF materials, with minimal Stokes shift and negligible splitting between singlet and triplet states.[16] The absence of a triplet drain in these systems should allow some CT states to be spin-protected from recombination, a property that may be unique to excitonic solar cell materials.

7.8. CT State Movement

In the previous section, we demonstrated that these CT excitons can relax and intersystem cross. This raised an interstesting question: could these states move as a unit in the blend? To find out, we use an optical microscope with a scanning detector (Figure 7-10) to characterize the physical diffusion of CT states by spatially imaging the transient photoluminescence. By magnifying and reimaging the excitation spot onto a scanning single photon counting avalanche photodetector (APD), we can monitor the spatial broadening associated with exciton diffusion.[97,161] We assume that the PL spatial profile can be modeled by a time-varying Gaussian

function convoluted with the initial exciton distribution. Using Fourier transform analysis, we extract this Gaussian component and compare the standard deviation of each fitted Gaussian function in time to that at $t = 400$ ns after excitation. The initial data is neglected to avoid any anomalies due to statistical errors associated with time correlated single photon counting technique used for lifetime measurements.

The change in standard deviation of the fitted Gaussian broadening component is plotted in Figure 7-10. This direct spatial and temporal visualization of motion reveals that CT states move over 5-10 nm in space. Concurrent with the CT state motion, we observe a red shift in peak emission wavelength over the same time period in spectrally resolved lifetime measurements using a streak camera. The redshift is associated with diffusion to lower energy sites or solvation effect.[16,162] We qualitatively compare the transient dynamics of the red shift to the spatial broadening by overlapping the diffusion data with the evolution of the peak PL wavelength, shown by dotted line in Figure 7-10(c). We observe consistent trends for spectral redshift and the spatial broadening implying the contribution of CT state transport to the spectral shift. The overall spectral shift observed from $t = 0$ to $t = 30$ μs corresponds to a decrease in energy of approximately 60 meV. This is within the order of binding energies expected for tightly bound, geminate excitations.
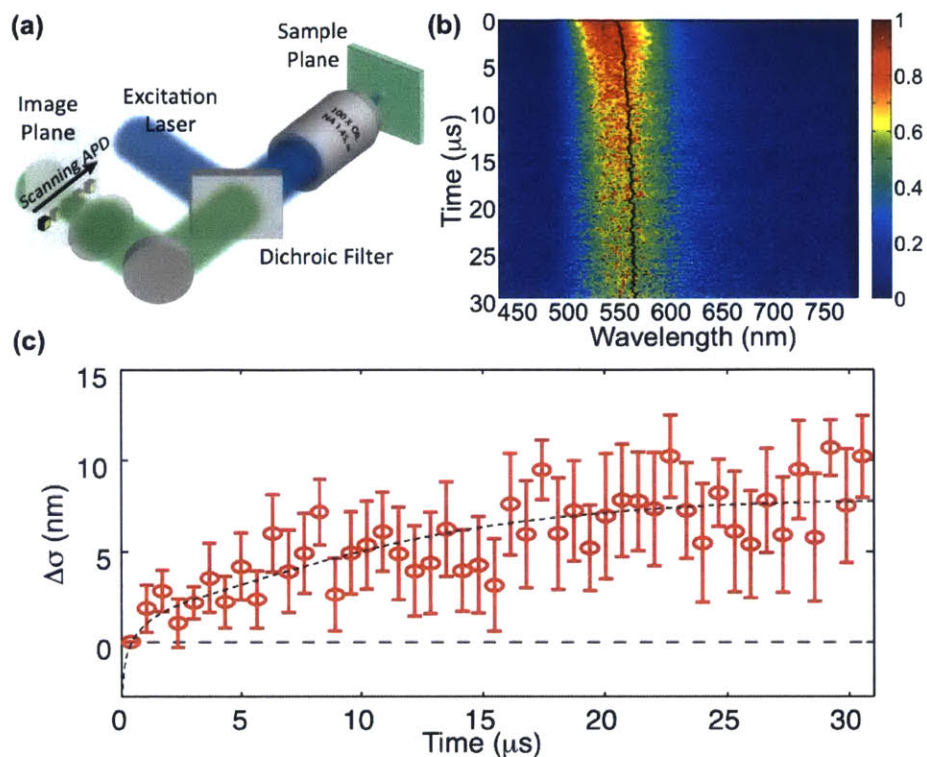
Figure 7-10. (a) Setup schematic of the optical microscope with a scanning detector for diffusion imaging measurements. (b) Spectrally resolved steak camera measurement of charge transfer state emission showing red shift in peak emission wavelength. (c) Change in standard deviation of the spatial broadening Gaussian function extracted from Fourier analysis technique showing CT state diffusion. The overlaid dotted line indicates the trend in the peak PL wavelength obtained from the streak camera measurements in (b) over the same time period.

7.9. CT State Binding Energy

Excitation power and electric field dependent transient PL measurements shown in Figure 7-11 were performed to investigate the contribution of free carrier diffusion towards spatial broadening of luminescence. Figure 7-11(a) shows no notable change in the transient dynamics as a function of optical pump power, which is consistent with luminescence from tightly bound geminate CT exciplex states. Similar to other thermally-activated delayed fluorescent (TADF) materials,[16] the transient characteristic of m-MTDATA:3TPYMB exhibits prompt fluorescence

from the singlet CT states followed by delayed fluorescence as the triplet CT states are thermally-activated back to the fluorescent singlet CT state. Figure 7-11(b) compares the electric-field induced quenching of the prompt and delayed components of the transient allowing us to estimate the exchange splitting between the singlet and triplet CT states. The field-induced quenching follows the Poole-Frenkel theory,[9] as expected for bound states. By analyzing the evolution of the delayed transient with time, we find that the binding energy systematically increases, consistent with the red shift observed in the spectral dynamics. From field-induced quenching measurements, the change in binding energy is estimated to be +12 meV between $t = 1$ µs, and $t = 3$ µs, which is in agreement with the measured redshift during this time period. The estimated exchange splitting obtained from the same technique is 51 meV, consistent with prior reports by Adachi, et al.[137] based on the temperature dependence of the transient.
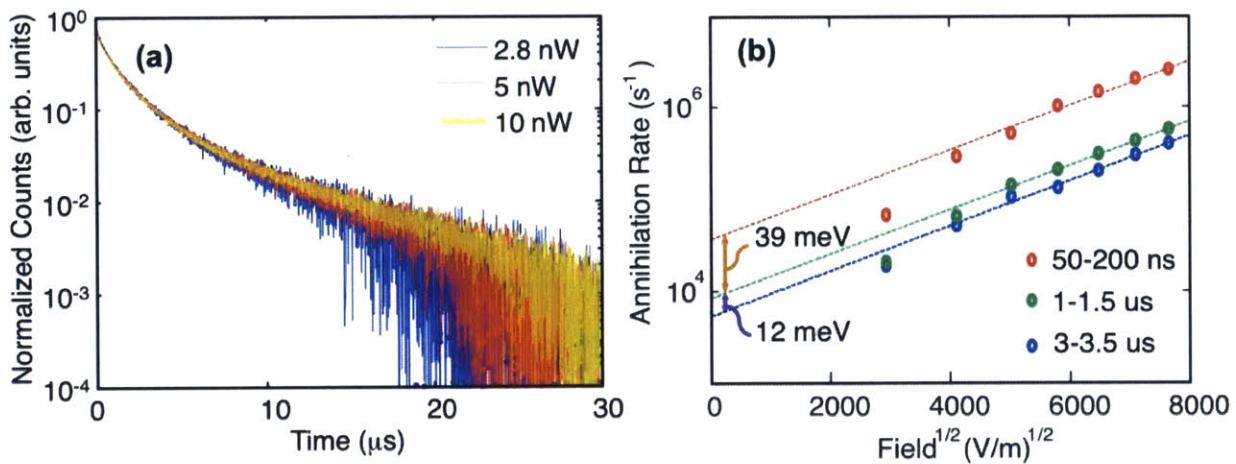
Figure 7-11. (a) Normalized time-resolved CT state PL for select excitation power. The agreement in CT state lifetimes over the measured time interval indicates a geminate emissive CT population, whose dynamics is independent of excitation power. (b) Fluorescence quenching of CT exciplex PL under external electrical field fitted to Poole Frenkel model. The change in energy of 12 meV between 1 µs and 3 µs matches the red shift in PL from streak camera over the same time period.

The excitation power and electric field dependencies confirm that CT states in this system behave as tightly bound particles with geminate characteristics. This geminate nature of CT states in conjunction with the observed spatial broadening indicates that both the photo-generated electron and hole are being displaced. However, the mechanism of CT state transport remains unclear. Direct CT state absorption signal is negligibly low, suggesting that Förster transfer is not likely to be effective. Although Dexter mechanism is feasible, CT states are weakly bound compared to most intra-molecular excitonic states. A more efficient transport is possible, where the CT motion occurs via asynchronous electron and hole motion; the CT state stretches and contracts as it moves through the blend. The latter 'inchworm'-type mechanism is probed by magnetic field studies, which are capable of examining the relative displacement of the electron and the hole. As noted by Frankevich, *et al.*, [163] magnetic field effects in CT states are only observed if the Zeeman splitting induced by the field is comparable to or larger than the exchange splitting. This is not possible given a typical relaxed CT state exchange splitting of 51 meV. The m-MTDATA:3TPYMB system, however, does exhibit magnetic field effects on both PL and photocurrent, suggesting that the CT states can stretch while remaining bound. An expansion of the electron-hole spacing reduces the exchange splitting, rendering the singlet and triplet CT states approximately degenerate. Intersystem crossing can then occur via hyperfine coupling, which is suppressed by Zeeman splitting upon application of an external magnetic field, which decouples two of three triplets.[156,157,163,164] Thus, the magnetic field can act to reduce coupling from singlet to triplet CT states. This preserves the population of the luminescent singlet CT states, increasing the fluorescence, as shown in Figure 7-12.
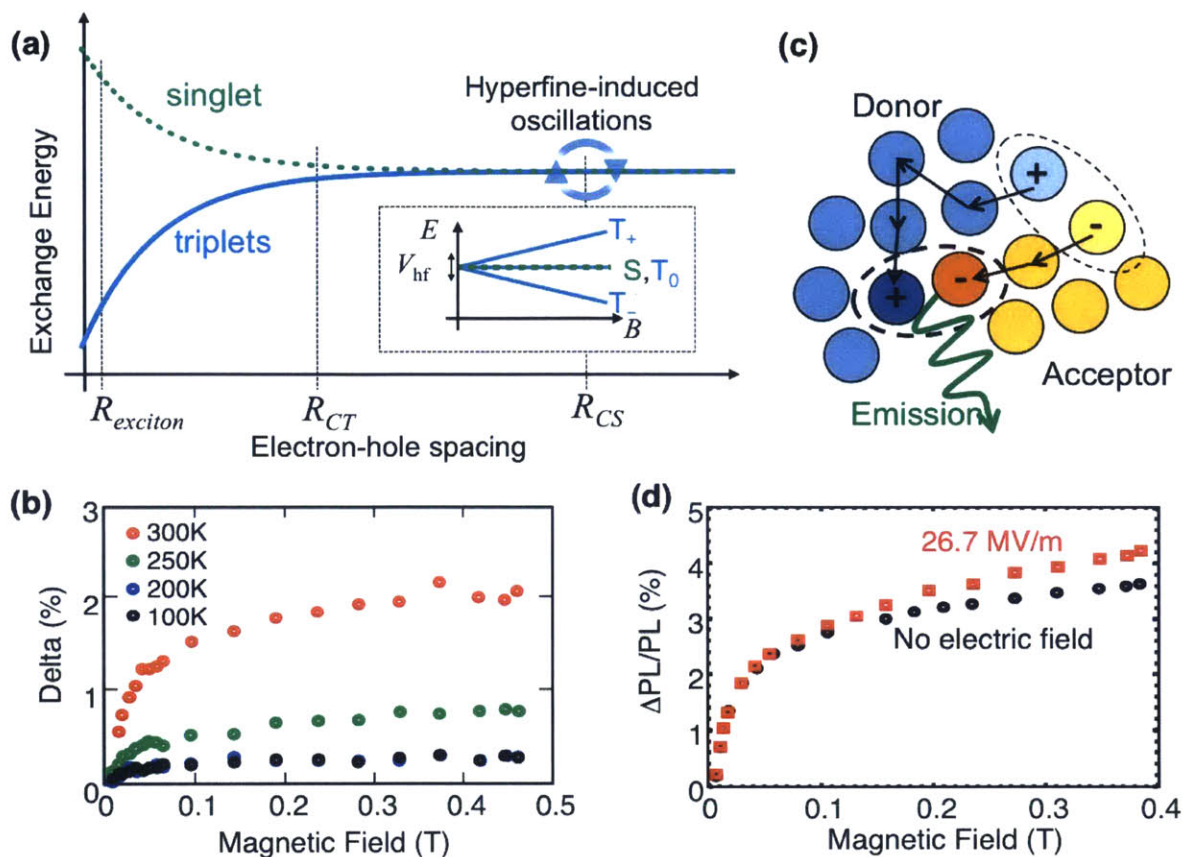
*Figure 7-12. (a) Energy schematic of singlet-triplet energy splitting as a function of electron-hole spacing. **(inset)** Schematic of Zeeman splitting due to external magnetic field in relation to hyperfine coupling V_{hf}. **(b)** The temperature dependence of the magnetic field modulation of CT state PL. The magnitude of the change in PL decreases at lower temperature, indicating magnetic field-dependent hyperfine mediated intersystem crossing decreases with lower thermal energy. However, change in the shape of the magnetic field dependence is not observed over this range of temperatures. (c) Illustration of stretching effect on CT state dynamics and spectral diffusion. (d) Bulk heterojunction device sample under magnetic field at open-circuit and closed-circuit, demonstrating that application of an electric field distorts the size of the CT state.*

7.10. Inchworm Diffusion

The shape of the magnetic field dependence also provides insight into the dynamics of the electron and hole, specifically regarding any spin relaxation effect. According to the model of Schulten and Wolynes, the saturation of the magnetic field effect is determined by the applied magnetic field, the strength of the hyperfine field at each molecule, and the rate at which a charge

hops to neighboring molecules.[165,166] The effective hyperfine field at each molecule is randomly oriented, with a standard deviation of ~1 mT. As a charge hops from molecule to molecule, it experiences a fluctuating local magnetic field, which induces transitions between spin states, leading to spin relaxation of the stretched CT state.[167] Consequently, stronger magnetic fields are required to suppress intersystem crossing when the charges are more mobile and visit more sites. Thus, the saturation of the magnetic field effect serves as a probe of the degree to which these charges travel.

The magnetic field effect can occur only if the CT state can stretch, thus we probe it by examining the temperature dependence of the CT state PL. As shown in Figure 7-12(b), we find the magnitude of the magnetic field effect on PL to be thermally activated, which is consistent with expectations that fewer CT states should stretch at lower temperatures. The shape of the magnetic field dependence as a function of temperature shows no change in saturation behavior above 100 K. Varying spin relaxation effects within the measured range of temperatures yielded no measurable change in the magnetic field effect shape. Instead, the more significant effect of lower temperature is to decrease the number of CT states that stretch beyond the exchange radius, thus decreasing the magnitude of the observed change.

Notable change in spin relaxation is observed, however, under the application of an electric field as shown in Figure 7-12(d). An external field increases the hopping rate of the charges in stretched CT states, increasing the spin relaxation and producing a slower saturation of the magnetic field effect. Overall, the magnetic field studies show that transport via asynchronous electron and hole hopping is plausible; there is fluctuation in the electron-hole spacing during the lifetime of the CT states, but the relative displacement is sufficiently small that the electron-hole pair remain bound.

We conclude by considering the implications of CT transport for organic optoelectronic devices. Arguably, the evidence of CT diffusion to lower energy traps only deepens the mystery concerning the origin of efficient photocurrent generation from tightly bound CT states in organic photovoltaics. Consequently, we offer some insight as to other potential ramifications of the diffusion of CT states. First, it is well known from exciton dissociation models that the probability of charge separation is significantly higher if the CT state is aligned with the electric field.[16,162] The ability of the CT state to move is expected to help reorient the CT states, since the aligned donor-acceptor pairs are lower energy sites. Second, constraining the percolation networks in phase-separated donor-acceptor blends, where CT states can only diffuse along the grain boundaries, would significantly reduce the diffusion distances, while still allowing the states to orient optimally for charge separation. Imaging measurements in different morphologies coupled to simulations should help resolve the mechanism of the transport as well as identify the optimum tradeoff between diffusion and trapping.

Chapter 8: Conclusion

In this document, we have demonstrated the potential of singlet fission, generating an EQE of 126%. We utilized magnetic field effects to quantify the fission yields and understand the inner workings of the solar cell. We demonstrated Dexter transfer to a colloidal nanocrystal, with efficiencies as high as 90% with proper choice of ligand, building an incoherent, low intensity downconverter that could potentially be used for a wide range of solar cells. We further demonstrated the power of utilizing colloidal nanocrystals for upconversion purposes, pushing past 1000 nm into the infrared in a solid state geometry. Finally, we show that triplet CT states may be uniquely advantageous in reducing recombination at an interface.

The demonstration of efficient upconversion and downconversion opens many doors for photovoltaics. In particular, if we can master the junction between the nanocrystals and the silicon, we could place a downconverter layer at the front of the cell, harvesting the high energy light. If we can find an appropriate annihilator, we can utilize PbS nanocrystals out to ~1800 nm to greatly extend the harvestable spectrum of silicon. With future engineering effort, we hope to build a photovoltaic with power efficiency greater than the traditional Shockley-Queisser limit, allowing for cost-effective, renewable, and independent energy for our nation and our world.

Chapter 9: List of Publications

Congreve, D.N.*, Wu, M.*, et al. "Solid-state optical upconversion from near-infrared to visible sensitized by colloidal nanocrystals", *in prep.*

Congreve, D.N.*, Deotare, P.B.*, Chang, W.*, Hontz, E.*, et al. "Nanoscale Transport of Charge Transfer States in Organic Donor-Acceptor Blends", (2015), *submitted*

Wu, T.C, Congreve, D.N., Baldo, M.A. "Solid state photon upconversion utilizing Thermally-Activated-Delayed-Fluorescence Molecules as Triplet Sensitizer", *submitted*

Congreve, D.N.*, Chang, W.*, Hontz, E., et al. "Spin Dependent Charge Transfer State Design Rules in Organic Photovoltaics", (2015) **Nature Communications**, 6 (6415). doi.org/10.1038/ncomms7415

Congreve, D.N.*, Thompson, N.J.*, Wilson, M.W.B.*, et al., "Energy Harvesting of non-emissive triplet excitons in tetracene by emissive PbS nanocrystals", (2014) **Nature Materials** 13, pp. 1039-1043. doi.org/10.1038/nmat4097

Wu, T.C., Thompson, N.J., Congreve, D.N., et al., "Singlet fission efficiency in tetracene-based organic solar cells", (2014) **Applied Physics Letters**, 104 (19). http://dx.doi.org/10.1063/1.4876600

Thompson, N.J., Hontz, E., Congreve, D.N., et al., "Nanostructured singlet fission photovoltaics subject to triplet-charge annihilation", (2014) **Advanced Materials**, 26 (9), pp. 1366-1371. doi.org/10.1002/adma.201304588

Yost, S.R., Lee, J., Wilson, M.W.B., Wu, T., McMahon, D.P., Parkhurst, R.R., Thompson, N.J., Congreve, D.N., et al., "A transferable model for singlet-fission kinetics", (2014) **Nature Chemistry**, 6 (6), pp. 492-497. doi.org/10.1038/nchem.1945

Congreve, D.N.*, Lee, J.*, Thompson, N.J.*, et al., "External quantum efficiency above 100% in a singlet-exciton-fission-based organic photovoltaic cell", (2013) **Science**, 340 (6130), pp. 334-337. doi.org/10.1126/science.1232994

Lee, J., Jadhav, P., Reusswig, P.D., Yost, S.R., Thompson, N.J., Congreve, D.N., et al., "Singlet exciton fission photovoltaics", (2013) **Accounts of Chemical Research**, 46 (6), pp. 1300-1311. doi.org/10.1021/ar300288e

Congreve, D.N.*, Thompson, N.J.*, Goldberg, D., et al., "Slow light enhanced singlet exciton fission solar cells with a 126% yield of electrons per photon", (2013) **Applied Physics Letters**, 103 (26). http://dx.doi.org/10.1063/1.4858176

Reusswig, P.D., Congreve, D.N., Thompson, N.J., Baldo, M.A. "Enhanced external quantum efficiency in an organic photovoltaic cell via singlet fission exciton sensitizer" (2012) **Applied Physics Letters**, 101 (11). http://dx.doi.org/10.1063/1.4752445

Chapter 10: Bibliography

1.   Tsao, J., Lewis, N. & Crabtree, G. Solar FAQs. *US Dep. Energy* 1–24 (2006). at <http://www.sandia.gov/~jytsao/Solar FAQs.pdf>

2.   Jean, J., Brown, P. R., Jaffe, R. L., Buonassisi, T. & Bulovic, V. Pathways for Solar Photovoltaics. *Energy Environ. Sci.* (2015). doi:10.1039/C4EE04073B

3.   Roberts, B. J. Photovoltaic Solar Resource of the United States. (2012). at <http://www.nrel.gov/gis/images/eere_pv/national_photovoltaic_2012-01.jpg>

4.   Sherwood, L. *US Solar Market Trends*. (2014).

5.   Esterly, S., Gelman, R., Buchanan, S., Hicks, A. & Haas, K. *2013 Renewable Energy Data Book*. (2015). at <http://www.nrel.gov/docs/fy15osti/62580.pdf>

6.   Green, M. The path to 25% silicon solar cell efficiency: history of silicon cell evolution. *Prog. Photovoltaics Res.* 183–189 (2009). doi:10.1002/pip

7.   Shockley, W. & Queisser, H. J. Detailed Balance Limit of Efficiency of p-n Junction Solar Cells. *J. Appl. Phys.* **32,** 510 (1961).

8.   Green, M. A., Emery, K., Hishikawa, Y., Warta, W. & Dunlop, E. D. Solar cell efficiency tables (version 44). *Prog. Photovoltaics Res. Appl.* **22,** 701–710 (2014).

9.   Pope, M. & Swenberg, C. E. *Electronic Processes in Organic Crystals and Polymers. Oxford Univ. Press USA 2nd Ed.* (1999). doi:10.1063/1.327880

10.   Scholes, G. D. & Rumbles, G. Excitons in nanoscale systems. *Nat. Mater.* **5,** 683–696 (2006).

11.   Atkins, P. W. & Friedman, R. S. *Molecular quantum mechanics. Book* (1997). doi:10.1002/bio.1290

12.   Griffiths, D. J. *Introduction to Quantum Mechanics. Quantum* **1,** (2005).

13.   Baldo, M. A. *et al.* Highly efficient phosphorescent emission from organic electroluminescent devices. *Nature* **395,** 151–154 (1998).

14.   Baldo, M. A. & Forrest, S. R. Transient analysis of organic electrophosphorescence: I. Transient analysis of triplet energy transfer. *Phys. Rev. B* **62,** 10958–10966 (2000).

15.   Köhler, a. & Beljonne, D. The Singlet-Triplet Exchange Energy in Conjugated Polymers. *Adv. Funct. Mater.* **14,** 11–18 (2004).

16.   Uoyama, H., Goushi, K., Shizu, K., Nomura, H. & Adachi, C. Highly efficient organic light-emitting diodes from delayed fluorescence. *Nature* **492,** 234–238 (2012).

17.   Tang, C. W. Two-layer organic photovoltaic cell. *Appl. Phys. Lett.* **48,** 183–185 (1986).

134

18.   Peumans, P., Uchida, S. & Forrest, S. R. Efficient bulk heterojunction photovoltaic cells using small-molecular-weight organic thin films. *Nature* **425**, 158–62 (2003).

19.   Park, S. H. S. *et al.* Bulk heterojunction solar cells with internal quantum efficiency approaching 100%. *Nat. Photonics* **3**, 297–302 (2009).

20.   Dalal, V. L., Mayer, R., Bhattacharya, J. & Samiee, M. Stability of organic solar cells. *2012 IEEE Int. Reliab. Phys. Symp.* 4A.5.1–4A.5.4 (2012). doi:10.1109/IRPS.2012.6241829

21.   Liu, M., Johnston, M. B. & Snaith, H. J. Efficient planar heterojunction perovskite solar cells by vapour deposition. *Nature* **501**, 395–8 (2013).

22.   Jean, J. *et al.* ZnO nanowire arrays for enhanced photocurrent in PbS quantum dot solar cells. *Adv. Mater.* **25**, 2790–2796 (2013).

23.   Singh, S., Jones, W. J., Siebrand, W., Stoicheff, B. P. & Schneider, W. G. Laser Generation of Excitons and Fluorescence in Anthracene Crystals. *J. Chem. Phys.* **42**, 330 (1965).

24.   Swenberg, C. & Stacy, W. Bimolecular radiationless transitions in crystalline tetracene. *Chem. Phys. Lett.* 327–328 (1968). at <http://www.sciencedirect.com/science/article/pii/0009261468800879>

25.   Merrifield, R. E., Avakian, P., Groff, R. P., Physics, C. & June, L. Fission of Singlet Excitons into Pairs of Triplet Excitons in Tetracene Crystals. **3**, 5–7 (1969).

26.   Johnson, R. & Merrifield, R. Effects of Magnetic Fields on the Mutual Annihilation of Triplet Excitons in Anthracene Crystals. *Phys. Rev. B* **1**, (1970).

27.   Merrifield, R. E. Theory of Magnetic Field Effects on the Mutual Annihilation of Triplet Excitons. *J. Chem. Phys.* **48**, 4318 (1968).

28.   Suna, A. Kinematics of exciton-exciton annihilation in molecular crystals. *Phys. Rev. B* **I**, (1970).

29.   Dexter, D. L. Two ideas on energy transfer phenomena: Ion-pair effects involving the OH stretching mode, and sensitization of photovoltaic cells. *J. Lumin.* **18-19**, 779–784 (1979).

30.   Hanna, M. C. & Nozik, A. J. Solar conversion efficiency of photovoltaic and photoelectrolysis cells with carrier multiplication absorbers. *J. Appl. Phys.* **100**, 074510 (2006).

31.   Smith, M. B. & Michl, J. Singlet fission. *Chem. Rev.* **110**, 6891–936 (2010).

32.   Smith, M. B. & Michl, J. Recent advances in singlet fission. *Annu. Rev. Phys. Chem.* **64**, 361–386 (2013).

33.   Musser, A. J. *et al.* Activated Singlet Exciton Fission in a Semiconducting Polymer. *J. Am. Chem. Soc.* (2013). doi:10.1021/ja405427j

34.   Eaton, S. W. *et al.* Singlet Exciton Fission in Thin Films of t -Butyl-Substituted Terrylenes. *J. Phys. Chem. A* 150409130820008 (2015). doi:10.1021/acs.jpca.5b02719

35. Schrauben, J. N., Ryerson, J., Michl, J. & Johnson, J. C. The Mechanism of Singlet Fission in Thin Films of 1,3-Diphenylisobenzofuran. *J. Am. Chem. Soc.* (2014). doi:10.1021/ja501337b

36. Nichols, V. M. *et al.* Assessing the Potential of Peropyrene as a Singlet Fission Material: Photophysical Properties in Solution and the Solid-State. *J. Phys. Chem. C* 130717190635002 (2013). doi:10.1021/jp4051116

37. Burdett, J. J. & Bardeen, C. J. Quantum beats in crystalline tetracene delayed fluorescence due to triplet pair coherences produced by direct singlet fission. *J. Am. Chem. Soc.* **134,** 8597–607 (2012).

38. Burdett, J. J., Müller, A. M., Gosztola, D. & Bardeen, C. J. Excited state dynamics in solid and monomeric tetracene: The roles of superradiance and exciton fission. *J. Chem. Phys.* **133,** 144506 (2010).

39. Wilson, M. W. B., Rao, A., Ehrler, B. & Friend, R. H. Singlet Exciton Fission in Polycrystalline Pentacene: From Photophysics toward Devices. *Acc. Chem. Res.* **46,** 1330–1338 (2013).

40. Piland, G. B., Burdett, J. J., Kurunthu, D. & Bardeen, C. J. Magnetic Field Effects on Singlet Fission and Fluorescence Decay Dynamics in Amorphous Rubrene. *J. Phys. Chem. C* **117,** 1224–1236 (2013).

41. Chan, W.-L. *et al.* Observing the multiexciton state in singlet fission and ensuing ultrafast multielectron transfer. *Science* **334,** 1541–5 (2011).

42. Tomkiewicz, Y., Groff, R. P. & Avakian, P. Spectroscopic Approach to Energetics of Exciton Fission and Fusion in Tetracene Crystals. *J. Chem. Phys.* **54,** 4504 (1971).

43. Burdett, J. J., Gosztola, D. & Bardeen, C. J. The dependence of singlet exciton relaxation on excitation density and temperature in polycrystalline tetracene thin films: kinetic evidence for a dark intermediate state and implications for singlet fission. *J. Chem. Phys.* **135,** 214508 (2011).

44. Wilson, M. W. B. *et al.* Temperature-independent singlet exciton fission in tetracene. *J. Am. Chem. Soc.* **135,** 16680–16688 (2013).

45. Chan, W., Ligges, M. & Zhu, X. The energy barrier in singlet fission can be overcome through coherent coupling and entropic gain. *Nat. Chem.* 1–6 (2012). doi:10.1038/NCHEM.1436

46. Sebastian, L., Weiser, G. & Bässler, H. Charge transfer transitions in solid tetracene and pentacene studied by electroabsorption. *Chem. Phys.* **61,** 125–135 (1981).

47. Geacintov, N. E., Burgos, J., Pope, M. & Strom, C. Heterofission of pentacene excited singlets in pentacene-doped tetracene crystals. *Chem. Phys. Lett.* **11,** 504–508 (1971).

48. Wilson, M. W. B. *et al.* Ultrafast dynamics of exciton fission in polycrystalline pentacene. *J. Am. Chem. Soc.* **133,** 11830–3 (2011).

49. Jadhav, P. J., Mohanty, A., Sussman, J., Lee, J. & Baldo, M. a. Singlet exciton fission in nanostructured organic solar cells. *Nano Lett.* **11,** 1495–8 (2011).

50.   Ehrler, B., Wilson, M. W. B., Rao, A., Friend, R. H. & Greenham, N. C. Singlet exciton fission-sensitized infrared quantum dot solar cells. *Nano Lett.* **12,** 1053–7 (2012).

51.   Jadhav, P. J. *et al.* Triplet exciton dissociation in singlet exciton fission photovoltaics. *Adv. Mater.* **24,** 6169–74 (2012).

52.   Burdett, J. J., Piland, G. B. & Bardeen, C. J. Magnetic field effects and the role of spin states in singlet fission. *Chem. Phys. Lett.* **585,** 1–10 (2013).

53.   Congreve, D. N. *et al.* External Quantum Efficiency Above 100% in a Singlet-Exciton-Fission-Based Organic Photovoltaic Cell. *Science.* **340,** 334–337 (2013).

54.   Wu, T. C. *et al.* Singlet fission efficiency in tetracene-based organic solar cells. *Appl. Phys. Lett.* **104,** 193901 (2014).

55.   Thompson, N. J., Congreve, D. N., Goldberg, D., Menon, V. M. & Baldo, M. A. Slow light enhanced singlet exciton fission solar cells with a 126% yield of electrons per photon. *Appl. Phys. Lett.* **103,** 263302 (2013).

56.   Reusswig, P. D., Congreve, D. N., Thompson, N. J. & Baldo, M.A. Enhanced external quantum efficiency in an organic photovoltaic cell via singlet fission exciton sensitizer. *Appl. Phys. Lett.* **101,** 113304 (2012).

57.   Thompson, N. J. *et al.* Nanostructured singlet fission photovoltaics subject to triplet-charge annihilation. *Adv. Mater.* **26,** 1366–71 (2014).

58.   Lee, J. *et al.* Singlet Exciton Fission Photovoltaics. *Acc. Chem. Res.* **46,** 1300–1311 (2013).

59.   Yost, S. R. *et al.* A transferable model for singlet-fission kinetics. *Nat. Chem.* **6,** 492–497 (2014).

60.   Semonin, O. E. *et al.* Peak external photocurrent quantum efficiency exceeding 100% via MEG in a quantum dot solar cell. *Science* **334,** 1530–3 (2011).

61.   Nitsche, R. & Fritz, T. Determination of model-free Kramers-Kronig consistent optical constants of thin absorbing films from just one spectral measurement: Application to organic semiconductors. *Phys. Rev. B - Condens. Matter Mater. Phys.* **70,** 1–14 (2004).

62.   Peumans, P., Yakimov, A. & Forrest, S. R. Small molecular weight organic thin-film photodetectors and solar cells. *J. Appl. Phys.* **93,** 3693–3723 (2003).

63.   Yoo, S. *et al.* Analysis of improved photovoltaic properties of pentacene/C60 organic solar cells: Effects of exciton blocking layer thickness and thermal annealing. *Solid. State. Electron.* **51,** 1367–1375 (2007).

64.   Reddy, V. S., Karak, S., Ray, S. K. & Dhar, A. Photovoltaic properties of pentacene/[6,6]-phenyl C61 butyric acid methyl ester based bilayer hetero-junction solar cells. *J. Phys. D. Appl. Phys.* **42,** 145103 (2009).

65. Hwang, J., Sunesh, C. D., Chandran, M., Lee, J. & Choe, Y. Performance characteristics of pentacene-based organic photovoltaic cells. *Org. Electron.* **13**, 1809–1818 (2012).

66. Yoo, S., Domercq, B. & Kippelen, B. Efficient thin-film organic solar cells based on pentacene/C 60 heterojunctions. *Appl. Phys. Lett.* **85**, 5427–5429 (2004).

67. Guan, Z.-L. *et al.* Direct determination of the electronic structure of the poly(3-hexylthiophene):phenyl-[6,6]-C61 butyric acid methyl ester blend. *Org. Electron.* **11**, 1779–1785 (2010).

68. Sato, N., Saito, Y. & Shinohara, H. Threshold ionization energy of C60 in the solid state. *Chem. Phys.* **162**, 433–438 (1992).

69. Kahn, A., Koch, N. & Gao, W. Electronic Structure and Electrical Properties of Interfaces between Metals and -Conjugated Molecular Films. 2529–2548 (2003).

70. Hwang, J., Wan, A. & Kahn, A. Energetics of metal–organic interfaces: New experiments and assessment of the field. *Mater. Sci. Eng. R Reports* **64**, 1–31 (2009).

71. Rim, S.-B., Zhao, S., Scully, S. R., McGehee, M. D. & Peumans, P. An effective light trapping configuration for thin-film solar cells. *Appl. Phys. Lett.* **91**, 243501 (2007).

72. Tvingstedt, K., Andersson, V., Zhang, F. & Inganäs, O. Folded reflective tandem polymer solar cell doubles efficiency. *Appl. Phys. Lett.* **91**, 123514 (2007).

73. Ern, V. & Merrifield, R. Magnetic Field Effect on Triplet Exciton Quenching in Organic Crystals. *Phys. Rev. Lett.* **21**, 609–611 (1968).

74. Lee, J., Jadhav, P. & Baldo, M. A. High efficiency organic multilayer photodetectors based on singlet exciton fission. *Appl. Phys. Lett.* **95**, 033301 (2009).

75. Zilio, S. D., Tvingstedt, K., Inganäs, O. & Tormen, M. Fabrication of a light trapping system for organic solar cells. *Microelectron. Eng.* **86**, 1150–1154 (2009).

76. Cao, W. *et al.* Enhancing light harvesting in organic solar cells with pyramidal rear reflectors. *Appl. Phys. Lett.* **99**, 023306 (2011).

77. Zhang, X.-L., Song, J.-F., Li, X.-B., Feng, J. & Sun, H.-B. Anti-reflection resonance in distributed Bragg reflectors-based ultrathin highly absorbing dielectric and its application in solar cells. *Appl. Phys. Lett.* **102**, 103901 (2013).

78. Heidel, T. D., Mapel, J. K., Singh, M., Celebi, K. & Baldo, M. A. Surface plasmon polariton mediated energy transfer in organic photovoltaic devices. *Appl. Phys. Lett.* **91**, 093506–093506–3 (2007).

79. Burkhard, G. F., Hoke, E. T. & McGehee, M. D. Accounting for interference, scattering, and electrode absorption to make accurate internal quantum efficiency measurements in organic and other thin solar cells. *Adv. Mater.* **22**, 3293–7 (2010).

80. Thompson, N. *et al.* Energy harvesting of non-emissive triplet excitons in tetracene by emissive PbS nanocrystals. *Nat. Mater.* **13,** 1039–1043 (2014).

81. Zhao, N. *et al.* Colloidal PbS quantum dot solar cells with high fill factor. *ACS Nano* **4,** 3743–52 (2010).

82. Zarghami, M. *et al.* p-Type PbSe and PbS quantum dot solids prepared with short-chain acids and diacids. *ACS Nano* **4,** 2475–2485 (2010).

83. Brus, L. Electronic wave functions in semiconductor clusters: experiment and theory. *J. Phys. Chem.* **90,** 2555–2560 (1986).

84. Jasieniak, J., Califano, M. & Watkins, S. E. Size-dependent valence and conduction band-edge energies of semiconductor nanocrystals. *ACS Nano* **5,** 5888–902 (2011).

85. Reineke, S. & Baldo, M. Room temperature triplet state spectroscopy of organic semiconductors. *Sci. Rep.* **4,** (2014).

86. Burdett, J. J. & Bardeen, C. J. The dynamics of singlet fission in crystalline tetracene and covalent analogs. *Acc. Chem. Res.* **46,** 1312–1320 (2013).

87. Tayebjee, M. J. Y., Clady, R. G. C. R. & Schmidt, T. W. The exciton dynamics in tetracene thin films. *Phys. Chem. Chem. Phys.* **15,** 14797–14805 (2013).

88. Ehrler, B. *et al.* In situ measurement of exciton energy in hybrid singlet-fission solar cells. *Nat. Commun.* **3,** 1019 (2012).

89. Graham, K. R. *et al.* Re-evaluating the role of sterics and electronic coupling in determining the open-circuit voltage of organic solar cells. *Adv. Mater.* **25,** 6076–82 (2013).

90. Bardeen, C. J. The Structure and Dynamics of Molecular Excitons. *Annu. Rev. Phys. Chem.* **65,** 127–48 (2014).

91. Köhler, A. & Bässler, H. What controls triplet exciton transfer in organic semiconductors? *J. Mater. Chem.* **21,** 4003 (2011).

92. Dexter, D. L. A Theory of Sensitized Luminescence in Solids. *J. Chem. Phys.* **21,** 836 (1953).

93. Zhu, H., Song, N. & Lian, T. Controlling charge separation and recombination rates in CdSe/ZnS type I core-shell quantum dots by shell thicknesses. *J. Am. Chem. Soc.* **132,** 15038–15045 (2010).

94. Maksym, P. A. & Chakraborty, T. Quantum dots in a magnetic field: Role of electron-electron interactions. *Phys. Rev. Lett.* **65,** 108–111 (1990).

95. Moreels, I. *et al.* Size-dependent optical properties of colloidal PbS quantum dots. *ACS Nano* **3,** 3023–3030 (2009).

96. Nijegorodov, N., Ramachandran, V. & Winkoun, D. P. The dependence of the absorption and fluorescence parameters, the intersystem crossing and internal conversion rate constants on the number of rings in polyacene molecules. *Spectrochim. Acta Part A* **53,** 1813–1824 (1997).

97. Akselrod, G. M. *et al.* Visualization of exciton transport in ordered and disordered molecular solids. *Nat. Commun.* **5,** 3646 (2014).

98. Chatterjee, D. K., Rufaihah, A. J. & Zhang, Y. Upconversion fluorescence imaging of cells and small animals using lanthanide doped nanocrystals. *Biomaterials* **29,** 937–943 (2008).

99. Ang, L. Y., Lim, M. E., Ong, L. C. & Zhang, Y. Applications of upconversion nanoparticles in imaging, detection and therapy. *Nanomedicine* **6,** 1273–1288 (2011).

100. Ho, H. P., Wong, W. W. & Wu, S. Y. Multilayer optical storage disk based on the frequency up-conversion effect from rare-earth ions. *Opt. Eng.* **42,** 2349 (2003).

101. Kim, D. Y., Song, D. W., Chopra, N., De Somer, P. & So, F. Organic infrared upconversion device. *Adv. Mater.* **22,** 2260–2263 (2010).

102. Miteva, T., Yakutkin, V., Nelles, G. & Baluschev, S. Annihilation assisted upconversion: All-organic, flexible and transparent multicolour display. *New J. Phys.* **10,** (2008).

103. Refai, H. H. Static volumetric three-dimensional display. *IEEE/OSA J. Disp. Technol.* **5,** 391–397 (2009).

104. Van Sark, W. G., de Wild, J., Rath, J. K., Meijerink, A. & Schropp, R. E. Upconversion in solar cells. *Nanoscale Res. Lett.* **8,** 81 (2013).

105. Trupke, T., Green, M. a. & Würfel, P. Improving solar cell efficiencies by up-conversion of sub-band-gap light. *J. Appl. Phys.* **92,** 4117 (2002).

106. Franken, P. A., Hill, A. E., Peters, C. W. & Weinreich, G. Generation of optical harmonics. *Phys. Rev. Lett.* **7,** 118–119 (1961).

107. Ou, Z. Y., Pereira, S. F., Polzik, E. S. & Kimble, H. J. 85% efficiency for cw frequency doubling from 1.08 to 0.54 um. *Opt. Lett.* **17,** 640–642 (1992).

108. Strümpel, C. *et al.* Modifying the solar spectrum to enhance silicon solar cell efficiency-An overview of available materials. *Sol. Energy Mater. Sol. Cells* **91,** 238–249 (2007).

109. De Wild, J., Meijerink, A., Rath, J. K., van Sark, W. G. J. H. M. & Schropp, R. E. I. Upconverter solar cells: materials and applications. *Energy Environ. Sci.* **4,** 4835–4848 (2011).

110. Suyver, J. F. *et al.* Upconversion spectroscopy and properties of NaYF4 doped with Er3+, Tm3+ and/or Yb3+. *J. Lumin.* **117,** 1–12 (2006).

111. Singh-Rachford, T. N. & Castellano, F. N. Photon upconversion based on sensitized triplet–triplet annihilation. *Coord. Chem. Rev.* **254,** 2560–2573 (2010).

112. Zhao, J., Ji, S. & Guo, H. Triplet–triplet annihilation based upconversion: from triplet sensitizers and triplet acceptors to upconversion quantum yields. *RSC Adv.* **1,** 937–950 (2011).

113. Gray, V., Dzebo, D., Abrahamsson, M., Albinsson, B. & Moth-Poulsen, K. Triplet-triplet annihilation photon-upconversion: towards solar energy applications. *Phys. Chem. Chem. Phys.* **16,** 10345–52 (2014).

114. Schulze, T. F. & Schmidt, T. W. Photochemical upconversion : Present status and prospects for its application to solar energy conversion. *Energy Environ. Sci.* **8,** 103–125 (2015).

115. Singh-Rachford, T. N. & Castellano, F. N. Photon upconversion based on sensitized triplet-triplet annihilation. *Coord. Chem. Rev.* **254,** 2560–2573 (2010).

116. Monguzzi, A. *et al.* Broadband up-conversion at subsolar irradiance: triplet-triplet annihilation boosted by fluorescent semiconductor nanocrystals. *Nano Lett.* **14,** 6644–6650 (2014).

117. Khnayzer, R. S. *et al.* Upconversion-powered photoelectrochemistry. *Chem. Commun.* **48,** 209–211 (2012).

118. Cao, X., Hu, B. & Zhang, P. High upconversion efficiency from hetero triplet-triplet annihilation in multiacceptor systems. *J. Phys. Chem. Lett.* **4,** 2334–2338 (2013).

119. Yakutkin, V. *et al.* Towards the IR limit of the triplet-triplet annihilation-supported up-conversion: tetraanthraporphyrin. *Chem. – A Eur. J.* **14,** 9846–9850 (2008).

120. Englman, R. & Jortner, J. The energy gap law for radiationless transitions in large molecules. *Mol. Phys.* **18,** 145–164 (1970).

121. Simon, Y. C. & Weder, C. Low-power photon upconversion through triplet–triplet annihilation in polymers. *J. Mater. Chem.* **22,** 20817–20830 (2012).

122. Gywat, O., Krenner, H. J. & Berezovsky, J. *Spins in Optically Active Quantum Dots: Concepts and Methods.* (Wiley-VCH Verlag GmbH & Co. KGaA, 2010).

123. Tabachnyk, M. *et al.* Resonant energy transfer of triplet excitons from pentacene to PbSe nanocrystals. *Nat. Mater.* **13,** (2014).

124. Kondakov, D. Y., Pawlik, T. D., Hatwar, T. K. & Spindler, J. P. Triplet annihilation exceeding spin statistical limit in highly efficient fluorescent organic light-emitting diodes. *J. Appl. Phys.* **106,** (2009).

125. Herkstroeter, W. G. & Merkel, P. B. The triplet state energies of rubrene and diphenylisobenzofuran. *J. Photochem.* **16,** 331–341 (1981).

126. Cheng, Y. Y. *et al.* On the efficiency limit of triplet-triplet annihilation for photochemical upconversion. *Phys. Chem. Chem. Phys.* **12,** 66–71 (2010).

127. Schmidt, T. W. & Castellano, F. N. Photochemical upconversion : The primacy of kinetics. *J. Phys. Chem. Lett.* **5,** 4062–4072 (2014).

141

128. De Mello, J., Wittmann, H. & Friend, R. An improved experimental determination of external photoluminescence quantum efficiency. *Adv. Mater.* **9,** 230–232 (1997).

129. Deng, F., Sun, W. & Castellano, F. N. Texaphyrin sensitized near-IR-to-visible photon upconversion. *Photochem. Photobiol. Sci.* 813–819 (2014). doi:10.1039/c4pp00037d

130. Cui, J., Beyler, A. P., Bischof, T. S., Wilson, M. W. B. & Bawendi, M. G. Deconstructing the photon stream from single nanocrystals: From binning to correlation. *Chem. Soc. Rev.* **43,** 1287–1310 (2013).

131. Whitcomb, K. J., Ryan, D. P., Gelfand, M. P. & Van Orden, A. Blinking statistics of small clusters of semiconductor nanocrystals. *J. Phys. Chem. C* **117,** 25761–25768 (2013).

132. Reineke, S. & Baldo, M. A. Room temperature triplet state spectroscopy of organic semiconductors. *Sci. Rep.* **4,** 3797 (2014).

133. Chang, W. *et al.* Spin-dependent charge transfer state design rules in organic photovoltaics. *Nat. Commun.* **6,** 6415 (2015).

134. Luňák, S., Nepraš, M., Hrdina, R., Kurfürst, A. & Kuthan, J. Photophysics of PBD derivatives. II. The character of the lowest excited triplet state of 2-(biphenyl-4'-yl)-5-phenyl-1,3,4-oxadiazole. *Chem. Phys.* **170,** 77–80 (1993).

135. Holmes, R. J. *et al.* Blue organic electrophosphorescence using exothermic host–guest energy transfer. *Appl. Phys. Lett.* **82,** 2422 (2003).

136. Adamovich, V. I. *et al.* New charge-carrier blocking materials for high efficiency OLEDs. *Org. Electron.* **4,** 77–87 (2003).

137. Goushi, K., Yoshida, K., Sato, K. & Adachi, C. Organic light-emitting diodes employing efficient reverse intersystem crossing for triplet-to-singlet state conversion. *Nat. Photonics* **6,** (2012).

138. Deibel, C., Strobel, T. & Dyakonov, V. Role of the charge transfer state in organic donor-acceptor solar cells. *Adv. Mater.* **22,** 4097–111 (2010).

139. Clarke, T. M. & Durrant, J. R. Charge photogeneration in organic solar cells. *Chem. Rev.* **110,** 6736–6767 (2010).

140. Brédas, J.-L., Norton, J. E., Cornil, J. & Coropceanu, V. Molecular understanding of organic solar cells: the challenges. *Acc. Chem. Res.* **42,** 1691–1699 (2009).

141. Lee, J. *et al.* Charge transfer state versus hot exciton dissociation in polymer-fullerene blended solar cells. *J. Am. Chem. Soc.* **132,** 11878–80 (2010).

142. Vandewal, K. *et al.* Efficient charge generation by relaxed charge-transfer states at organic interfaces. *Nat. Mater.* **13,** 63–8 (2014).

143. Morteani, A. C., Sreearunothai, P., Herz, L. M., Friend, R. H. & Silva, C. Exciton regeneration at polymeric semiconductor heterojunctions. *Phys. Rev. Lett.* **92,** 247402 (2004).

144. Gélinas, S. *et al.* Ultrafast Long-Range Charge Separation in Organic Semiconductor Photovoltaic Diodes. *Sci.* **343**, 512–516 (2014).

145. Chow, P. C. Y., Gélinas, S., Rao, A. & Friend, R. H. Quantitative Bimolecular Recombination in Organic Photovoltaics through Triplet Exciton Formation. *J. Am. Chem. Soc.* **136**, 3424–3429 (2014).

146. Westenhoff, S. *et al.* Charge recombination in organic photovoltaic devices with high open-circuit voltages. *J. Am. Chem. Soc.* **130**, 13653–8 (2008).

147. Bakulin, A. a *et al.* The role of driving energy and delocalized States for charge separation in organic semiconductors. *Science* **335**, 1340–4 (2012).

148. Etzold, F. *et al.* Ultrafast exciton dissociation followed by nongeminate charge recombination in PCDTBT: PCBM photovoltaic blends. *J. Am. Chem. Soc.* **133**, 9469–9479 (2011).

149. Brédas, J.-L., Beljonne, D., Coropceanu, V. & Cornil, J. Charge-transfer and energy-transfer processes in pi-conjugated oligomers and polymers: a molecular picture. *Chem. Rev.* **104**, 4971–5004 (2004).

150. Vandewal, K., Tvingstedt, K., Gadisa, A., Inganas, O. & Manca, J. V. On the origin of the open-circuit voltage of polymer-fullerene solar cells. *Nat Mater* **8**, 904–909 (2009).

151. Veldman, D., Meskers, S. C. J. & Janssen, R. A. J. The Energy of Charge-Transfer States in Electron Donor–Acceptor Blends: Insight into the Energy Losses in Organic Solar Cells. *Adv. Funct. Mater.* **19**, 1939–1948 (2009).

152. Schmidtke, J. P., Kim, J.-S., Gierschner, J., Silva, C. & Friend, R. H. Optical Spectroscopy of a Polyfluorene Copolymer at High Pressure: Intra- and Intermolecular Interactions. *Phys. Rev. Lett.* **99**, 167401 (2007).

153. Albert-Seifried, S. *et al.* Pressure-Induced Delocalization of Photoexcited States in a Semiconducting Polymer. *Phys. Rev. Lett.* **105**, 195501 (2010).

154. Rao, A. *et al.* Kinetic Control of Recombination in Organic Photovoltaics : The Role of Spin. *Nature* **500**, 435–9 (2013).

155. Graves, D., Jankus, V., Dias, F. B. & Monkman, A. Photophysical Investigation of the Thermally Activated Delayed Emission from Films of m-MTDATA:PBD Exciplex. *Adv. Funct. Mater.* **201303389**, n/a–n/a (2013).

156. Steiner, U. E. & Ulrich, T. Magnetic field effects in chemical kinetics and related phenomena. *Chem. Rev.* **89**, 51–147 (1989).

157. Hu, B., Yan, L. & Shao, M. Magnetic Field Effects in Organic Semiconducting Materials and Devices. *Adv. Mater.* 1500–1516 (2009). doi:10.1002/adma.200802386

158. Suzuki, M. *et al.* Highly efficient polymer light-emitting devices using ambipolar phosphorescent polymers. *Appl. Phys. Lett.* **86**, 103507 (2005).

159. Madigan, C. F. & Bulović, V. Solid state solvation in amorphous organic thin films. *Phys. Rev. Lett.* **91,** 247403 (2003).

160. Schmidtke, J., Friend, R. & Silva, C. Tuning Interfacial Charge-Transfer Excitons at Polymer-Polymer Heterojunctions under Hydrostatic Pressure. *Phys. Rev. Lett.* **100,** 157401 (2008).

161. Akselrod, G. M. *et al.* Subdiffusive exciton transport in quantum dot solids. *Nano Lett.* **14,** 3556–3562 (2014).

162. Braun, C. L. Electric field assisted dissociation of charge transfer states as a mechanism of photocarrier production. *J. Chem. Phys.* **80,** 4157–4161 (1984).

163. Frankevich, E. L. *et al.* Polaron-pair generation in poly(phenylene vinylenes). *Phys. Rev. B* **46,** 9320–9324 (1992).

164. Frankevich, E. L., Lymarev, a. a. & Sokolik, I. A. CT-excitons and magnetic field effect in polydiacetylene crystals. *Chem. Phys.* **162,** 1–6 (1992).

165. Knapp, E.-W. & Schulten, K. Magnetic field effect on the hyperfine-induced electron spin motion in radicals undergoing diamagnetic--paramagnetic exchange. *J. Chem. Phys.* **71,** 1878–1883 (1979).

166. Kitahara, K., Osakabe, H., Mori, K. & Titulaer, U. M. The effect of a magnetic field on the recombination of a radical pair. *J. Mol. Liq.* **86,** 53–59 (2000).

167. Shushin, A. I. Magnetic field effects on electron-hole recombination in disordered organic semiconductors. *Phys. Rev. B* **84,** 115212 (2011).